Doctoral thesis

On the Origin of PeV Electrons in the Crab Nebula

かに星雲におけるPeV電子の起源の解明

Masanori Arakawa

Department of Physics, Graduate School of Science,
Rikkyo University

Abstract

We have studied the origin of PeV electrons in the Crab Nebula from observational and theoretical points of view. The Crab Nebula is known as one of the most efficient electron accelerators in the Galaxy. PeV electrons accelerated in the Crab Nebula emit gamma rays via synchrotron emission and inverse Compton scattering. Thus, one can probe the origin of PeV electrons with gamma-ray observations.

Recently, >100 TeV gamma-rays which are the highest energy photons one has ever observed, were detected from the Crab Nebula. We constructed a one-zone model to derive constraints on physical conditions at the acceleration site. The magnetic field is required to be weak, 118 μG, to explain both fluxes measured in MeV and > 100 TeV gamma-ray bands, which implies a weak magnetization of the pulsar wind, $\sigma \simeq 0.01$ in the equatorial plane. Here σ represents a magnetization parameter, which is defined by the ratio of the Poynting flux and the particle energy flux of the pulsar wind. Such a weak magnetic field implies a large gyro radius for ∼1 PeV electrons and it is difficult to confine PeV electrons in a compact region close to the termination shock. This indicates the presence of a second population of electrons that is responsible for the multi MeV radiation. The two considered electron populations could be accelerated in different regions through different acceleration processes. We calculated the non-thermal spectra in the framework of a two-zone model. The first population corresponds to the termination shock accelerated electrons, which is responsible for the bulk of X-ray emission ("wind electrons" component). The second component is an ultrarelativistic Maxwellian distribution. The two-zone modelling provides a good explanation for the X-ray and gamma-ray emission and future MeV and TeV gamma-ray missions might test this hypothesis.

Spaceborne gamma-ray telescopes revealed that 100 MeV gamma-ray radiation from the Crab Nebula shows day- and month-scale variability. The day-scaled variable gamma-ray emission is dubbed as "gamma-ray flares". The flares require a strong magnetic field, ≥ 1 mG, and exhibit a presence of PeV electrons. We have performed a systematic search for gamma-ray flares using 7.4-year data (since 2008 August 8) acquired with *Fermi*-LAT during the off-pulse phases of the Crab pulsar. We found nine small-flux flares ("small flares") which were not reported in literature. The "small flares" originate from the variable synchrotron component of the Crab Nebula, and are characterized by larger fluxes and harder photon indices similarly to the previously reported flares. The "small flares" and the previously reported flares are characterized by "harder when brighter" feature. These flares show day-scale time variability and require a strong magnetic field of $B_{\rm min} \approx 1$ mG at the site of the gamma-ray production. This result seems to be inconsistent with the typical values revealed with modeling of the non-thermal emission from the nebula and the production site of the "small flares" is different from the typical environment in the Crab Nebula.

We have revealed that the Crab Nebula shows the month-scale variability even if all detected flares are excluded while there is no correlation between the gamma-ray flux and X-ray flux observed by *Swift*/BAT (15-50 keV). The month-scale variability indicates that the origin of PeV electrons, which are responsible for the bulk of the synchrotron gamma-ray emission, is different from the "wind electrons." In addition, we have discovered a possible correlation between the gamma-ray flux and the pulsar-knot separation observed by the *Hubble Space Telescope*. Although further observations are required to establish a firm correlation, this is a first signature between the relation of the multi MeV gamma-ray and the emission observed at other wave length.

The works presented in this thesis indicate that the flaring components and the bulk of multi MeV synchrotron emission might originate from the same site which characterized by a strong magnetic field, $\sim$ 1 mG.

Contents

Chapter 1

Introducution

Recent studies have revealed that the formation of non-thermal particle distributions occur in many objects such as supernova remnants, pulsar wind nebulae (PWNe), active galactic nucleus, and cluster of galaxies. This implies that the particle acceleration works at various scales and environments. Cosmic rays (CRs) provide the best example of the non-thermal particles. The energy density of CRs is $\sim$ 1 eV cm^{-3} and this suggests CRs play an important role in the formation of the universe. Therefore, studying the CR acceleration mechanisms, which means the way how energy is transported from thermal to non-thermal form, is essential for understanding of the Universe.

PWNe are known to be efficient CR electron accelerators and the primary galactic gamma-ray sources in the TeV band (H. E. S. S. Collaboration et al., 2018). The energy source of PWNe is a central rotation powered pulsars (RPPs). The pulsar-PWN system is characterized by three regions: (i) pulsar magnetosphere, (ii) relativistic electrons and positrons flow (pulsar wind), (iii) pulsar wind nebula. RPPs induced ultra strong electric field in their vicinity and this field provides electrons and positrons (hereafter electrons) through pair cascades. Eventually the plasma fills a region around the pulsar, which is called the pulsar magnetosphere. The pulsar wind is mainly composed of the electrons originated from the pulsar magnetosphere. PRPs release most of their rotational energy through the pulsar wind. The pulsar wind from the central pulsar encounters the surrounding supernova remnant and then a termination shock is formed. The electrons in the wind are accelerated and randomized at the shock and the PWN are formed. The magnetohydrodynamic (MHD) description provides the most fruitful approach for studying the properties of the PWNe, while the MHD framework requires the particle acceleration as a phenomenological treatment. In spite of many systematic studies, one does not understand why PWNe are such efficient particle accelerators.

In this regard, the Crab Nebula provides a unique opportunity to test the particle acceleration mechanism. The central pulsar, known as Crab pulsar, has a rotation period of 33 millisecond and a large spindown luminosity, $L_{\rm SD} \simeq 5 \times 10^{38}$ erg s^{-1} (Hester, 2008). The spindown luminosity of the Crab pulsar is the second highest power among all known pulsars. The observed synchrotron luminosity of the nebula is $\sim 1.3 \times 10^{38}$ erg s^{-1} and it corresponds to about 26% of the spindown luminosity. The

large spindown luminosity allows detailed observational and theoretical studies and the Crab Nebula is one of the most studied objects in astrophysics at the present. Thanks to its brightness, the non-thermal radiation from the Crab Nebula is observed from radio to TeV gamma-ray band, extending over 20 decades of frequency. The Crab Nebula is treated as the "standard candle" in the X-ray and TeV gamma-ray astronomy because of its bright and persistent radiation. The broadband spectrum can be well explained based on MHD model via synchrotron and inverse Compton (IC) scattering radiation (e.g. Kennel and Coroniti, 1984a; Atoyan and Aharonian, 1996). The synchrotron spectrum extended up to 100 MeV indicates an presence of PeV electrons and the Crab Nebula is known to the only leptonic PeV accelerator. In addition, the brightest TeV gamma-ray radiation allows one to detect >100 TeV gamma-ray photons (Abeysekara et al., 2019; Amenomori et al., 2019), which is the dawn of the multi hundred gamma-ray astronomy.

The recent spaceborne gamma-ray telescopes (*Fermi* and *AGILE*) detected the rapid gamma-ray enhancements, called flares, so the Crab Nebula can not be treated as the "standard candle" at least at 100 MeV. The peak synchrotron energy during flares exceeds the theoretical limit under the ideal MHD configuration and the short time variability imposes a stronger magnetic field $\sim$ 1 mG than the averaged magnetic field in the Crab Nebula revealed with modeling of the non-thermal emission from the nebula (e.g. Atoyan and Aharonian, 1996; Meyer et al., 2010). These indicate that flares originate from non-ordinary environment in the nebula where electrons are accelerated up to PeV. The flares are likely associated with the acceleration via the magnetic reconnection in a highly magnetized region (e.g Lyutikov et al., 2018a). According to 3D MHD simulations, such region seems to be realized at the base of the jet (Porth et al., 2014).

The important issue is how and where the electrons are accelerated up to PeV energies in the Crab Nebula. The canonical explanation is that particles are accelerated at the termination shock via the shock acceleration. This scenario seems to be confirmed in the multi-TeV band by measurements of the extension of the Crab Nebula in UV, X-ray and TeV bands (H. E. S. S. Collaboration et al., 2019a). However, there is still no supports for this description for multi hundred TeV electrons. In addition, the electron acceleration up to PeV energies require an efficiency close to the maximum rate under the ideal MHD configuration (Aharonian et al., 2002). In this regard, the >100 TeV gamma-ray photons which are smoothly connected with previous TeV gamma-ray fluxes provide new insight about the acceleration at the termination shock. In this energy range, the dominant target for the IC is Cosmic Microwave Background Radiation, therefore one can extract information about the parent electrons and the strength of the magnetic field at the acceleration site without any MHD model. In this thesis, we derive a constraint on the strength of the magnetic field in the acceleration site based on the one-zone modeling and discuss a possibility of the multi-component composition of the electron distribution.

On the other hand, additional spectral component emerges during flares (e.g Buehler et al., 2012), which indicates an existence of another electron population. The flare is treated as rare events, about

once a year, therefore the flare component is not strongly related to persistent synchrotron emission. However, the 100 MeV gamma-ray emission from the Crab Nebula shows variability at various time-scales (Buehler et al., 2012), which indicates low-intensity flares might be hidden. If such flares exist, the contribution of the flaring component may be not small for the 100 MeV gamma-ray emission. In addition, flares characterized not only by the day-scale variability but also the month scale variability was observed in the Crab Nebula (Abdo et al., 2011), while the origin of this variability is still missing. A potentially effective approach is to link gamma-ray emission to some other wavelength, where spatially resolved observations are possible. Such correlated studies may elevate limitations of gamma-ray instruments that cannot resolve the gamma-ray production sites. The monthly gamma-ray variability also helps to understand the origin of the multi MeV synchrotron emission and particle acceleration sites. In this thesis, a systematic survey of the weak-intensity flares ("small flares"), which has not been reported in literature and the month-scale gamma-ray analysis is performed based on 7.4 years *Fermi*-LAT data. We discuss flare statistics because the increased number of flares enable us to discuss a flare property from the statistical point of view and then we characterize the environment at the production site for each "small flare". In order to study its origin of the month-scale variability, the possible correlation with the hard X-ray band and the pulsar-knot separation observed by the *Hubble Space Telescope* are investigated. Finally, we propose a scenario that the origin of the multi MeV synchrotron emission is the base of the jet featured by the strong magnetic field $\sim$ 1 mG.

This thesis is organized as follows. In Chapter 2, we review the Crab Nebula focusing on the MHD-flow model and gamma-ray emission including flares. Chapter 3 presents the physical implications of $>$ 100 TeV gamma rays observed in the Crab Nebula. Chapter 4 provides a brief description of the *Fermi*-LAT and the analysis method. The results of the *Fermi*-LAT of the Crab Nebula are shown in this chapter. We discuss the interpretations of the variability of the Crab Nebula and the origin of the multi MeV synchrotron emission in Chapter 5. Chapter 6 presents a summary of this thesis.

Chapter 2

Review: Crab Nebula

In this chapter, we summarized the magnetohydrodynamics model and radiation mechanism in the Crab Nebula. In addition, we give explantations of the gamma-ray observation results and the current understanding of gamma-ray flares observed in the Crab Nebula.

2.1 The MHD Model of the Crab Nebula

The Crab Nebula has been observed by many instruments and such observations allow one to understand the pulsar wind nebula (PWN) system. Left panel of Figure 2.1 represents a composite image of the Crab Nebula: X-ray image (*Chandra*) is shown in blue, optical continuum image (*Hubble Space Telescope*) is shown in green, and red shows a radio image (Very Large Array). The X-ray image is shown in Figure 2.1 right panel. We can see the differences in spatial extension of the Crab Nebula: the lower photon energy image is the larger is the emission extension. In addition, the X-ray morphology deviates from a spherical symmetry and contains the fine structures: jet, torus, and inner ring (see Figure 2.1 right panel). For description of such PWN systems, magnetohydrodynamics (MHD) treatment is widely accepted (e.g. Olmi et al., 2016; Porth et al., 2017). Seminal works were done by the Rees and Gunn (1974) and Kennel and Coroniti (1984b) where one introduced the MHD approach. Since the pulsar is produced after the supernova, one expects the central pulsar is enclosed by the supernova remnant (SNR). Rees and Gunn (1974) pointed out that the termination shock is formed at the equilibrium between the ram pressure of pulsar wind and the pressure in the nebula which allows one to determine the radius of the termination shock:

$$R_{\rm TS} = \sqrt{\frac{L_{\rm SD}}{4\pi c p_{\rm PWN}}}, \tag{2.1}$$

where $R_{\rm TS}$, $L_{\rm SD}$ and $p_{\rm PWN}$ are the distance of the termination shock form the central pulsar, the spin down luminosity and the pressure of the nebula, respectively. Rees and Gunn (1974) estimated $R_{\rm TS} = 0.1$ pc and this is good agreement with the location of the “inner ring" observed by *Chandra* (Weisskopf et al., 2000) (see Figure 2.1 right). Therefore the “inner ring" is considered to be the termination shock

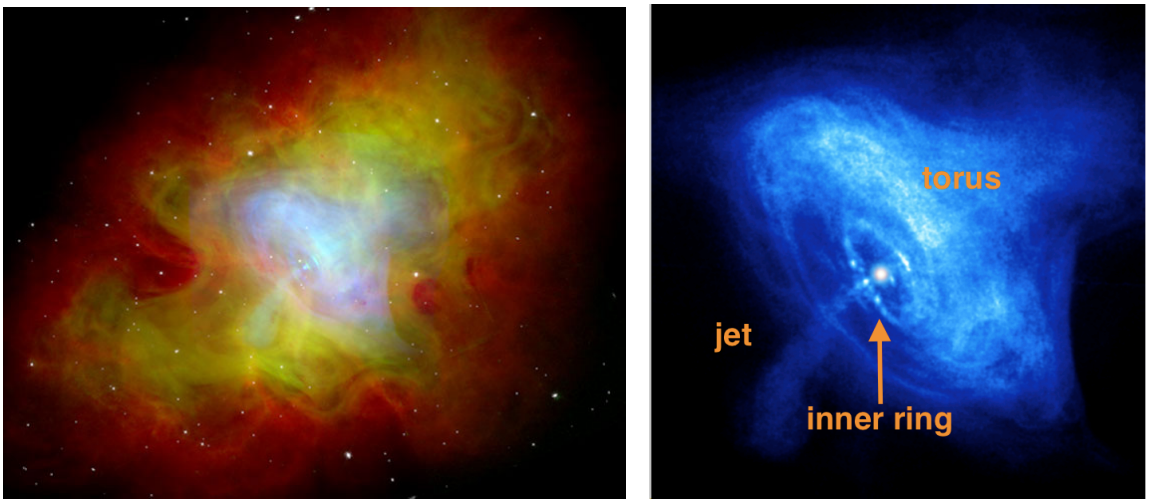

Figure 2.1 left: Composite image of the Crab Nebula. Blue indicates X-rays (from *Chandra*), green is optical (from the *Hubble Space Telescope*), and red is radio (from the Very Large Array). right: The X-ray image of the Crab Nebula. The left figure is taken from https://apod.nasa.gov/apod/ap020920.html (Credit: J. Hester (ASU), CXC, HST, NRAO, NSF, NASA) and the right one is from http://chandra.harvard.edu/photo/1999/0052/ (Credit: NASA/CXC/SAO) with the modifications by the author.

of the relativistic pulsar wind. The particle acceleration is assumed to occur at the termination shock. The accelerated electrons can radiate in the downstream and we can observe their emission as a nebula.

Kennel and Coroniti (1984b) described the bulk motion of the electrons between the PWN and the contact discontinuity (the boundary between the PWN and the SNR) based on a stationary and spherical symmetric MHD description (hereafter KC model). The schematic image of the Crab Nebula and the SNR is shown in Figure 2.2. The KC model provides the transport and radiative cooling of electrons with the analytical MHD-flow solution (Kennel and Coroniti, 1984a). This allows computing the volume emissivity of the synchrotron radiation. Their model was extended by including the IC radiation in order to explain the TeV gamma ray emission (Atoyan and Aharonian, 1996). The predicted spectrum agreed with the observed non-thermal spectrum. This supports the scenario that particles are accelerated at the termination shock and transported with the MHD flow. Here, we provide a detailed description of the MHD flow and the transport of the non-thermal particles based on the KC model.

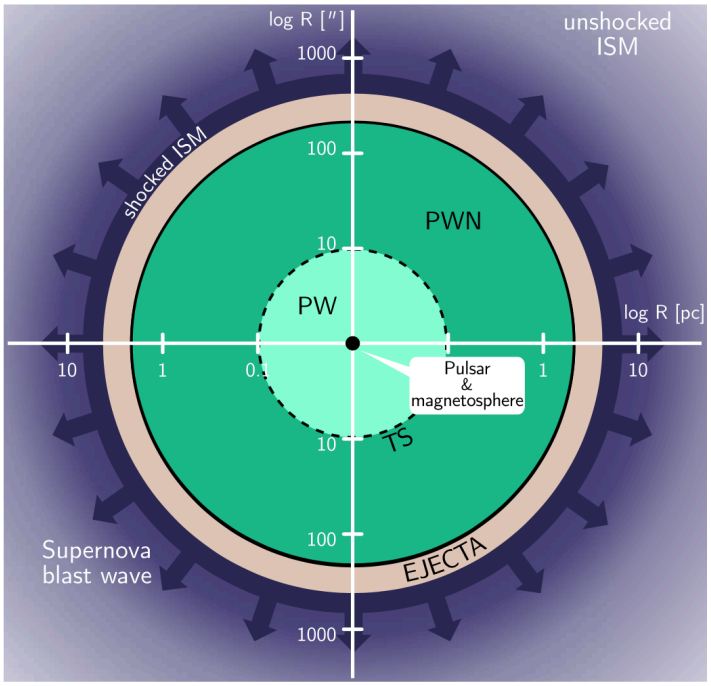

Figure 2.2 The schematic image of the Crab Nebula and surrounding the supernova remnant based on the Kennel and Coroniti (1984b). The spacial scale is represented in logarithmic scale and x-axis and y-axis show in unit of parsec and arcsecond, respectively. The pulsar wind (light green region) composed of the ultrarelativistic electrons is dissipated at the termination shock which is located at ~ 0.1 pc (black dashed line) from the central pulsar. The dissipated electrons are randomized and forms pulsar wind nebula (dark green region). The boundary between the pulsar wind nebula and the supernova remnant, which is called by the contact discontinuity, is located at ~ 2 pc (black thick line). The figure is taken from Del Zanna and Olmi (2017).

MHD model

The 1D MHD flow is determined by the three parameters: the wind magnetization, the location of the termination shock and the upstream Lorentz factor. The most important parameter is the wind magnetization, σ. The wind magnetization parameter represents which fraction of the spin-down luminosity, $L_{\rm SD}$, is carried by the Poynting flux:

$$L_{\rm SD} = n_1 \gamma_1 u_1 R_{\rm TS}^2 m_e c^3 (1+\sigma)\,, \tag{2.2}$$

and the wind magnetization parameter is defined as

$$\sigma \equiv \frac{B_1^2}{4\pi n_1 u_1 \gamma_1 m_e c^2}\,, \tag{2.3}$$

where m_e and c represent the electron rest mass and the speed of the light, respectively. The subscription 1 shows the parameters at the upstream of the termination shock: n_1, B_1 γ_1, and $u_1 \left(= \sqrt{\gamma_1^2 - 1}\right)$

are the electron density, the strength of the magnetic field, the bulk Lorentz factor and the radial four velocity of the wind. Under the approximation of the stationary and spherical symmetry flow with a toroidal magnetic field, the basic equations of the MHD flow are written by:

$$\frac{\mathrm{d}}{\mathrm{d}r}(cnur^2) = 0\,, \tag{2.4}$$

$$\frac{\mathrm{d}}{\mathrm{d}r}\left(\frac{ruB}{\gamma}\right) = 0\,, \tag{2.5}$$

$$\frac{\mathrm{d}}{\mathrm{d}r}(nur^2\epsilon) + P\frac{\mathrm{d}}{\mathrm{d}r}\left(r^2u\right) = 0\,, \tag{2.6}$$

$$\frac{\mathrm{d}}{\mathrm{d}r}\left[nur^2\left(\gamma\mu + \frac{B^2}{4\pi n\gamma}\right)\right] = 0\,. \tag{2.7}$$

These equations represent the conservation of number flux, the conservation of magnetic flux, the propagation of internal energy, and the conservation of total energy. Here ϵ, μ are the relativistic internal energy per particle and the specific enthalpy ($\mu = \epsilon + p$), respectively. P and p represent the gas pressure and specific pressure. As shown by Kennel and Coroniti (1984b), the basic equations (Eq. (2.4) – Eq. (2.7)) are governed by the following equation:

$$(1 + u_2^2 v^2)^{1/2}\left[\delta + \Delta(vz^2)^{-1/3} + \frac{1}{v}\right] = \gamma_2(1 + \delta + \Delta)\,, \tag{2.8}$$

which describes the downstream four velocity, $v(z) = \frac{u}{u_2}$ in unit of the post shock velocity as a function of the dimensionless distance, $z = \frac{r}{R_{\rm TS}}$. Here subscription 2 means the parameters at the downstream of the termination shock. The dimensionless parameters δ and Δ in Eq. (2.8) are defined by

$$\delta = \frac{4\pi n_2\gamma_2^2 mc^2}{B_2^2} \simeq \frac{u_2}{u_1\sigma} \simeq 0\,, \tag{2.9}$$

$$\Delta = \frac{16\pi P_2\gamma_2^2}{B_2^2} = \left(\frac{1+\sigma}{\sigma}\right)\frac{u_2}{\gamma_2} - 1\,. \tag{2.10}$$

δ becomes small in the strong shock limit ($\frac{u_2}{u_1} \ll 1$) and could be neglected. According to the Rankine-Hugoniot relation which determines the jump condition between the downstream and upstream, the four velocity and the bulk Lorentz factor at the immediately downstream, u_2 and γ_2, depend on only the wind magnetization parameter σ (Kennel and Coroniti, 1984b). Therefore, the flow four velocity is determined by the σ and $R_{\rm TS}$.

The asymptotic flow velocity at far from the termination shock, V_∞, can be obtained from by Eq. (2.8) as follows:

$$V_\infty = \frac{u_\infty}{\gamma_\infty} = \frac{\sigma}{1+\sigma}c\,, \tag{2.11}$$

where u_∞ and γ_∞ represent the radial four velocity and the bulk Lorentz factor at far from the termination shock. This means a large sigma flow (i.e. Poynting flux dominant) in the downstream becomes a constant asymptotic velocity. Therefore, in order to decrease the flow speed down to the expansion velocity of the SNR, ~ 2000 km s^{-1}, a weak magnetization $\sigma < 0.01$ is required.

In the case of the $\sigma < 1$, the downstream flow becomes nonrelativistic ($\gamma_2 \simeq 1$), so the radial profile of the magnetic field can be written as follows:

$$B(z) = B_2 \frac{u_2}{u(z)z} \,. \tag{2.12}$$

The strength of the magnetic filed at the downstream, B_2, is determined by the Rankine-Hugoniot relation (Kennel and Coroniti, 1984b):

$$B_2 = 3B_1(1 - 4\sigma) \,. \tag{2.13}$$

Eqs. (2.2) and (2.3) describe the strength of the magnetic field at the pulsar wind termination shock:

$$B_1 = \sqrt{\frac{L_{\rm SD}}{cR_{\rm TS}} \frac{\sigma}{1+\sigma}} \,. \tag{2.14}$$

Therefore, the downstream magnetic field is also determined by the σ and $R_{\rm TS}$. Figure 2.3 represents the spatial distribution of the magnetic fields at the different magnetization parameters, σ = 0.1, 0.01 and 0.001 (Kennel and Coroniti, 1984b). In this calculation, we assumed $L_{\rm SD} = 5 \times 10^{38}$ erg s^{-1}, $R_{\rm TS} = 0.1$ pc. The strength of the magnetic field increases with the deceleration of the plasma and after the equipartition between the plasma pressure and the magnetic field pressure, the magnetic field gradually decreases with the distance z.

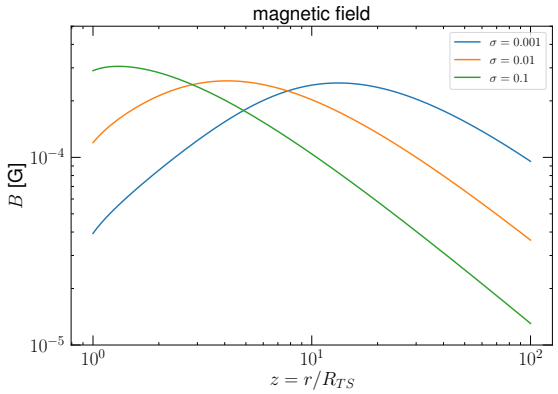

Figure 2.3 The radial distribution of the magnetic field for the various magnetization parameter σ =0.1 (green line), 0.01 (orange line) and 0.001 (blue line) based on the 1D MHD model (Kennel and Coroniti, 1984b). We assumed the spindown luminosity $L_{\rm SD} = 5 \times 10^{38}$ erg s^{-1} and the location of the termination shock $R_{\rm TS} = 0.1$ pc.

Non-thermal particles

Kennel and Coroniti (1984a) first calculated the transport of the non-thermal particles with synchrotron cooling and adiabatic losses. Their model is able to reproduce the emission detected from the Crab Nebula in the optical band and higher frequencies at the synchrotron emission of electrons accelerated at the termination shock. Atoyan and Aharonian (1996) added the IC component to explain $\gtrsim 1$ GeV emission. In order to explain the broadband spectrum in the Crab Nebula, Atoyan and Aharonian (1996) argued that at least two distinct population of electrons is required. One is called "radio electrons", which are responsible for the radio synchrotron emission. The "radio electrons" are assumed to be almost uniformly distributed in the nebula while the origin has not been established. The other is "wind electrons", which is composed of multi TeV electrons. The "wind electrons" is considered to be freshly injected at the termination shock and advected with the MHD flow.

According to Atoyan and Aharonian (1996), the spectrum of the "radio electrons" is described by

$$n_{\rm re} = A_{\rm re} E^{-1.52} \exp\left(-\frac{E}{E_*}\right) \tag{2.15}$$

where E represents the electron energy. $A_{\rm re}$ is the normalization constant, which is determined by the synchrotron radio flux. $E_* = 150$ GeV shows the transition between the "radio electrons" and "wind electrons" (Atoyan and Aharonian, 1996). The "wind electrons" suffer the synchrotron cooling and adiabatic loss after the injection. Atoyan and Aharonian (1996) derived the evolution of the energy distribution, $n_{\rm w}$, of the "wind electrons" in the nebula as

$$n_{\rm w}(r, E) = \frac{1}{(vz^2)^{4/3}} \left(\frac{E'}{E}\right)^2 n_{\rm s}(E') \,. \tag{2.16}$$

where $n_{\rm s}$ is the energy spectrum injected at the termination shock. $E' = E'(E, r)$ represents the initial electron energy at the termination shock. The electron energy at distance z is written as follows:

$$E(z) = \frac{E'}{(vz^2)^{1/3} + \frac{E'}{E_{\rm max}}} \,. \tag{2.17}$$

$E_{\rm max}$ shows the maximum electron energy that is attainable at a distance z with the synchrotron loss and the adiabatic loss:

$$E_{\rm max} = m_e c^2 \left(\frac{9 m_e^3 c^6 u_2}{4 e^4 R_{\rm TS} B_2^2}\right) I^{-1} (vz^2)^{-1/3} \,, \tag{2.18}$$

where

$$I = \int_1^z \frac{x^4}{(vx^2)^{10/3}} dx \tag{2.19}$$

The definition of u_2, z and $v(z)$ are the same as the Eq. (2.8). The injection spectrum, $n_{\rm s}$, at the termination shock is written by

$$n_{\rm s}(E) = A_{\rm w} (E + E_0)^{-2.4} \exp\left(-\frac{E}{2.5 \text{ PeV}}\right). \tag{2.20}$$

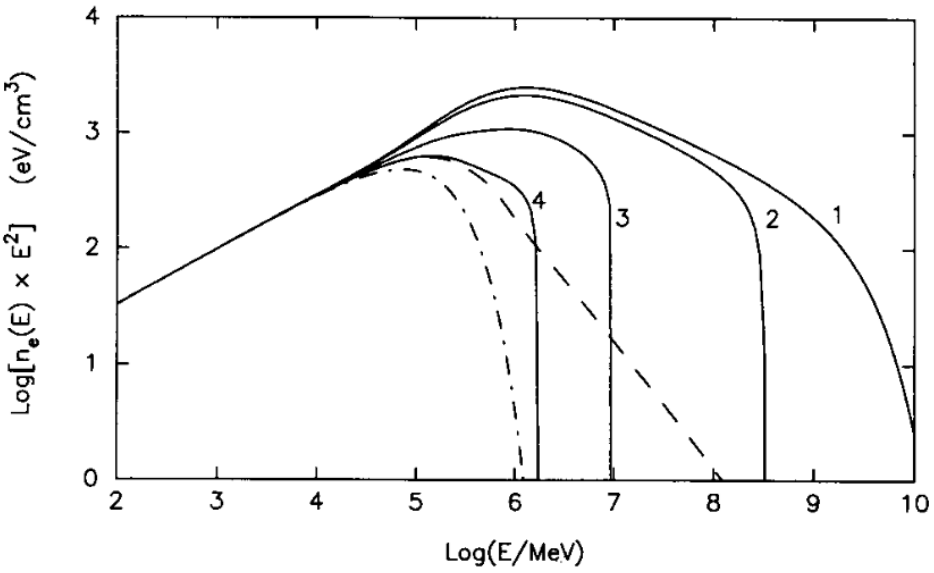

Figure 2.4 The total electron spectrum, $n_{\rm tot} = n_{\rm w} + n_{\rm re}$ at different distance $r \leq R_{\rm TS}$ for $\sigma = 0.005$: $r = R_{\rm TS}$ (curve 1); $r = 2R_{\rm TS}$ (curve 2); $r = 4R_{\rm TS}$ (curve 3); $r = 10R_{\rm TS}$ (curve 4). The dot-dashed line corresponds to the spectrum of the "radio electrons". The dashed line shows the electron spectrum averaged over the entire nebula (Atoyan and Aharonian, 1996).

$A_{\rm w}$ is the normalization constant and $E_0 = 250$ GeV provides the spectral flattening below E_0 (Atoyan and Aharonian, 1996). $A_{\rm w}$ is determined by the spindown luminosity:

$$L_{\rm SD} \simeq 4\pi R_{\rm TS} u_2 mc^3 \bar{E} \int n_{\rm s} {\rm d}E \tag{2.21}$$

where $\bar{E}$ is the mean electron energy of the pulsar wind, $\bar{E}/mc^2 \sim \gamma_1 \sim 10^6$ (Kennel and Coroniti, 1984b). Thus, the spectral flattening is naturally expected below γ_1 in the MHD framework. The spectral transition between the "radio electrons" and "wind electrons" is appeared at the IR/optical band. The detailed spectral analysis in this energy band allows one to accurately derive E_* and E_0.

The calculated total electron energy spectra ($n_{\rm tot} = n_{\rm re} + n_{\rm w}$) at various distances are shown in Figure 2.4. In this calculation, the magnetization parameter $\sigma = 0.005$ was assumed. The dot-dashed line represents the contribution of the "radio electrons" and they are dominant component at low energies ($\lesssim 100$ GeV). The maximum energy of particles in the "wind electrons" component achieves 2.5 PeV at the termination shock. Because of the synchrotron and adiabatic losses, the maximum energy decreases when particles get advected downstream in the nebula. The obtained distribution of electrons allows one to calculate the volume integrated emission. The calculated spectral energy distribution (SED) is shown in Figure 2.5 (Atoyan and Aharonian, 1996). A combination of the "radio electrons" and "wind electrons" can explain the broadband SED over 20 decades. In addition, the spatial extension of the Crab Nebula in UV, X-ray and TeV energy band can be reproduced well (H. E. S. S.

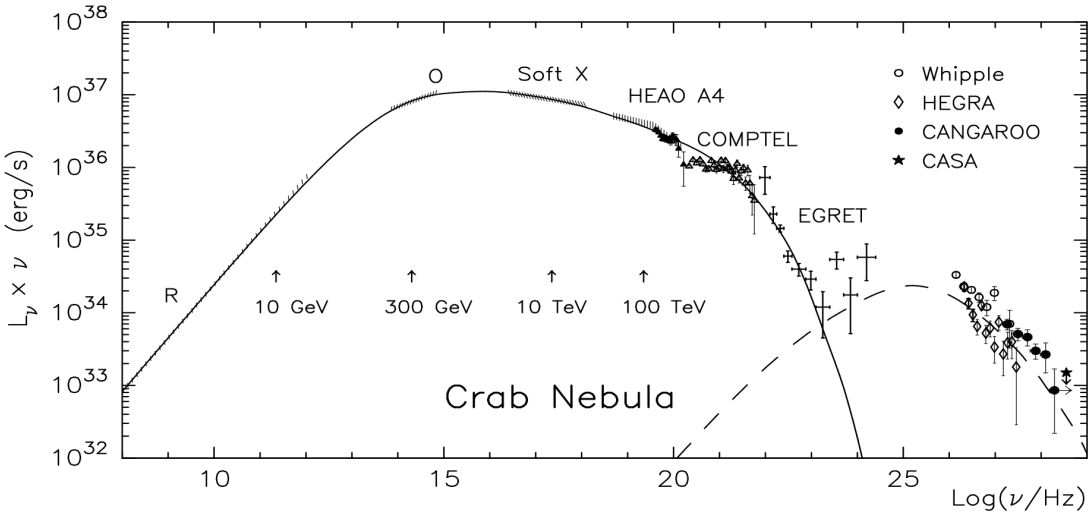

Figure 2.5 The non-thermal radiation spectrum of the Crab Nebula. The solid line shows the synchrotron component and the dashed line is the inverse Compton component. Figure is taken from Aharonian and Atoyan (1998).

Collaboration et al., 2019a; Madsen et al., 2015). The required maximum energy of "wind electrons" is at least PeV, so the Crab Nebula has been considered to be one of the most efficient electron accelerators in the universe.

However, 1D MHD models can not explain the complex structures seen in the center part of the nebula: jet, torus and wisp which are revealed by the high-resolution telescopes, e.g. *Hubble Space Telescope* (HST) and *Chandra* (See Figure 2.1). In addition, 1D MHD models require the low magnetization, $\sigma \simeq 0.003$ (Kennel and Coroniti, 1984b) while the initial magnetization (i.e., close to the light cylinder) is expected to be large, $\sigma \gg 1$ (e.g., Arons, 2012). This discrepancy is known as the "σ problem" and indicates the energy conversion from electro-magnetic energy to the particle kinetic energy must be occurred at the pulsar wind region. 2D MHD models that account for the anisotropic of the pulsar wind allow one to better understand the morphology seen in the Crab Nebula. The oblique termination shock originated from the anisotropic pulsar wind naturally make the torus structure observed in X-ray (e.g. Weisskopf et al., 2000; Bogovalov and Khangoulyan, 2002). Such anisotropy also makes the collimated flow due to the magnetic hoop stress in the polar region, which results in the jet structure. (e.g. Lyubarsky, 2002a; Bogovalov and Khangoulian, 2002a). Recent multi-dimensional MHD simulations confirm this pictures (e.g., Olmi et al., 2016; Porth et al., 2017), as they produce the jet-torus morphology originated from the anisotropic pulsar wind. The properties of wisps, e.g. their emergence and the velocity can be also explained by the multi-dimensional MHD simulations (see, e.g., Volpi et al., 2008; Olmi et al., 2015). In addition, 3D MHD simulations allow one to describe the randomization of the magnetic field. This leads a significant magnetic field dispersion inside the PWN

and provides a possible solution for the "σ problem" (Porth et al., 2014).

2.2 Radiation Mechanism

The accelerated particles, whose distribution is typically characterized by the power-law function, emit the non-thermal radiation. The parents particles yield broadband radiation (from radio to TeV gamma-ray band) spectrum via various radiation mechanisms. One needs to identify the radiation mechanism in order to interpret observations. In PWNe, there are two dominant radiation mechanisms, the synchrotron radiation and inverse Compton scattering. In this section, we provide the basic explanation of these radiation mechanism. In this section, we describe electron energy and photon energy as E and ε, respectively.

2.2.1 Synchrotron Radiation

Relativistic charged particles interacting with a magnetic field emit the synchrotron radiation. Since particles are accelerated in a magnetized medium, the synchrotron emission is an essential process in the high energy astrophysics. Here, we briefly explain basic features of the synchrotron radiation.

The synchrotron spectrum from single electron is given by

$$\frac{\mathrm{d}N_{\mathrm{SYN}}}{\mathrm{d}\varepsilon \mathrm{d}t} = \frac{\sqrt{3}}{2\pi}\frac{e^3 B}{m_{\mathrm{e}} c^2 \hbar \varepsilon} F(x) \,, \tag{2.22}$$

where $\hbar$, m_{e}, e, c, and B represent the Dirac constant, the electron mass, the elementary charge, the speed of light and the strength of the magnetic field, respectively. The critical energy ε_{c} is defined as

$$\varepsilon_{\mathrm{c}} \equiv \frac{3e\hbar B}{2m_{\mathrm{e}} c}\left(\frac{E}{m_{\mathrm{e}} c^2}\right)^2 \,, \tag{2.23}$$

and x is defined as $x \equiv \varepsilon/\varepsilon_{\mathrm{c}}$. The function $F(x)$ is given by

$$F(x) = x\int_{\xi}^{\infty} K_{5/3}(\xi)\mathrm{d}\xi \tag{2.24}$$

where $K_{5/3}(\xi)$ represents the modified Bessel function of 5/3 order. For the case of chaotic magnetic fields, one needs to average over the pitch angle, θ which is the angle between the direction of magnetic field and the velocity of the electron (Aharonian et al., 2010):

$$G(x) = \int \sin\theta F\left(\frac{x}{\sin\theta}\right)\frac{\mathrm{d}\Omega}{4\pi} = \frac{1}{2}\int_0^{\pi} F\left(\frac{x}{\sin\theta}\right)\sin^2\theta \mathrm{d}\theta = x\int_{\xi}^{\infty} K_{5/3}(\xi)\sqrt{1-\frac{x^2}{\xi^2}}\mathrm{d}\xi \,. \tag{2.25}$$

Although Eq. (2.25) is described by a combination of modified Bessel functions, Aharonian et al. (2010) proposed an approximation, which does not contain special functions, as follows:

$$G(x) = \frac{1.808x^{1/3}}{\sqrt{1+3.4x^{2/3}}}\frac{1+2.21x^{2/3}+0.347x^{4/3}}{1+1.353x^{2/3}+0.217x^{4/3}}e^{-x} \,. \tag{2.26}$$

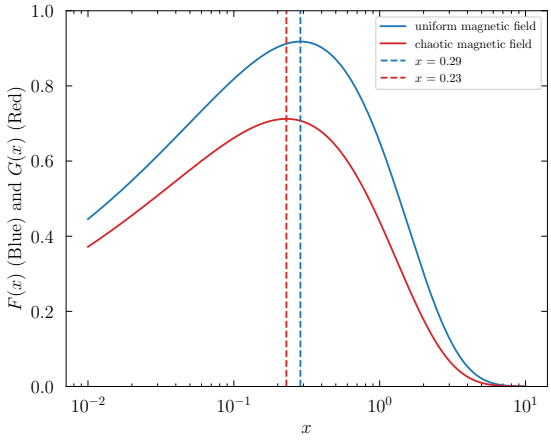

Figure 2.6 The synchrotron spectrum of a charged particle.

This formula provides an accuracy better than 0.2 % over the entire range of variable x. The function $F(x)$ and $G(x)$, which show the spectral shape of synchrotron radiation in uniform and chaotic magnetic fields, are shown in Figure 2.6. As seen in Figure 2.6, the peak value of $F(x)$ and $G(x)$ is achieved at $\varepsilon = 0.29\varepsilon_c$ and $\varepsilon = 0.23\varepsilon_c$, respectively. In the case of so called "νF_ν" plot, the peak energy is shifted toward a higher energies: $\varepsilon \simeq 1.3\varepsilon_c$ and $\varepsilon \simeq 1.2\varepsilon_c$. The intensity of $F(x)$ and $G(x)$ sharply declined above these energies.

The peak synchrotron photon energy from single electron in chaotic magnetic fields can be calculated by

$$\varepsilon_{\rm SYN} \simeq 6\left(\frac{B}{100\,\mu{\rm G}}\right)\left(\frac{E}{1\,{\rm TeV}}\right)^2 {\rm eV}\,. \tag{2.27}$$

The total synchrotron power, averaged over the pitch angle, is given by.

$$P_{\rm SYN} = \frac{4}{3}\sigma_{\rm T}\beta^2 c w_{\rm B}\left(\frac{E}{m_e c^2}\right)^2 {\rm eV}\,. \tag{2.28}$$

where β, $\sigma_{\rm T} = \frac{8\pi r_e^2}{3}$, $w_{\rm B} = \frac{B^2}{8\pi}$ is the velocity of the electron in unit of the speed of light, the Thomson cross section and the energy density of a magnetic field, respectively. r_e represents the classical electron radius.

The cooling time of the synchrotron emission is given by

$$t_{\rm SYN} = \frac{E}{P_{\rm SYN}} = \frac{6\pi m_e^2 c^3}{\sigma_{\rm T} E B^2} = 4\times 10^{10}\left(\frac{E}{1\,{\rm TeV}}\right)^{-1}\left(\frac{B}{100\,\mu{\rm G}}\right)^{-2} {\rm sec} \tag{2.29}$$

If the parent electrons form a power-law distribution:

$$\frac{{\rm d}N}{{\rm d}E} = AE^{-s}\,,$$

the synchrotron spectrum is also power-law energy distribution. The observed photon index $\Gamma_{\rm SYN}$ of synchrotron spectrum is related with the index of the electron distribution as follows:

$$s = 2\Gamma_{\rm SYN} - 1\,. \tag{2.30}$$

2.2.2 Inverse Compton Scattering

The accelerated electrons interact not only with magnetic field but also with radiation fields. Electrons transfer a fraction of their energy to a target photon, which results in production of high-energy emission. This process is called the inverse Compton (IC) scattering. The interaction through IC provided one of the principal gamma-ray production processes in astrophysics.

The total power emitted from a single electron via IC is

$$P_{\rm IC} = \frac{4}{3}\sigma_{\rm T}\beta^2 c w_{\rm ph}\left(\frac{E}{m_{\rm e}c^2}\right)^2\,, \tag{2.31}$$

where $w_{\rm ph}$ is the energy density of seed photons. Note that Eq. (2.31) is valid when the energy of the seed photon in the rest frame of the electron is smaller than the rest mass energy of the electron ($\varepsilon_{\rm s}' \ll m_{\rm e}c^2$) (Thomson limit). Here, $\varepsilon_{\rm s}$ represents the seed photon energy and a prime means parameters in the electron rest frame. The seed photon energy in the electron rest frame is $\varepsilon_{\rm s}' = \gamma\varepsilon_{\rm s}$ and the photon energy does not change in the Thomson regime after the scattering. Therefore the enhanced photon energy by one scatter is $\sim \gamma^2\varepsilon_{\rm s}$. In the case of $\varepsilon_{\rm s}' \gg m_{\rm e}c^2$, the quantum effects have to be introduced and the cross section decreases. This effect is called the Klein-Nishina (KN) effect which makes the gamma-ray spectrum steep at high energy.

The typical IC energy averaged by the scatter angle can be calculated by

$$\varepsilon_{\rm IC} = 5\left(\frac{\varepsilon_{\rm s}}{10^{-3}\ {\rm eV}}\right)\left(\frac{E}{1\ {\rm TeV}}\right)^2\ {\rm GeV}\,. \tag{2.32}$$

Here, we assumed the Thomson regime. Using Eq. (2.27) and (2.32), we can derive the relation between the energies of synchrotron and IC photons emitted by the same electron:

$$\varepsilon_{\rm SYN} = 0.1\left(\frac{B}{100\ \mu{\rm G}}\right)\left(\frac{\varepsilon_{\rm IC}}{1\ {\rm TeV}}\right)\left(\frac{\varepsilon_{\rm s}}{1\times10^{-3}\ {\rm eV}}\right)^{-1}\ {\rm keV}\,. \tag{2.33}$$

This implies the electrons which produce the synchrotron emission around X-ray can also emit TeV gamma-ray emission via IC channel. In addition, the ratio between Eq. (2.28) and (2.31) is determined by the ratio between the energy density of the magnetic field and the energy density of seed photons.

$$\frac{P_{\rm IC}}{P_{\rm SYN}} = \frac{w_{\rm ph}}{w_{\rm B}}\,. \tag{2.34}$$

If we know or assume the energy density of the target photon, the ratio of the intensity of the synchrotron and IC components defines the strength of the magnetic field.

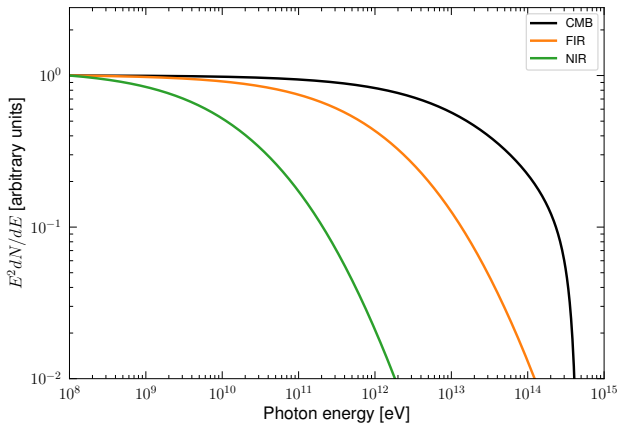

Figure 2.7 The inverse Compton spectrum produced by the power-law electron spectrum with $s = 3$. The temperature of the up-scattering thermal radiation is assumed to be 2.7 K (black line), 70 K (orange line) and 5000 K (green line).

In order to calculate the spectrum via IC, one needs to know the cross-section of the IC process. The scattered photon spectrum per electron is given by:

$$\frac{\mathrm{d}N_{\mathrm{IC}}}{\mathrm{d}\varepsilon \mathrm{d}t} = \frac{2\pi r_e^2 c}{E} \frac{n(\varepsilon_s)\mathrm{d}\varepsilon_s}{\varepsilon_s} \left[2q \ln q + (1+2q)(1-q) + \frac{1}{2} \frac{(\Gamma_\varepsilon q)^2}{1+\Gamma_\varepsilon q}(1-q) \right] \tag{2.35}$$

where $\Gamma_\varepsilon = 4\varepsilon_s E/(m_e c^2)^2$, $q = \varepsilon/\Gamma_\varepsilon(E-\varepsilon)$, and E represents the initial electron energy (Blumenthal and Gould, 1970). The parameter Γ_ε determines the transition from Thomson regime ($\Gamma_\varepsilon \ll 1$) to KN regime ($\Gamma_\varepsilon \gg 1$). In the Thomson regime, the observed spectral index Γ_{IC} from the power-law distributed electrons is written by

$$s = 2\Gamma_{\mathrm{IC}} - 1\,, \tag{2.36}$$

while the KN effect makes the spectrum steeper. The spectral change due to the KN effect is shown in Figure 2.7 for each background component relevant for the gamma-ray emission in the Crab Nebula:2.7 K (black line), 70 K (orange line) and 5000 K (green line). One can see a clear dependence on the target field temperature: the higher temperature, at the low energy spectral steepening starts.

As seen in Eq. (2.35), the seed photon distribution must be defined to calculate the IC spectrum. In the case of the Crab Nebula, one of the most important target is the synchrotron photons in the nebula. This process, relativistic electrons scatter up the synchrotron photon, is called synchrotron-self-Compton (SSC). The SSC in the Crab Nebula is different from the standard SSC seen in e.g. blazars. In the case of the standard SSC, relativistic electrons emit the synchrotron and the same electrons scatter up the synchrotron photon. On the other hand, the synchrotron photons are produced not only by "wind electrons" but also by "radio electrons" in the Crab Nebula. The gamma-ray emission above $\sim$ 100 GeV are mainly produced by the interaction between the "wind electrons" and the

synchrotron photon originated from the “radio electrons”. Since the “radio electrons” are almost uniformly distributed in the nebula, the magnetization parameter which determines the distribution of the magnetic field at the downstream is not important (Atoyan and Aharonian, 1996).

2.3 Gamma-ray Emission from the Crab Nebula

The observed spectrum in gamma-ray regime shows two components: one is the synchrotron component which dominates below $\sim$ 450 MeV and the other is the IC component which becomes significant above $\sim$ GeV. The Crab Nebula is known to be an only PWN which synchrotron radiation extends up to $\sim$GeV energy band. The connection between *COMPTEL* data and *Fermi*–LAT data allows one to derive the synchrotron cut-off energy, 97 $\pm$ 12 MeV (Abdo et al., 2010a).

This high-energy cut off of the synchrotron radiation is close to the theoretical limit under the ideal MHD condition, $\sim$ 100 MeV (also see Section 2.4.2) and indicates the Crab Nebula is the extremely efficient electron accelerator. The spectral energy distribution of the Crab Nebula in gamma-ray regime is shown in Figure 2.8 left panel. Interestingly, the synchrotron component is not stationary and causes a rapid and strong enhancement of fluxes called flares (Tavani et al., 2011; Abdo et al., 2011). The observational results and the theoretical interpretations of the flares are summarized in the Section 2.4.

The IC component which becomes dominant above $\sim$1 GeV were discovered in 1989 with the Whipple telescope (Weekes et al., 1989). The Crab Nebula is the brightest and persistent source in TeV energy range and basically all gamma-ray telescopes observe the Crab Nebula due to a cross calibration of detectors(e.g Aliu et al., 2014; Aleksić et al., 2015; H. E. S. S. Collaboration et al., 2014; Abeysekara et al., 2019; Amenomori et al., 2019). The high-quality data from *Fermi*–LAT and TeV gamma-ray telescopes enables one to estimate the averaged magnetic field based on the comparison of the X-ray synchrotron and TeV IC radiation. The estimated magnetic fields is B = 100–200 μG (Abdo et al., 2010a) and this is consistent with the prediction by the 1D MHD calculation (Atoyan and Aharonian, 1996). In 2019, two ground telescope mission, Tibet Air Show Gamma Experiment (*Tibet ASγ*) and High Altitude Water Cherenkov (*HAWC*) Gamma-Ray Observatory detected above 100 TeV gamma rays from Crab Nebula (Abeysekara et al., 2019; Amenomori et al., 2019). The observed spectrum with *Tibet ASγ* is shown in Figure 2.8 right panel. This is the first light of the gamma-rays above 100 TeV.

2.4 Gamma-ray Flare Observed in the Crab Nebula

The Crab Nebula is fairly bright source and treated as a “standard candle” in the field of the high energy astrophysics (X-ray and TeV gamma-ray bands). However, spaceborne gamma-ray telescopes (*Fermi*-LAT and *AGILE*) revealed that $\sim$ 100 MeV emission from the Crab Nebula displays day-scale variabilities, dubbed as GeV flares. The presence of flares indicates the Crab Nebula is never "standard

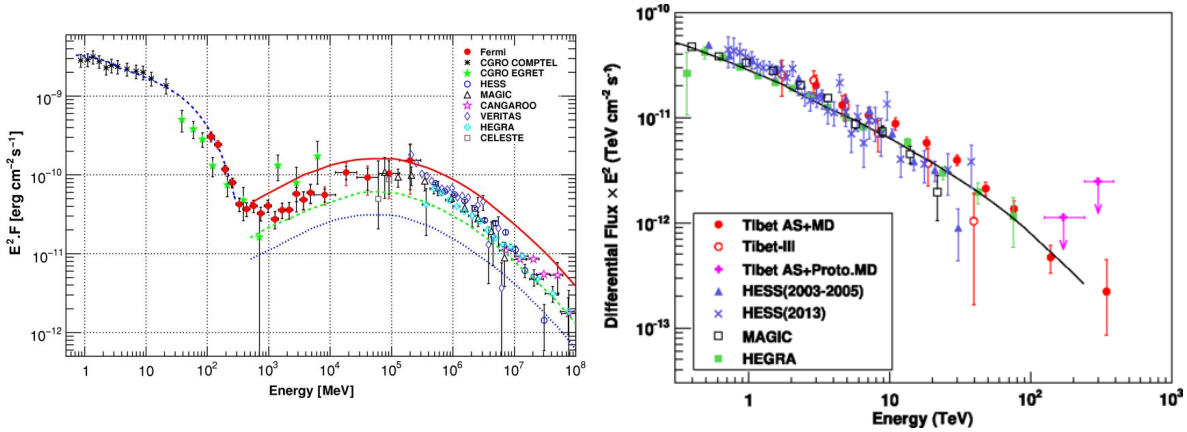

Figure 2.8 left: Spectra energy distribution of the Crab Nebula from ∼ 1 MeV to ∼ 100 TeV (Abdo et al., 2010a). The synchrotron component is shown in the blue dashed line. The IC components based on Atoyan and Aharonian (1996) are overlaid assuming three averaged magnetic field: 100 μG (red line), 200 μG (dashed green line) and 300 μG (dotted blue line). The IC components indicates the averaged magnetic field in the nebula is B = 100–200 μG. right: Spectra energy distribution of the Crab Nebula above ∼ 100 GeV. The data points observed by *Tibet ASγ* is shown in red (Amenomori et al., 2019).

candle" in the ∼ 100 MeV. In this section, we review the recent results of the time variability in the Crab Nebula from observational and theoretical points of view. The comprehensive review is done by Bühler and Blandford (2014)

2.4.1 Observational Results

Tavani et al. (2011) and Abdo et al. (2011) reported the rapid gamma-ray flux enhancement (hereafter called flares) from the direction of the Crab pulsar and Nebula system. The pulsed component was stable during the flares and the enhanced gamma-ray should be originates from the Crab Nebula. The peak flux of flares shows $> 3.5 \times 10^{-6}$ photons cm^{-2} s^{-1} while the definition of flares are somehow arbitrary because of the statistical fluctuation (Bühler and Blandford, 2014). The 2011 April flare which is most examined among flares revealed the interesting activity of flares (Striani et al., 2011; Buehler et al., 2012). The light curve of the 2011 April flare is shown in Figure 2.9. Its extremely large flux enabled to measure the flux down to ∼ 20 minutes time bins (shorter than one orbit time scale) and the measured doubling time of the flare showed ≤ 8 hours. In addition, the spectral evolution during the flare was measured. The temporal evolution of the SED during the 2011 April flare is shown in Figure 2.10. The detailed spectral analysis suggests the new component was emerged (e.g. see period 7 in Figure 2.10). The observed spectrum of the flare component was characterized by the power-law with the exponential cut off, $\propto \varepsilon^{-\Gamma}\exp(-\varepsilon/\varepsilon_{\rm cut})$, where ε represents photon energy. The spectral index of the flare component shows the constant value, $\Gamma = 1.27 \pm 0.12$, while the cut-off energy, $\varepsilon_{\rm cut}$, and flux strongly vary during flare. The cut-off energy represented $\varepsilon_{\rm cut} = 375 \pm 26$ MeV

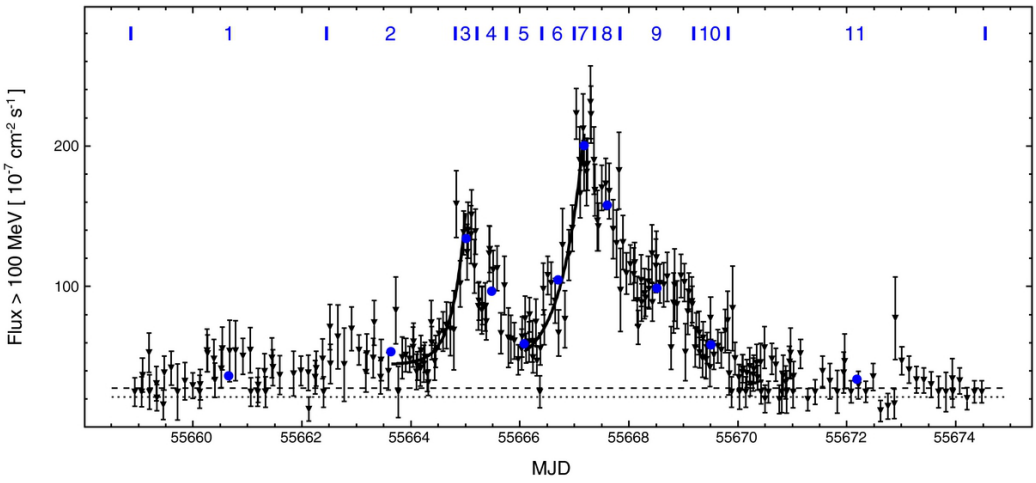

Figure 2.9 The light curve of the Crab Nebula above 100 MeV observed by the *Fermi*–LAT during 2011 April flare (Buehler et al., 2012). The data points represent the sum of the radiation of the Crab Nebula and the Crab pulsar. The dotted line and the dashed line shows the averaged flux of the synchrotron component of the Crab Nebula and the averaged flux of the sum of the Crab pulsar and inverse Compton component of the Crab Nebula. The blue numbers represent the time interval where the fluxes become constant within the statistical uncertainties.

at the maximum flare and the isotropic luminosity at the peak of the flare (period 7 in Figure 2.9) is $L_{\rm iso} \simeq 4 \times 10^{36}$ erg s^{-1}, which corresponds to $\sim$ 1% of the spindown luminosity of the Crab pulsar. The similar analysis was performed for the 2013 March flare by Mayer et al. (2013). They reported the variability timescale of the flare was determined to be $\sim$ 5 hr time and the cut-off energy at the maximum flare was $\varepsilon_{\rm cut} = 484^{+409}_{-166}$ MeV.

Striani et al. (2013) reported the flux enhancement during 1–2 week scale, called "wave" (see Figure 2.11). The intensity of the "waves" is weaker than flares and they seem to be intermediate phenomena between the stationary emission and flares. The released energy by "waves" is a few percent of the pulsar spindown luminosity and comparable with flares. Striani et al. (2013) argued that flares and "waves" are attributed with the same class of plasma instabilities.

The current GeV gamma-ray telescopes do not spatially resolve the Crab Nebula. In order to identify the origin of flares, the multi-wave-length observations must be required. The multi-wave-length campaign was performed by the *Chandra* (X-ray), Keck (near infrared) and Very Large Telescopes (radio) during the 2011 April flare. However flux increasing could not be detected by any observations and only upper limit from infrared observation was obtained (Weisskopf et al., 2013). Rudy et al. (2015) investigated the relation between the inner knot and the gamma-ray flux for three flare by the *Chandra*, Keck and HST (optical). The inner knot, as known as knot 1, discovered by Hester et al. (1995) is a compact source (a few arcmin) and located the southeast from the Crab pulsar. The inner knot is considered to be the result of the emission from relativistically moved plasma in the down-

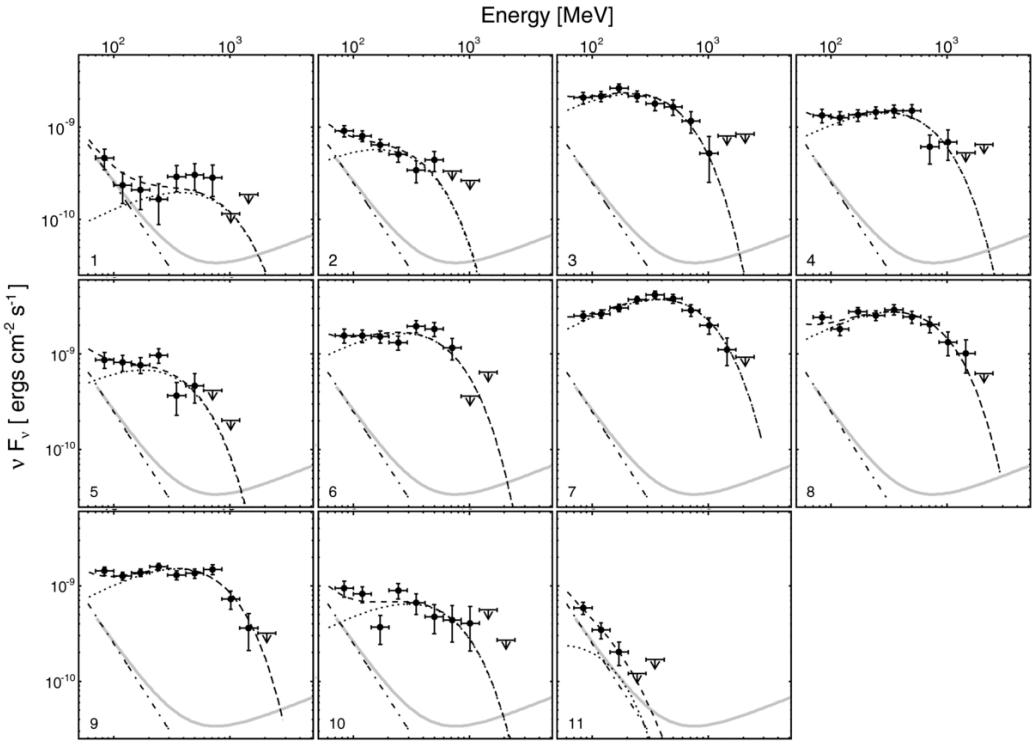

Figure 2.10 The time evolution of the spectral energy distribution during the 2011 April flare (Buehler et al., 2012). The number located in the bottom left in each time window (1-11) corresponds to the number described in the Figure 2.9. The dotted line, dash-dotted line and dashed line show the flare component, the synchrotron component of the synchrotron and the sum of both components, respectively. The grey line represents the time-averaged spectrum of the Crab Nebula.

stream of the termination shock (Yuan and Blandford, 2015; Lyutikov et al., 2016). If the inner knot is a site of flares, some synchronized activities are expected. However there was no relation between the pulsar-knot separation distance and gamma-ray flare occurrence.

2.4.2 The Difficulties of the Gamma-ray Flare

After the detections of flares, many theoretical works have been done, however the origin of gamma-ray flares is still missing. What are difficulties of gamma-ray flares? One difficulty is the observed synchrotron cut-off energy, $\varepsilon_{\rm cut} = 375 \pm 26$ MeV in the 2011 April flare and $\varepsilon_{\rm cut} = 484^{+409}_{-166}$ MeV in the 2013 March flare. The cut-off energy of the synchrotron emission corresponds to the maximum energy of accelerated electrons, if the energy loss is dominated by the synchrotron radiation. In this case, the maximum electron energy can be estimated by the balance between the time scale of the acceleration and the synchrotron loss. The acceleration time scale with electron energy, E, is written by

$$t_{\rm acc} = \eta(E)\frac{r_g}{c}\,, \tag{2.37}$$

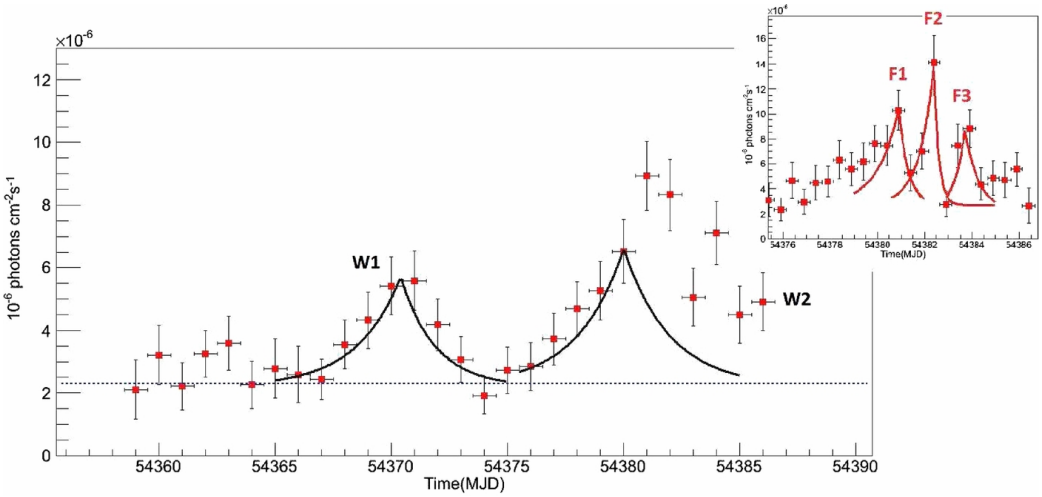

Figure 2.11 The 1 day binned lightcurve of the 2007 September and October Crab Nebula flare detected by *AGILE* (Striani et al., 2013). The upper-right window represents the 12 hours binned light curve around the flare. This episode can be divided into the "wave" (black lines) and flares (red lines).

where $\eta(E)$ and $r_g = \frac{E}{eB}$ represent the acceleration efficiently and the gyro radius, respectively. Under the ideal MHD condition, which indicates the static electric field is smaller than the magnetic field, $\eta(E)$ should be greater than unity. If we assume the most dominant energy loss process is due to the synchrotron radiation, the condition $t_{\rm SYN} = t_{\rm acc}$ yields the maximum synchrotron critical energy (Aharonian et al., 2002; Arons, 2012, also see Eq. 2.29):

$$\varepsilon_{\rm max} = \frac{27}{8}\alpha^{-1}\eta^{-1}m_e c^2 \simeq 236\eta^{-1}\ {\rm MeV}\,, \tag{2.38}$$

where α is the fine structure constant. This energy is called "synchrotoron burn-off cut-off energy" and does not depend on the strength of the magnetic field. The observed cut-off energy clearly exceeds the maximum energy in the MHD regime.

Another issue arises from the short time variability, which is the typically day scale (Bühler and Blandford, 2014). The upper limit of emission region is determined by the light crossing time, $l < ct_{\rm var} \sim 1\times10^{-3}\left(\frac{t_{\rm var}}{1\ {\rm day}}\right)$ pc $\ll 0.1$ pc. Here, $t_{\rm var}$ is observed variable time scale. It means that the flare region must be compact compared with the size of the Crab Nebula, while the isotropic power of the flares is quite large, close to 1% of the spindown luminosity for the 2011 April flare. It is challenging to explain this phenomenon, because such a large fraction of the available energy is released as the gamma-ray synchrotron emission.

In addition, the fast variability of flares requires a very strong magnetic field. From Eqs. (2.27) and (2.29), one can derive the relation between the synchrotron cooling time, $t_{\rm SYN}$, and the typical

synchrotron photon energy, $\varepsilon_{\rm SYN}$ as follows:

$$t_{\rm SYN} = 100 \left(\frac{\varepsilon_{\rm SYN}}{100\ {\rm MeV}} \right)^{-1/2} \left(\frac{B}{100\ \mu{\rm G}} \right)^{-3/2} {\rm d}\,. \tag{2.39}$$

In order to explain the hour/day-scale variability, the strong magnetic field $\gtrsim 1$ mG is required. Such a high magnetic field exceed the averaged magnetic field in the nebula (e.g. Atoyan and Aharonian, 1996) while the recent 3D MHD simulation indicates such a strong magnetic field can exist at the base of the jet (Porth et al., 2014).

2.4.3 Theoretical Model

These observational results of flares do not reconcile to the MHD models and imply production sites of flares to operate under very special circumstances. In order to exceed the "synchrotoron burn-off cut-off energy", there are three possibilities:

(i) Magnetic Reconnection: particles are accelerated via the magnetic reconnection
(ii) Doppler Boosting: flare sites relativistically move.
(iii) Small-Scale Magnetic Turbulence: stochastic magnetic field is present in the acceleration and radiation region.

Here, we briefly describe these scenarios.

(i) Magnetic Reconnection

Magnetic reconnection is the topological reconfiguration of the magnetic field in plasma and the magnetic energy is released by annihilating the field lines. The ideal MHD condition breaks down and $\eta < 1$ can be realized in the reconnection layer. The schematic view of the acceleration via the magnetic reconnection is shown in Figure 2.12. Electrons injected into the current sheet are accelerated by the electric field induced in the reconnection layer (in the direction of z axis in Figure 2.12). Therefore the reconnection layer works as a linear accelerator (Uzdensky et al., 2011). If a trajectory of the electrons is fully confined inside the layer, the perpendicular magnetic filed, B_x, for the electrons becomes smaller, whereas the strength of the electric field is constant. This means that the acceleration efficiency does not change and the synchrotron radiation loss becomes smaller. In this case, the maximum energy of the electrons is limited by the length of the reconnection layer and the synchrotron radiation can exceed the "burn-off" limit. In addition, the synchrotron loss time scale of such energetic electrons is expected to be shorter than their gyro period. Therefore, one can naturally interpret that the enhancement of the gamma-ray flux is due to a strong beaming effect. Recent 2D particle-in-cell (PIC) simulations can explain the observed flare features: exceeding the synchrotron "burn-off" limit, the hard spectrum, day/hour-scaled variability and the correlation between the gamma-ray flux and the cut-off energy (Cerutti et al., 2013). In addition, Sironi and Spitkovsky (2014) performed the both

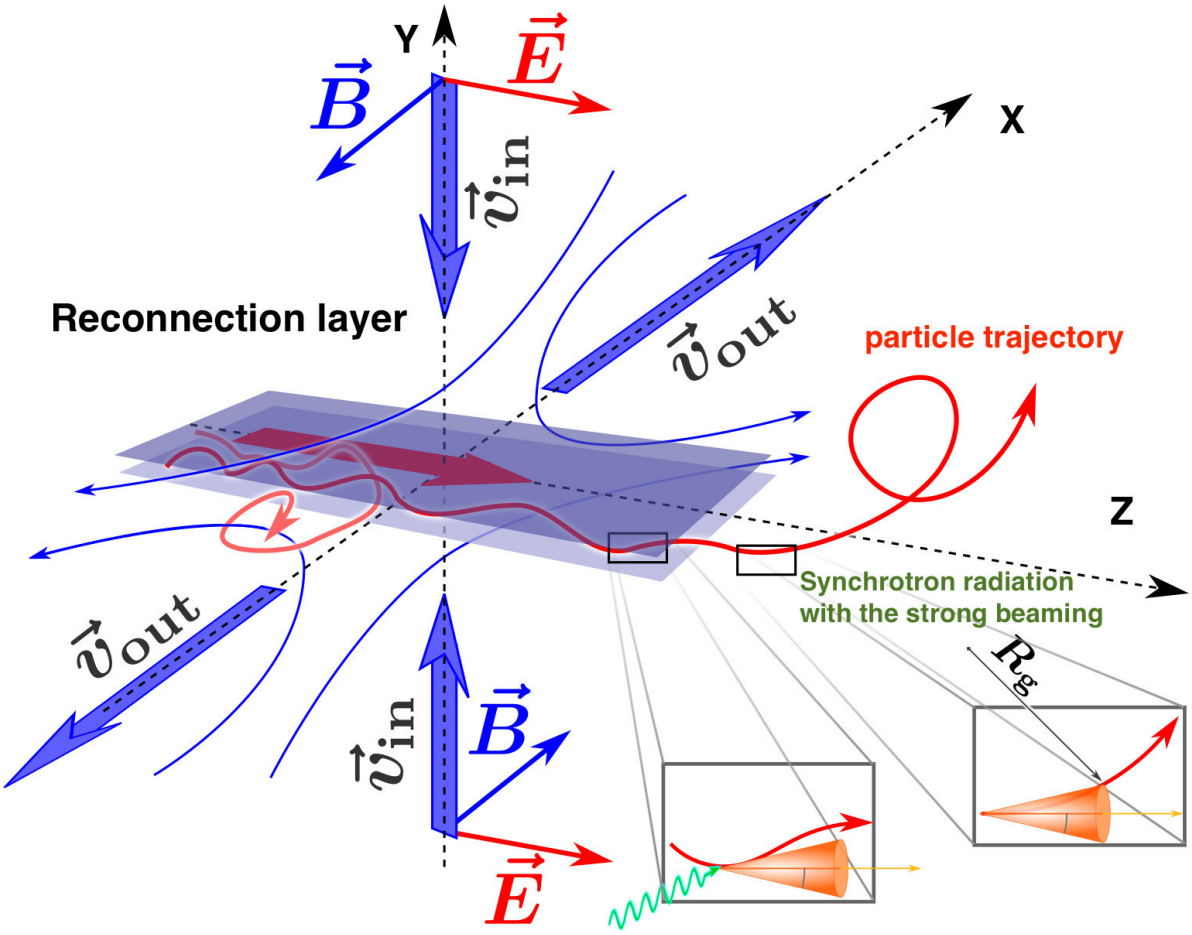

Figure 2.12 The schematic view of the magnetic reconnection. The incoming Poynting flux is dissipated in the reconnection layer and the outflow plasma is ejected to the direction of x-axis. The electron which follow a relativistic Speiser orbit is accelerated by the electric field E_z in the reconnection layer. Then the electron escapes from the layer and efficiently emits the synchrotron radiation. (Credit: Dmitry Khangulyan, with modifications by the author.)

2D and 3D kinetic PIC simulations in the relativistic pair plasmas to examine the particle distribution via the magnetic reconnection. They found that the non-thermal distributions are generally formed for both 2D and 3D cases. The power-law slope, s, of the electron distribution depends on the magnetization, $s \sim 4$ for $\sigma = 1$ to $s \leq 1.5$ for $\sigma \geq 50$. Such a hard electron spectrum is consistent with the observed spectral index,, in the 2011 April flare, $s = 2\Gamma - 1 \sim 1.5$.

(ii) Doppler Boosting

Another scenario for flares origin is from the relativistic moving fluid. If a fluid element relativistically moves, the radiation proprieties are modified by the Doppler boost. The photon energy, ε, and the time

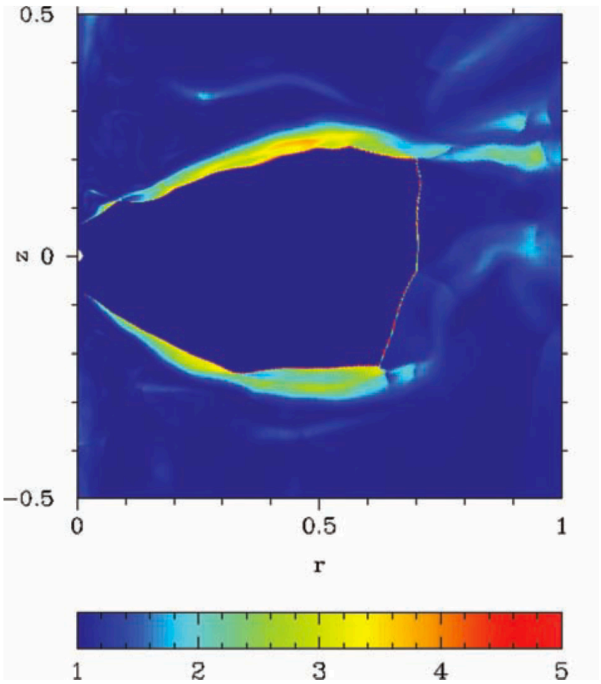

Figure 2.13 Termination shock in the MHD simulation performed by Camus et al. (2009). The color bar shows the flow bulk Lorentz factor. The figure is taken from Komissarov and Lyutikov (2011).

duration, $t_{\rm var}$, in the laboratory frame are written as

$$\varepsilon = \delta\varepsilon' \tag{2.40}$$

$$t_{\rm var} = \frac{t'_{\rm var}}{\delta}\,, \tag{2.41}$$

where ε' and $t'_{\rm var}$ are the photon energy and the flare duration in the fluid co-moving frame, respectively. Here, δ is Doppler factor:

$$\delta \equiv \frac{1}{\gamma(1-\beta\cos\theta)}\,, \tag{2.42}$$

where γ is the fluid bulk Lorentz factor in the downstream and θ is the angle between the line of sight and the velocity vector of the fluid bulk motion. The Doppler boost allows the reduction of the maximum photon energy and relaxes the constraint on the size of the flaring region. Recent MHD simulations suggests that an oblique termination shock can produce relativistic flow ($\gamma \sim 5$) at high latitudes (Camus et al., 2009, also see Figure 2.13). In this regard, the inner knot observed by the HST (Hester et al., 1995) is a promising candidate because the recent 3D MHD simulations revealed that the radiation from the region where the flow is characterized by a high Lorentz factor at the downstream can be observed as a compact knot (Porth et al., 2014). However, as we mentioned in Section 2.4.1,

the multi-wave-length observations suggested the inner knot as a flare origin is less promising.

(iii) Small-Scale Magnetic Turbulence

If small scale magnetic turbulence is present, synchrotron spectra are significantly changed. The "small" is determined by the typical magnetic field fluctuation length (λ_B) and the non-relativistic gyro radius ($\lambda_{\rm ph} = \frac{m_{\rm e}c^2}{eB}$). For $\lambda_{\rm ph} \gg \lambda_B$, the radiation is produved in a different regime, called jitter radiation (Kelner et al., 2013). The peak energy is shifted by a factor $\lambda_{\rm ph}/\lambda_B$ from the critical synchrotron energy (see Eq. (2.23)). The minimum scale of the turbulence is imposed by the Landau damping (H. E. S. S. Collaboration et al., 2019b):

$$\frac{\lambda_{\rm B}}{\lambda_{\rm ph}} = \sqrt{\frac{\epsilon_{\rm e}}{4\pi e^2 n_{\rm e}}}\frac{eB}{m_e c^2} = \frac{\epsilon_{\rm e}}{m_{\rm e}c^2}\sqrt{\frac{B^2}{4\pi\epsilon_{\rm e} n_{\rm e}}} \tag{2.43}$$

where $n_{\rm e}$ and $\epsilon_{\rm e}$ are number density of electrons and mean energy per electron, respectively. In the case of the Crab Nebula, $\frac{\epsilon_{\rm e}}{m_{\rm e}c^2}$ corresponds to the wind bulk Lorentz factor and significantly larger than unity , while $\frac{B^2}{4\pi e^2 n_{\rm e}\epsilon_{\rm e}} \sim 1$ for the energy equipartition between magnetic fields and particles. So, one expects $\frac{\lambda_{\rm B}}{\lambda_{\rm ph}} > 1$ and the jitter radiation seems to be less feasible. On the other hand, if large scale turbulence is presented, synchrotron spectra are deformed near the cut-off energy. Bykov et al. (2012) demonstrated that such fluctuations of the magnetic field shift the cut-off to the higher energies.

Chapter 3

Physical Implications of the Gamma-ray Emission beyond 100 TeV Observed in the Crab Nebula

Recently the gamma-ray emission beyond 100 TeV was reported with Tibet Air Show Gamma Experiment and High Altitude Water Cherenkov Gamma-Ray Observatory. Observed spectrum is smoothly connected to the previous TeV gamma-ray spectra (below 100 TeV) and the consistency between the past observations and new observations makes $\sim$ 100 TeV gamma-ray results more reliable. The smooth connection of the gamma rays suggests the same electron distribution produces the gamma-ray emission above 100 TeV. According to the current pulsar wind nebula model, the gamma-ray above $\sim$ 1 GeV is produced via inverse Compton scattering from non-thermal electrons accelerated at the termination shock. We can investigate the environment nearby the acceleration site based on the highenergy electrons responsible for 100 TeV gamma ray because of the rapid radiation cooling time. In addition, the extension of gamma-ray spectrum allows one to predict a possibility of the detection by future measurements (e.g. Large High Altitude Air Shower Observatory) from PeV electrons. In this chapter, we discuss a constraint on the strength of the magnetic field based on the simple one-zone model and an implication of two-zone model. Most of the contents in this chapter are taken from Khangulyan et al. (2020).

3.1 Non-thermal Steady Emission from the Crab Nebula

The non-thermal emission from the Crab Nebula covers an unprecedented energy range, including high-energy and very-high-energy (VHE, > 100GeV) gamma rays (see Hester, 2008, and references therein), and demonstrates complex energy-dependent morphology (Weisskopf et al., 2000; Madsen et al., 2015; Yeung and Horns, 2019; H. E. S. S. Collaboration et al., 2019a). Presently, the magnetohydrodynamic (MHD) description provides the most fruitful approach for studying the properties

of pulsar wind nebulae (PWNe) (Kennel and Coroniti, 1984a; Bogovalov and Khangoulian, 2002b; Komissarov and Lyubarsky, 2004; Bogovalov et al., 2005; Volpi et al., 2008; Camus et al., 2009; Bucciantini, 2014; Porth et al., 2014; Barkov et al., 2019). In this framework, one assumes that the central pulsar ejects an ultrarelativistic wind that interacts with the surrounding medium (Rees and Gunn, 1974; Kennel and Coroniti, 1984b). The bright non-thermal nebula corresponds to the shocked pulsar wind. Relativistic electrons are presumably accelerated at the pulsar wind termination shock and interact with the background fields while being advected in the down-stream region. Their synchrotron emission, which is generated at the interaction with the nebular magnetic field, dominates in the range from radio to 100 MeV energies; and the emission that is registered at GeV energies and above is produced by inverse Compton (IC) scattering of background and synchrotron photons (see, e.g., Aharonian and Atoyan, 1998).

The size of the Crab Nebula depends on photon energy, which is most likely caused by the different cooling times of the parent electrons. If one assumes that the emitting particles are injected at the pulsar wind termination shock and get advected with the down-stream flow, then one can reproduce the extension of the Crab Nebula seen in UV, X-ray, and TeV energy bands reasonably well (Madsen et al., 2015; H. E. S. S. Collaboration et al., 2019a). This suggests that the termination shock plays an important (or even the major) role in the acceleration of non-thermal particles. There are however certain caveats in this conclusion. First of all, the termination shock is expected to have a complex non-spherical shape (Bogovalov and Khangoulyan, 2002; Lyubarsky, 2002b). Thus, the physical conditions should vary considerably depending on the specific region of the pulsar wind termination shock. Only very accurate simulations together with detailed observations may hypothetically localize presumably the most important region with particle acceleration (Olmi et al., 2015). The particle acceleration sites localized with X-ray observations are responsible for acceleration of TeV electrons and this does not exclude possible existence of other acceleration sites, especially those contributing to other energy ranges. For example, modeling of the radio morphology does not allow one to define the origin of the radio-emitting electrons (i.e., with energy of ~ 100 GeV) in the Crab Nebula (Olmi et al., 2014). On the other hand, detection of intense flares in the GeV band implies efficient acceleration of PeV electrons in environments characterized by a very strong magnetic field, in excess of 1 mG (Buehler et al., 2012; Bühler and Blandford, 2014). Such a strong magnetic field is inconsistent with the pulsar wind termination shock, except maybe in the region close to the pulsar rotation axis (Porth et al., 2014).

There are little doubts that magnetic fields are essential for particle acceleration. However, the magnetic field at the accelerator also makes particles to loose energy due to synchrotron cooling. Thus, particle acceleration unavoidably competes with energy losses, and the maximum attainable energy for non-thermal particles does not generally determines the efficiency of the acceleration process (Aharonian et al., 2002). If synchrotron losses are the dominant cooling mechanism, which is almost unavoidable for the acceleration of extremely energetic electrons, then the product of the maximum attainable energy and the square root of the magnetic field strength, $E_{\rm max}B^{1/2}$, can be taken as a measure

of the accelerator efficiency.

If the acceleration and the emission regions are characterized by the same strength of the magnetic field, then the cut-off energy of the synchrotron component provides a good probe for the acceleration efficiency. In the case of PWNe, MHD simulations suggest that regions with very different strength of the magnetic field co-exist inside the nebula, so non-thermal spectra have a limited ability to constrain the physical conditions at the acceleration site. For the conditions expected in PWNe, only the emission from ultra-high-energy (UHE, > 100 TeV) particles, which have cooling times short enough, may probe the physicals conditions in the accelerator. The synchrotron emission generated by these particles appear at the energies above 100 keV and the modern instruments have a limited ability to probe this energy band. In particular, the information obtained with *Fermi* Large Area Telescope (*Fermi*-LAT) allows one to probe the above-cut-off part of the synchrotron spectrum, the emerging part of the IC component, and the GeV flares. While the flares are most-likely produced in some specific sites in the nebula, the shape of the cut-off part of the spectrum does not allow one to robustly constrain the conditions in the accelerator as it requires a very precise mathematical description of the acceleration mechanism (see, however, Zirakashvili and Aharonian, 2007, for a consideration of acceleration in non-relativistic regime).

Recently it was reported the detection of the Crab Nebula in the UHE regime with *Tibet ASγ* and High Altitude Water Cherenkov Gamma-Ray Observatory (*HAWC*) (Amenomori et al., 2019; Abeysekara et al., 2019). These measurements extend considerably the nebula spectrum, which was previously measured upto 80 TeV with High Energy Gamma Ray Astronomy (HEGRA) (Aharonian et al., 2004). The emission reported by *Tibet ASγ* and *HAWC* collaborations is predominately generated on the Cosmic Microwave Background Radiation (CMBR), and it allows modelling which is free from several additional assumptions, in particular on the intensity and distribution of the synchrotron target. As the reported spectrum smoothly connects to the well-established part of the spectrum, 100 GeV – 50 TeV, it seems to be feasible that UHE and VHE photons registered with *Tibet ASγ*, *HAWC* and HEGRA are produced by particles that originate at the same acceleration site. Thus study of the UHE gamma ray should allows one to constrain accurately the physical conditions at the site responsible for the acceleration of the major fraction of VHE particles in the Crab Nebula.

3.2 Ultra-High-Energy (UHE) Particles in the Crab Nebula

While high-energy particles in PWNe predominately lose their energy due to synchrotron, IC, and adiabatic losses, in the UHE domain synchrotron losses are expected to dominate. Thus, the particle cooling time can be estimated as:

$$t_{\rm SYN} \simeq 4 \times 10^5 \left(\frac{E}{1\ \rm PeV}\right)^{-1} \left(\frac{B}{1\ \rm mG}\right)^{-2}\ \rm s\,, \tag{3.1}$$

where E and B are the electron energy and magnetic field strength, respectively. The advection distance

$$l_{\rm SYN} = t_{\rm SYN} V_{\rm f} \simeq 4 \times 10^{-3} \left(\frac{E}{1\ {\rm PeV}}\right)^{-1} \left(\frac{B}{1\ {\rm mG}}\right)^{-2} V_{\rm f}\ {\rm pc}\,. \tag{3.2}$$

where $V_{\rm f}$ is flow velocity in the units of the speed of light. In PWNe, the down-stream magnetic field may considerably change on scales comparable to the termination shock radius, $R_{\rm TS}$, (see, e.g., Kennel and Coroniti, 1984a), which allows one to define a dimensionless advection distance:

$$\lambda_{\rm SYN} = \frac{l_{\rm SYN}}{R_{\rm TS}} = 10^{-2} \left(\frac{V_{\rm f}}{0.3}\right) \left(\frac{R_{\rm TS}}{0.1\ {\rm pc}}\right) \left(\frac{E}{1\ {\rm PeV}}\right)^{-1}\,. \tag{3.3}$$

The above estimate suggests that the emission of UHE > 100 TeV electrons indeed provides a good probe for the physical conditions in the acceleration region.

3.2.1 Radiation from the UHE Particles

The typical synchrotron photon energy of UHE electrons can be written in the Eq. (3.4):

$$\varepsilon_{\rm SYN} \simeq 60 \left(\frac{E}{1\ {\rm PeV}}\right)^{2} \left(\frac{B}{1\ {\rm mG}}\right)\ {\rm MeV}\,. \tag{3.4}$$

Therefore, the synchrotron emission of UHE electrons appears in the gamma-ray energy band, which can be probed by spaceborn instruments sensitive for > 100 keV emission (given $B \geq 100$ μG and $E \geq 0.1$ PeV). This band on one hand has quite a limited coverage and there is no robust detection of any features that may help to disentangle the influence of the magnetic field strength and parent particle energy. Thus, the observational information solely contained in the synchrotron emission does not allow one to constrain the parameters in the emitting region.

On the other hand, several different photon fields may provide an important target for the IC emission generated in the Crab Nebula (Atoyan and Aharonian, 1996; Aharonian and Atoyan, 1998). Three dominant IC components are generated on far-infrared (FIR), CMBR, and synchrotron photons. Up-scattering of synchrotron photons through the synchrotron-self-Compton (SSC) channel provides the major contribution at TeV energies. The synchrotron target is however characterized by a relatively high photon energy, and the SSC process is significantly attenuated for UHE electrons due to the Klein – Nishina (KN) effect. The KN reduction of the IC cross-section occurs if electrons up-scatter photons with an energy, $\varepsilon_{\rm s}$, exceeding the limiting value:

$$\varepsilon_{\rm s} \geq \varepsilon_{\rm kn} = 3 \times 10^{-4} \left(\frac{E}{1\ {\rm PeV}}\right)^{-1}\ {\rm eV}\,. \tag{3.5}$$

The flux from the Crab Nebula at these energies is about 10^{-10} erg s^{-1} cm^{-2}. For the nebula radius of $R_{\rm n} \simeq 1$ pc, the energy density of the synchrotron target, which is up-scattered in the Thomson regime, is $\sim 10^{-2}$ eV cm^{-3}. This value falls significantly below the energy density of the Galactic background photon fields.

If the target is a diluted Plankian photon field, then the limit by Eq. (3.5) corresponds to a temperature of 10 K. This implies that all background fields, except the CMBR, are up-scattered deep in the KN regime. Thus, one expects that the emission detected with *Tibet ASγ* and *HAWC* in the UHE regime is predominately generated on CMBR photons. This conclusion is consistent with numerical calculations shown in Figure 3.1. The spectral calculations shown in this figure were performed with the package `naima` (Zabalza, 2015). An analytic approximation suggested in Aharonian et al. (2010) was used for computing the synchrotron emission; the SSC spectrum was obtained by integrating the scattering-angle averaged cross-section (Aharonian and Atoyan, 1981); and the IC spectra generated on the Galactic background fields were calculated with an analytic approximation by Khangulyan et al. (2014). We adopted a one-zone approximation, which assumes a spatially homogeneous model, and the electron distribution was assumed to be a broken power-law with an exponential cutoff:

$$\frac{dN}{dE} = A \exp\left(-\left(\frac{E}{E_{\rm cut}}\right)^2\right) \times \begin{cases} \left(\dfrac{E}{1\ \mathrm{TeV}}\right)^{-\alpha_1} & \text{if} \quad E < E_{\rm br} \\ \left(\dfrac{E_{\rm br}}{1\ \mathrm{TeV}}\right)^{\alpha_2-\alpha_1} \left(\dfrac{E}{1\ \mathrm{TeV}}\right)^{-\alpha_1} & \text{if} \quad E > E_{\rm br} \end{cases} . \tag{3.6}$$

Here E is electron energy, A is an electron spectrum normalization constant, $E_{\rm cut}$ is cutoff energy, and $E_{\rm br}$ is power-law break energy. We adopted the following parameters[*1]: $E_{\rm cut} = 1.863$ PeV, $E_{\rm br} = 0.265$ TeV, $\alpha_1 = 1.5$, $\alpha_2 = 3.233$ and $B = 125$ μG (see also Meyer et al., 2010).

The IC spectra generated by four different photon fields, i.e., CMBR, FIR (a graybody distribution with temperature $T_{\rm fir} = 70$ K and energy density $U_{\rm fir} = 0.5$ eV cm^{-3}), near-infrared (NIR) ($kT_{\rm nir} = 5000$ K, $U_{\rm nir} = 1$ eV cm^{-3}), and synchrotron photons, are shown together with their summation in Figure 3.1. We assumed that the synchrotron target is homogeneously generated in the nebula, and the volume averaged density of the SSC target is enhanced by a factor of 2.24 as compared to the boundary region of the nebula (see Atoyan and Aharonian, 1996, for details).

Since the UHE gamma rays are predominantly generated by CMBR IC, the properties of the target are firmly defined and one can robustly define the spectrum of the emitting particles. Using the approximate formulae suggested by Khangulyan et al. (2014), one can conclude that to generate the highest energy part of the spectrum reported by *Tibet ASγ*, $\varepsilon \simeq 300$ TeV, electrons with energy up to 0.8 PeV are required. The corresponding numerical calculations are shown in Figure 3.2. This figure shows that the *Tibet ASγ* measurements constrain the particles in the range 50 – 750 TeV, in a parameter-free way. The calculation of the synchrotron emission from these particles requires additional assumptions on the strength and possible distribution of the magnetic field. In order to constrain on the parameters, quality of the $\gtrsim$ 50 TeV gamma-ray data becomes important because the dominant the seed photon field changes from SSC to CMBR. The previous most highest gamma-ray data point was measured

[*1] These parameters are suggested in the `naima` documentation at https://naima.readthedocs.io/en/latest/radiative.html

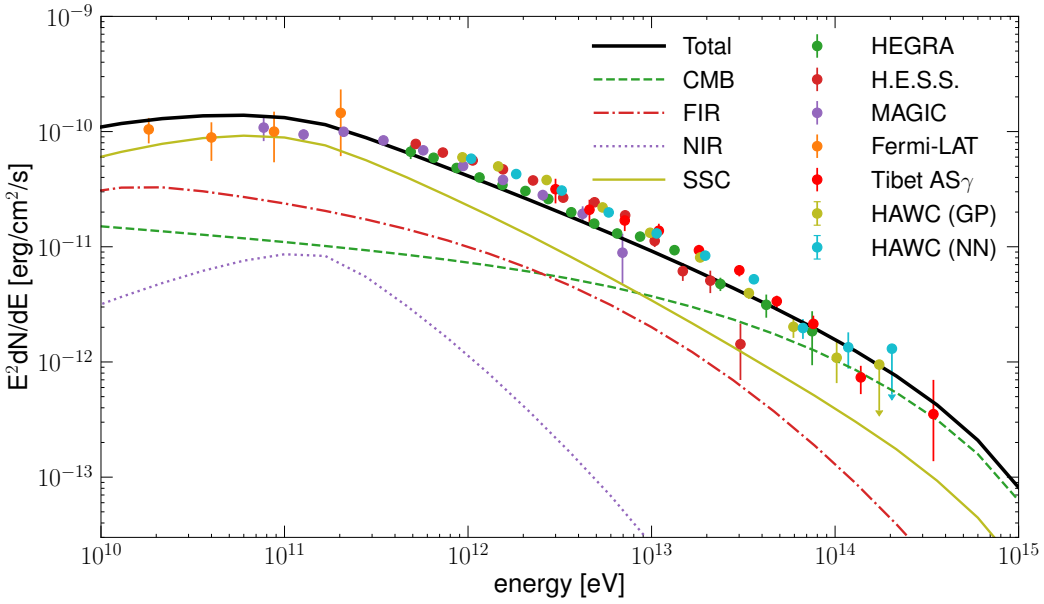

Figure 3.1 Gamma-ray spectrum of the Crab Nebula. The gamma-ray data are taken from *Fermi*-LAT (Buehler et al., 2012), HEGRA (Aharonian et al., 2004), H.E.S.S. (Aharonian et al., 2006), MAGIC (Albert et al., 2008), *Tibet ASγ* (Amenomori et al., 2019), *HAWC* (Abeysekara et al., 2019). IC spectra produced on four different photon fields: SSC (solid line), CMBR (dashed line), FIR (dash-dotted line), and NIR (dotted line) are shown together with their summation (thick solid line).

upto 80 TeV with HEGRA (Aharonian et al., 2004). HEGRA is a relatively old instrument and the reliability is somehow doubtful. The recent measurements with *Tibet ASγ* and *HAWC* are consistent with HEGRA data points, therefore the $\gtrsim$ 50 TeV gamma-ray results become much reliable. Note that we can see a discrepancy between the one-zone model and the observed spectrum from ∼1 GeV to ∼100 GeV in Figure 3.2. This gap originates from the simplification of the one-zone model[*2]. However, this discrepancy does not affect the obtained parameters in the following, because the energy range of the parent electrons responsible for $\lesssim$ 100 GeV gamma rays is significantly lower than the UHE gamma rays.

The obtained the strength of the magnetic field $B = 125$ μG is based on the global one-zone modelling. Figure 3.3, we show the synchrotron emission from 50 − 750 TeV electrons for three different strengths of the magnetic field as obtained in the framework of a one-zone model (all the remaining model assumptions are the same as in Figure 3.2). One can see that the synchrotron emission of ∼ 300 TeV electrons (derived model-independently from the *Tibet ASγ* measurements), violates the

[*2]If the particle transport with radiative cooling and adiabatic loss based on the MHD-flow model is considered, this discrepancy can be solved (e.g. H. E. S. S. Collaboration et al., 2019a).

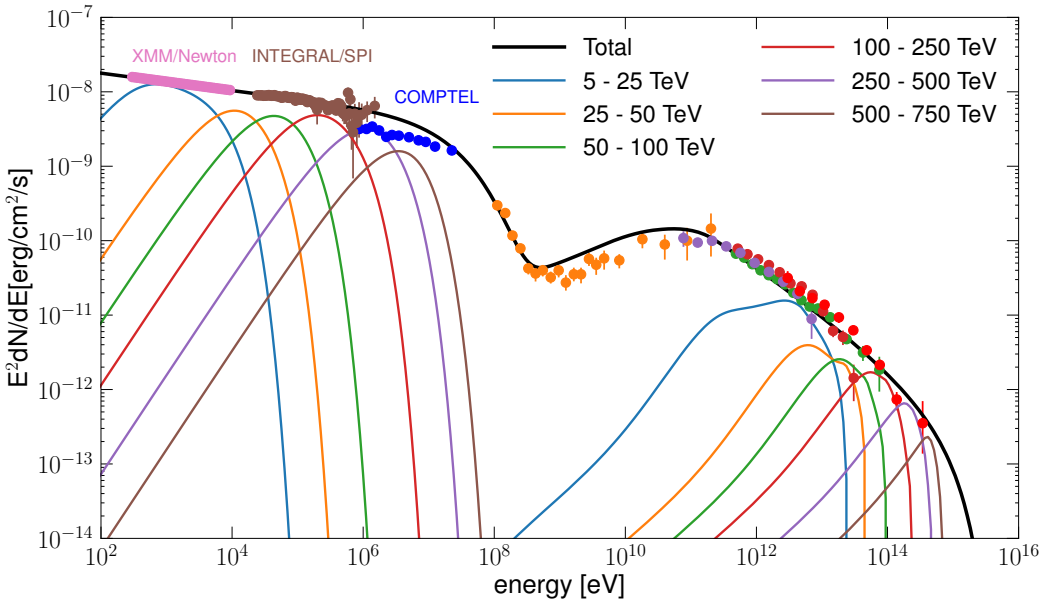

Figure 3.2 Synthetic non-thermal emission computed with a one-zone model (thick solid line). Synchrotron and IC emission by electrons from several energy ranges, 5 – 25 TeV, 25 – 50 TeV, 50 – 100 TeV, 100 – 250 TeV, 250 – 500 TeV, 500 – 750 TeV, are shown with thin solid lines. The magnetic field was assumed to have a strength of $B = 125\,\mu$G. In addition to the gamma-ray data shown in Figure 3.1, the following X-ray and soft gamma-ray measurements are shown *XMM-Newton* (Kirsch et al., 2005), *INTEGRAL*/SPI (Jourdain and Roques, 2009), and *COMPTEL* (Kuiper et al., 2001).

flux level in the MeV band measured with INTErnational Gamma-Ray Astrophysics Laboratory and Imaging Compton Telescope (*COMPTEL*), unless $B \lesssim 125\,\mu$G.

To illustrate that these data indeed constraint the strength of the magnetic field with very high accuracy, we try to derive a magnetic field using *INTEGRAL*/SPI fluxes and > 10 TeV gamma-ray fluxes (with energy above 10 TeV that include the HEGRA , H.E.S.S. and *Tibet ASγ* measurements), which more appropriately represents the field in the acceleration site [*3]. The computation of the spectral energy distribution (SED) models and subsequent fit to the multi-wave-length spectra are performed using the `naima` Python package (Zabalza, 2015). `naima` allows one to obtain the best-fit values and posterior probability distributions of the model parameters given the SED points from the χ^2, calculated assuming that the SED point uncertainties are Gaussian and uncorrelated. The model parameters are scanned using the Markov Chain Monte Carlo (MCMC) method, as implemented in the `emcee`

[*3]Electrons responsible for 100 TeV IC emission mostly produce synchrotron radiation visible with *INTEGRAL*/SPI and partially at the *COMPTEL* bands. Since a larg part of the *COMPTEL* data points are measured at significantly higher energies, they cannot be reproduced by the radiation model. Therefore we only use only *INTEGRAL*/SPI data points.

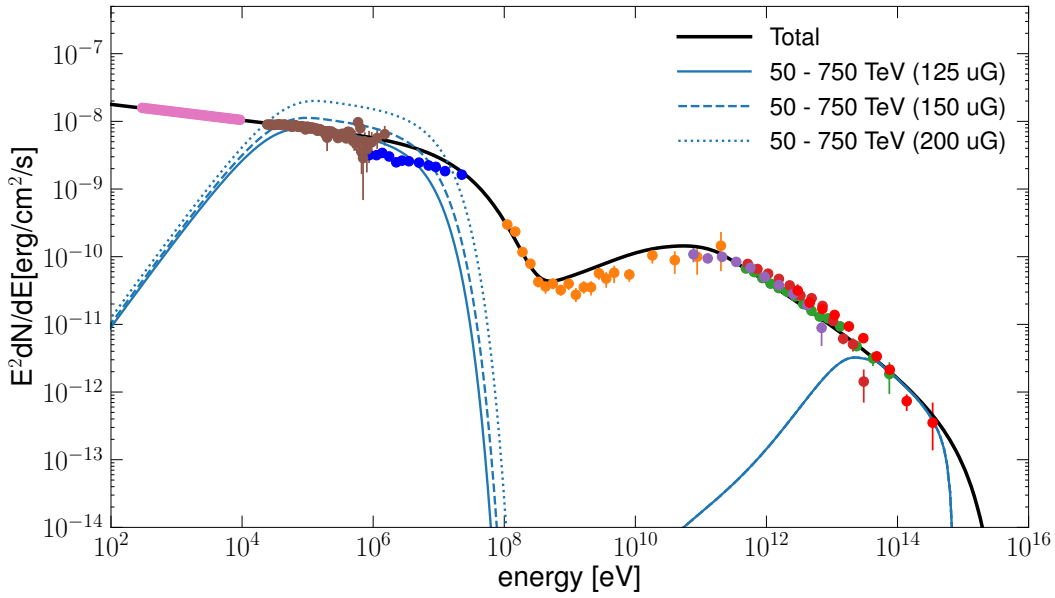

Figure 3.3 Computed synchrotron emission from electrons with energy in the range from 50 to 750 TeV for three different magnetic field strengths, $B = 125$ (thin solid line), 150 (dashed line), and 200 μG (dotted line). The electron energy distribution was kept unchanged to satisfy the *Tibet ASγ* measurements. The synthetic non-thermal spectrum is shown with thick solid line. For the origin of the shown data points see Figures. 3.1 and 3.2.

package (Foreman-Mackey et al., 2013). For all model parameters we assume a flat prior probability distribution, within physical constraints on the parameters values (e.g., particle densities are positive). We scan the normalization A and the cutoff energy $E_{\rm cut}$ in logarithmic space, so that the fit parameter is actually $\log_{10}(A/{\rm eV}^{-1})$ and $\log_{10}(E_{\rm cut}/1\,{\rm TeV})$, respectively. The energy distribution of emitting particles is assumed to be a power-law with exponential cutoff:

$$[E]N = A\left(\frac{E}{1\,{\rm TeV}}\right)^{-\alpha}\exp\left[-\left(\frac{E}{E_{\rm cut}}\right)^{\beta}\right], \tag{3.7}$$

where E is electron energy. The particle spectrum is determined by four parameters: A is normalization; $E_{\rm cut}$ is cutoff energy; α is the spectral index of a power-law distribution; and β is the cutoff index. The obtained parameters are shown in Table 3.1. In addition, we provide the results of the probability density distributions of the model parameters in Figure A.1. The MCMC simulations require the magnetic field strength to be in the range $B = 118^{+3}_{-2}$ μG, which is consistent with a less sophisticated estimate shown in Figure 3.3.

The obtained limit does not concern the acceleration of PeV electrons. The IC emission of PeV electrons should appear in the spectrum above 400 TeV. Currently, no measurements are available in this energy band. However, it is expected that Large High Altitude Air Shower Observatory (*LHAASO*), a

Table 3.1 Results of fitting of the hard X-ray and multi-TeV spectra of the Crab Nebula with `naima`.

parameter	value
magnetic field	$B = 118^{+3}_{-2}\,\mu\mathrm{G}$
normalization	$A = 1.0^{+0.2}_{-0.1} \times 10^{35}\,\mathrm{eV}^{-1}$
power-law index	$\alpha = 2.88 \pm 0.04$
cutoff energy	$E_{\mathrm{cut}} = 330 \pm 20\,\mathrm{TeV}$
cutoff index	$\beta = 1.6 \pm 0.2$

new powerful cosmic ray facility, will soon probe the gamma-ray spectrum of the Crab Nebula in this energy interval (see He, 2019, and references therein). Remarkably, the attenuation of such energetic photons from the Crab Nebula due to the interactions with diffuse galactic radiation fields is expected to be not significant (Vernetto and Lipari, 2016).

3.2.2 The Possibility of the Electron Acceleration upto PeV at the Termination Shock

One-zone modelling requires weak magnetic field at the acceleration site, $B = 125\ \mu\mathrm{G}$[*4]. In order to explain the ~ 100 MeV gamma-ray emission via the synchrotron channel, the electron cut-off energy should reach several PeV based on the MHD flow model (Atoyan and Aharonian, 1996; Meyer et al., 2010). A similar cut-off energy is obtained by the one-zone modelling, $E_{\mathrm{cut}} \simeq 1.8$ PeV with the strength of the magnetic field $B = 125\ \mu\mathrm{G}$. However, if the magnetic field has a statistical characteristics which is described by the probability density function (PDF), the cut-off shape of the synchrotron spectra-shape may be strongly affected. As the result, the synchrotron spectrum can extend to higher energy range than the simple exponential cutoff. Here, we tried two types of the PDF: (i) exponential type (Zirakashvili and Ptuskin, 2008) and (ii) gaussian type (Bykov et al., 2012; Derishev and Aharonian, 2019). The PDF is discribed as follows:

$$\mathrm{PDF}_{\mathrm{exp}} = \frac{6B}{B_0^2} \exp\left(-\frac{\sqrt{6}B}{B_0}\right), \tag{3.8}$$

$$\mathrm{PDF}_{\mathrm{gauss}} = \left(\frac{6}{\pi}\right)^{1/2} \frac{3B^2}{B_0^3} \exp\left(-\frac{3B^2}{2B_0^2}\right). \tag{3.9}$$

Here B_0 represents the square root of the mean square of the random magnetic field:

$$\left\langle B^2 \right\rangle = \int_0^\infty B^2 \mathrm{PDF}_{\mathrm{exp/gauss}} \mathrm{d}B = B_0^2\,. \tag{3.10}$$

[*4] We do not account for relative flux uncertainties between different instruments, thus the strength of the magnetic filed, $B = 125\ \mu\mathrm{G}$, is indistinguishable from the reveled by the MCMC simulation result, $B = 118\ \mu\mathrm{G}$.

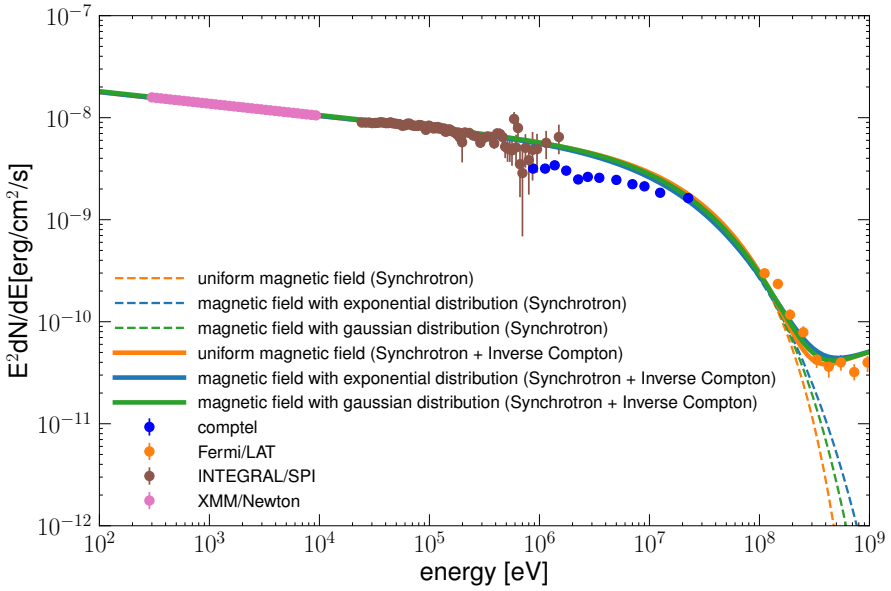

Figure 3.4 Synchrotron spectrum of the uniform magnetic (dashed orange line), the exponential distributed magnetic field (dashed blue line), and the gaussian distributed magnetic field (dashed green line). The solid line represents the synthetic non-thermal radiation spectra.

In the case of Eq. (3.8) and (3.9), the analytical form of the synchrotron spectrum of a single electron was found by Zirakashvili and Aharonian (2010) for the exponential type and Derishev and Aharonian (2019) for the gaussian type:

$$R_{\rm exp}(\omega/\omega_c) = 1.50(\omega/\omega_c)^{1/3}(1 + 1.53(\omega/\omega_c)^{1/2})^{11/6} \exp\left(-96^{1/4}(\omega/\omega_c)^{1/2}\right), \tag{3.11}$$

$$R_{\rm gauss}(\omega/\omega_0) = \frac{\alpha}{3}\frac{(m_e c^2)^2}{E^2}\left(1 + (\omega/\omega_0)^{2/3}\right)\exp\left(-2(\omega/\omega_0)^{2/3}\right), \tag{3.12}$$

where α is fine structure constant and ω_c and ω_0 are defined as follows:

$$\omega_c \equiv \frac{3E^2 eB_0}{2m_e^3 c^5},$$
$$\omega_0 \equiv \frac{8}{9}\omega_c .$$

Here, E, e, m_e, and c represent electron energy, the elementary charge, the electron mass, and the speed of light.

The calculated synchrotron spectrum is shown in Figure 3.4. We assumed the electron energy distribution to be a broken power-law with exponential cutoff and the obtained cutoff energy is $E_{\rm cut,uni} = 1.9$ PeV, $E_{\rm cut,exp} = 1.4$ PeV, and $E_{\rm cut,gauss} = 1.6$ PeV for the uniform magnetic field, the exponential distributed

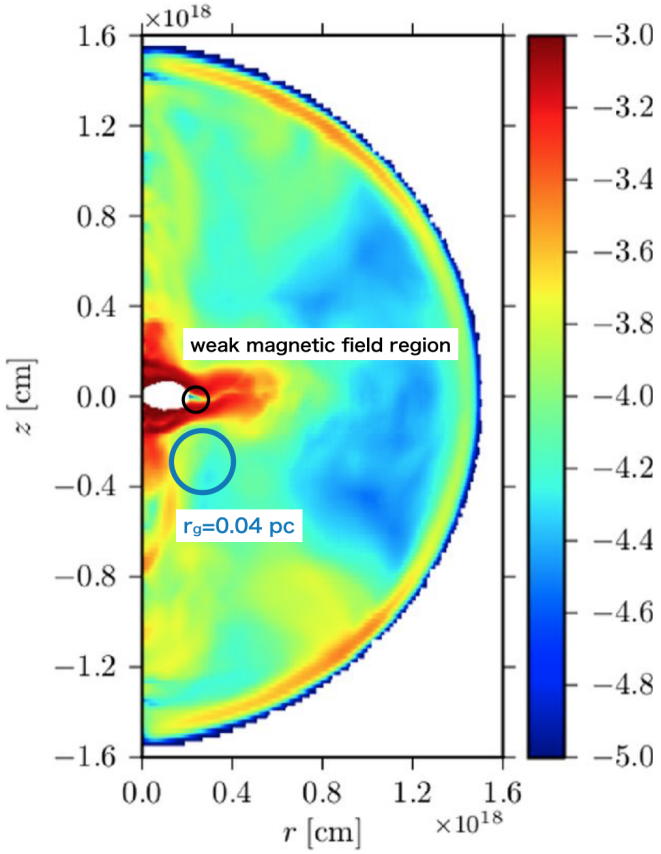

Figure 3.5 The angular averaged magnetic field strength in log scale. The black circle indicates a weak magnetic field region. The blue circle represents the gyro radius of 4 PeV electrons in 100 μG. The figure is taken from Porth et al. (2014) with modifications.

magnetic field, and the gaussian distributed magnetic field, respectively. Therefore the required cut-off energy is still above PeV, even if we consider a stochastic magnetic field configuration which can extend the tail toward high energy.

In the standard MHD paradigm, the particle acceleration occurs at the termination shock. However, this hypothesis seems to be inconsistent for multi PeV electrons, which are required to explain the flux of 100 MeV gamma rays. From Eq. (3.4), one can obtain the electron energy emitting 100 MeV gamma-ray synchrotron, $E \simeq 4$ PeV. The gyro radius of such electrons is:

$$r_{\rm g} = 0.04 \left(\frac{E}{4\ {\rm PeV}}\right)\left(\frac{B}{100\ \mu{\rm G}}\right)^{-1}\ {\rm pc} \simeq 0.4 R_{\rm TS}\,. \tag{3.13}$$

Recent 3D MHD simulation indicates that 100 μG magnetic field is expected in a tiny region near the termination shock, (see the black circle in Figure 3.5) (Porth et al., 2014). If we assumed a weak magnetic field $B =$ 100 μG, the gyro radius of the PeV electron is about 40 % of the termination shock.

Figure 3.5 suggests the gyro radius becomes larger than the weak magnetic region, which means the difficulty to confine the multi PeV electrons in this region. In addition, the larger gyro radius indicates the plane shock approximation does not hold and the acceleration efficiency should decrease. These imply the electrons which are responsible for the 100 MeV gamma ray can hardly be produced at the weak magnetic field region. The one solution is the electrons responsible for the synchrotron gamma-ray emission originated from the different population from the X-ray emitting electrons, i.e. two-zone model.

3.2.3 Two-zone Modelling

The synchrotron spectrum of the Crab Nebula extends to energies beyond 100 MeV and requires electrons with energy up to several PeV. This emission component is conventionally associated with the electrons accelerated at the termination shock, however the gamma-ray spectrum in the 1 to 100 MeV band is not smooth. It shows a structure which can be better reproduced by two different populations of UHE electrons described by power-law distribution with an exponential cut-off ($E_{\rm cut}$ = 500 TeV) and by relativistic Maxwellian-like distribution (Aharonian and Atoyan, 1998). The relativistic Maxwellian-like distribution is written by

$$\frac{\mathrm{d}N}{\mathrm{d}E} = A_2 E^2 \exp\left(-\frac{E}{E_{\rm T}}\right), \tag{3.14}$$

where A_2 and $E_{\rm T}$ represent a normalization factor and a temperature parameter. We note that a Maxwell distribution does not indicate the thermal equilibrium, but just a very hard acceleration spectrum. The superposition of emission of these two components is demonstrated in Figure 3.6. These two electron populations could be accelerated in different regions through different acceleration processes. For example, Sironi and Spitkovsky (2014) have shown that a hard distribution of non-thermal particle can be formed by magnetic reconnection in highly magnetized environments. Lyutikov et al. (2018b) suggested that an electron component accelerated by magnetic field reconnection operating in the bulk of the nebula (see, e.g., Komissarov, 2013) might be responsible for the dominant radio and soft gamma-ray emission detected from the Crab Nebula. Magnetic reconnection is considered as a feasible mechanism to power the Crab flares (Cerutti et al., 2012, 2013; Lyutikov et al., 2018a), thus the particles producing the steady MeV and flaring GeV synchrotron emission may have a common origin (see the discussion in Lyutikov et al., 2018b). We show in Figure 3.6 synthetic spectra computed for three different strengths of the magnetic field in region where the Maxwellian-like distribution is localized: B_2 = 125, 500, and 1000 μG. As it can be seen by a suitable choice of the temperature parameter ($E_{\rm T}$ = 260, 130, and 90 TeV, respectively), one can get identical synchrotron spectra. In contrast, the IC spectra show important differences (see Figure 3.6).

First of all, if the MeV spectral feature is real, one should expect a significantly smaller flux at 300 TeV. The expected difference is comparable with the *Tibet ASγ* error, so presently we cannot make

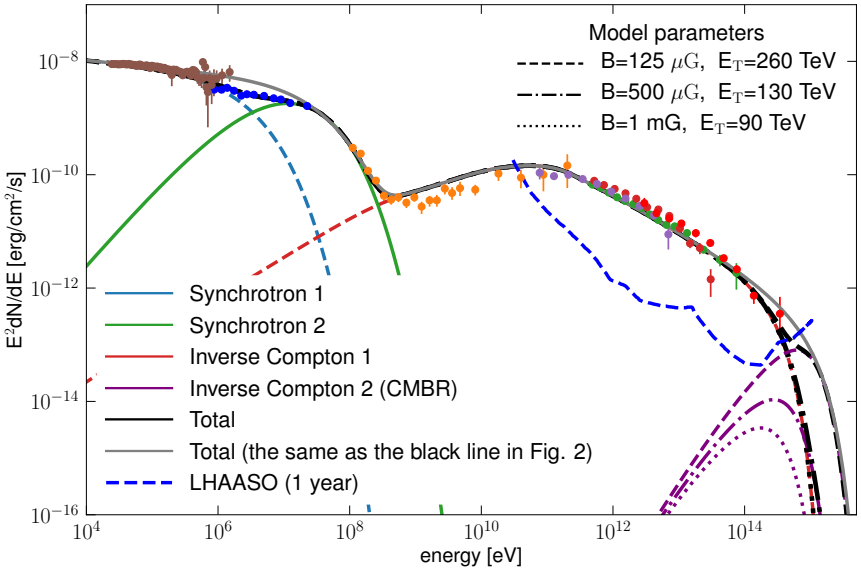

Figure 3.6 Computed synchrotron and IC emission components produced by two populations of electrons: a power-law with exponential cut-off energy distribution in B = 125 μG magnetic field, and a relativistic Maxwellian in B = 125, 500, and 1000 μG fields. For the origin of the shown data points see Figures 3.1 and 3.2.

any quantitative statement. However, the future measurements *LHAASO* should allow distinguishing between these two cases (shown with black and gray lines in Figure 3.6). To illustrate that, we show in Figure 3.6 the *LHAASO* sensitivity expected for one-year exposure(Bai et al., 2019). We also note that important new information can be obtained, as well, in the MeV energy band, e.g., with Gamma-Ray and AntiMatter Survey (Aramaki et al., 2020) or e-ASTROGAM (de Angelis et al., 2018). If these observations will confirm the two-component composition of the Crab Nebula spectrum, then one can attempt to define the magnetic field strength in the "Maxwellian region". Although from Figure 3.6 it may look as the *LHAASO* sensitivity is not good enough for such measurements, we remind that the shown sensitivity corresponds to one-year exposure. If the instrument will operate long enough, e.g. ten years, its performance may appear to be sufficient for obtaining a meaningful constraint on the magnetic field strength in this hypothetical "Maxwellian region."

3.3 On the Magnetization of the Pulsar Wind

The MHD framework provides important insights into non-thermal physical processes in PWNe. In particular, this concerns the dynamics of the magnetic field, particle transport and their radiation. Although the simplest 1D analytic models helped to advance the studies of PWNe, the most realistic

results are achieved with numerical 3D MHD simulations (see, e.g., Porth et al., 2014; Barkov et al., 2019).

The MHD models have limitations among which the phenomenological treatment of particle acceleration is essential. Although it is proved that relativistic outflows on different astrophysical scales are characterized by particle acceleration and radiation, PWNe demonstrate unprecedentedly high efficiency of non-thermal processes. Despite the systematic study of PWNe, it is still not fully understood what makes of PWNe so efficient high-energy sources.

One of the key parameters in MHD models applied to PWNe is the magnetization of the pulsar wind, σ, which determines the fraction of the pulsar spindown losses that carried by the Poynting flux. This parameter determines the magnetic field at the pulsar wind termination shock. The downstream magnetic field at the termination shock is

$$B \simeq h(\sigma)\sqrt{\frac{L_{\rm sd}}{cR_{\rm TS}^2}} \simeq 400h(\sigma)\left(\frac{R_{\rm TS}}{0.1\ {\rm pc}}\right)^{-1}\ \mu{\rm G}\,, \tag{3.15}$$

where the function h accounts for the the Rankie-Hugoniot conditions at the termination shock and the strength of the magnetic field in the unshocked pulsar wind: $h \simeq 1$ for $1 > \sigma \geq 0.1$, and $h(\sigma) \simeq 3\sigma^{1/2}$ for $\sigma < 0.1$. In the case of the Crab Nebula, the radius of the termination shock is constrained robustly, $R_{\rm TS} \lesssim 0.1\,{\rm pc}$, with the observations in the X-ray band (Weisskopf et al., 2000), the magnetic field at the termination shock should exceed 100 μG, unless the wind magnetization is very small, $\sigma \leq 10^{-2}$, or magnetic field dissipates at the termination shock (Lyubarsky, 2003; Sironi and Spitkovsky, 2011).

As shown in Figure 3.3, the strength of the magnetic field in the region responsible for acceleration of the "wind electrons" should not exceed 125 μG. Eq. (3.15) shows that such a modest magnetic field requires very weak magnetization of the pulsar wind, $\sigma \leq 10^{-2}$. Although 1D MHD models of the Crab Nebula, does require such a weakly magnetized pulsar wind, currently, it is considered as an artefact of the ideal 1D approximation. Indeed, the rigid flow structure implemented in ideal 1D models results in a rapid increase of the magnetic field in the shocked pulsar wind. The initially weak magnetic field in the flow approaches the equipartition strength on the scale of several termination shock distances. For the magnetization of $\sigma = 3 \times 10^{-3}$, simple 1D models can reproduce the radiation spectrum (Kennel and Coroniti, 1984a), expansion rate, and, to some extent, also the X-ray morphology band (Bogovalov and Khangoulyan, 2002).

3D MHD models agree better with the features of the Crab Nebula if one adopts a higher wind magnetization. As revealed by numerical simulations, the initially strong magnetic field can dissipate significantly in the shocked pulsar wind, allowing MHD solutions with highly magnetized pulsar winds, $\sigma \sim 0.5$. However, such a strong magnetization implies strong magnetic field at the termination shock, $B \simeq 400\,\mu{\rm G}$. The estimate based on Eq. (3.15) is consistent with 3D numerical simulations by Porth et al. (2014). If UHE electrons were accelerated in a region with such a strong magnetic field, their synchrotron emission would violate the level of the MeV flux. In Figure 3.5 or Figure. 11

(right panel) of Porth et al. (2014), one can see a small region close in the equator plane characterized by a relatively weak magnetic field. Actually, the equatorial region has been suggested as the most plausible site for the acceleration of TeV electrons in the Crab Nebula (Sironi and Spitkovsky, 2011; Olmi et al., 2015), but a highly anisotropic pulsar wind might be required to supply enough energy to this relatively compact region.

3.4 Summary

The energy-dependent morphology seen in the center part of the Crab Nebula suggests that the TeV electrons originate at the pulsar wind termination shock. The IC emission of these VHE electrons smoothly extends to the UHE regime as shown by the recent *Tibet ASγ* measurements. Since UHE electrons predominately interact with CMBR photons, their spectrum and the total energetics is derived model-independently. Because of the short cooling time, these electrons are confined in the proximity of the accelerator. The joint analysis of the fluxes of synchrotron and IC components reveals a weak magnetic field, 118 μG, in the acceleration site responsible for acceleration of multi-hundred TeV electrons in the Crab Nebula. On the other hand, PeV electrons which emit 100 MeV gamma rays seem not to originate from the weak magnetic field region, because the weak magnetic field leads the large gyro radius, 40% of the size of the termination shock. In this case, the plane shock approximation is not held and the acceleration efficiency should be worse. In addition, the larger-gyro radius electrons make difficult to be confined in the small sector where the weak magnetic filed is established (see Figure 3.5).

To obtain such a weak magnetic field at the pulsar wind termination shock, one needs either to assume a small magnetization of the pulsar wind, $\sigma \leq 10^{-2}$ or a highly anisotropic pulsar wind. Either of these possibilities needs to be tested against realistic 3D MHD simulations of the Crab Nebula.

The obtained limitation on the magnetic field might be not valid in the region responsible for acceleration of PeV electrons in the Crab Nebula. The future observations above 1 MeV and 300 TeV will reveal the physical conditions in that region. In particular, these observations have a potential (1) to verify if the broad band spectrum requires a presence of an additional electron component with a narrow energy distribution, and (2) to constrain the magnetic field strength in the region responsible for acceleration of the PeV electrons.

If this future study favors a strong magnetic field in the region of acceleration of PeV electrons, which are responsible for the $\sim$ 100 MeV steady emission in the Crab Nebula, then the site(s) of acceleration of this component could be responsible also for the enhanced GeV emission observed during the Crab flares. Thus, the future observations of UHE gamma rays up to 1 PeV may shed light on the origin of this component, and, perhaps also, its links to the Crab flares. The connection between the $\sim$ 100 MeV steady emission and the Crab flares will be discussed in Chapter 5.

Chapter 4

Gamma-ray Observations with *Fermi* Large Area Telescope

4.1 *Fermi* Gamma-ray Space Telescope

4.1.1 Overview

Fermi Gamma-ray Space Telescope (*Fermi*) was launched on a Delta II Heavy launch vehicle in June 11th, 2008. *Fermi* was put into an orbit at the ~ 565 km altitude and the 25.6 degree inclination angle. *Fermi* is composed of two detectors: the Large Area Telescope (LAT) and Gamma-Ray Burst Monitor (GBM). The LAT, which is a primary detector on board *Fermi*, is a pair production telescope and covers an energy range from 20 MeV to over 300 GeV with a wide filed of view (FoV), 2.4 sr. The GBM provides a spectral and temporal measurement in a energy range 8 keV to 40 MeV, which is a lower range than the LAT. The combination of the LAT and GBM allows to obtain more than seven-decade energy spectra. In following subsections, we provide the basic information of the LAT whose data is used in this thesis. More detailed description of the LAT can be found in Atwood et al. (2009).

4.1.2 The Large Area Telescope (LAT)

The LAT is designed to measure gamma rays in the energy range from 20 MeV to above 300 GeV. A pair-production process is adopted to detect photons because of the dominant cross section between a material and a photon in this energy range. The LAT is composed of 4×4 tower modules which comprise a converter-tracker (TKR) and calorimeter (CAL) and segmented Anti-coincidence Detector (ACD) encloses the towers. The schematic view of the LAT is shown in Figure 4.1.

Each TKR module is composed of the horizontally arranged 16 high-Z materials (tungsten) and 18 x-y paired silicon strip detectors (SSDs). The last 2 layers do not have the converter because the condition of the event trigger is two continuous hits. The incident photon interacting the converter produces the

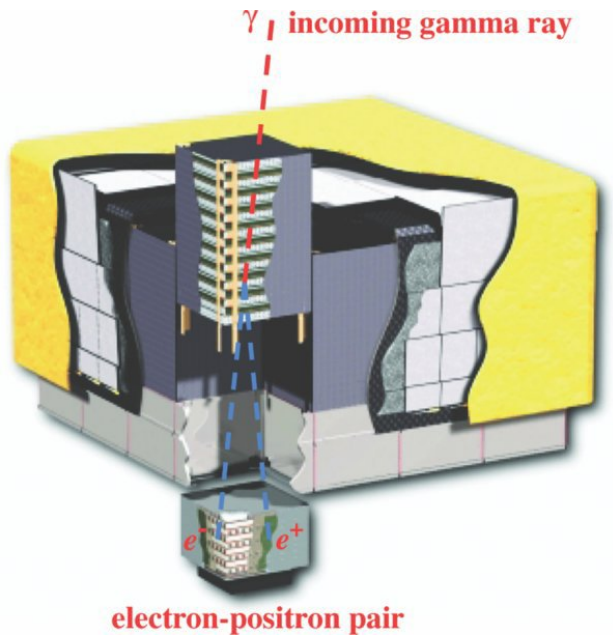

Figure 4.1 The schematic view of the LAT. Towers composed of the tracker and the calorimeter are enclosed by the anticoincidence detectors. The telescope's dimensions are 1.8 m×1.8 m×0.72 m. The figure is taken from Atwood et al. (2009).

electron and positron pairs and the SSDs measure the their track. The first 12 tungsten foils is a 3% radiation length (referred as front section) and next 4 converters is composed of thicker foils with 18% radiation length[*1] (referred as back section). The design of the front section is to minimize the separation between the conversion point in tungsten and the SSDs and to suppress the effect of the multi scattering which makes the angular resolution worse. The back section is designed to increase the probability of the conversion and make the effective area large. The SSD consists of the orthogonal two-layer structure and one extend x direction and the other y direction. This design enables the 3 dimensional reconstruction of the tracks of charged particles. The aspect ratio (length/height=0.4) of the TKRs determines the FoV.

Each CAL module is equipped bottom of the each tower and composed of 96 CsI scintillation bars. 12 bars per a row are orthogonally arranged for 8 layers (see Figure 4.2) and total radiation length of the CAL is 8.6 for normal incident (for a total instrument depth of 10.1 radiation lengths). The PIN diodes are set at each end of the bar, which measures the scintillation light that is transmitted to each end. The ratio of the scintillation light in both ends and the orthogonal alignment of the bars enable to the 3 dimensional reconstruction of the electromagnetic shower.

The external charged particles (e.g. cosmic rays) entering the LAT also interact with the detectors and become background. The primary purpose of the ACD is to remove such background charged

[*1] total 1.5 radiation length for each tower.

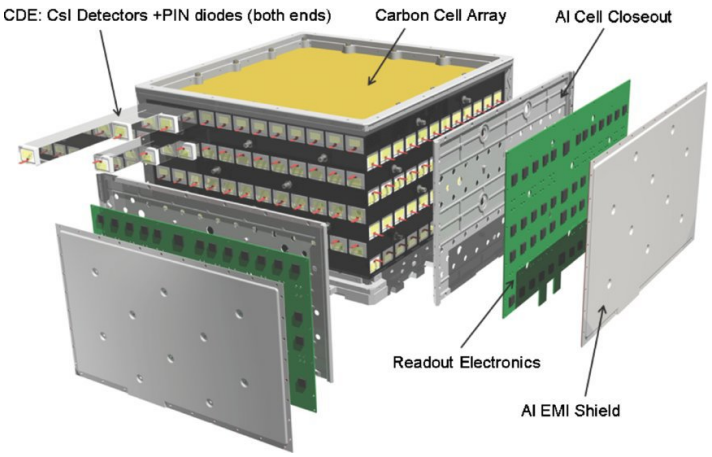

Figure 4.2 A schematic view of the LAT calorimeter module. The figure is taken from Atwood et al. (2009)

particles. The required rejection efficiency was at least 0.9997 for detection of singly charged particles entering the FoV of the LAT. The LAT is designed to detect at least 300 GeV photons and one needs to deduce the self-veto effect. The secondary charged particles produced by the electromagnetic shower in the CAL cross the ACD and create a signal via Compton scatter ("back splash"). These events also produce false veto signals. The EGRET detector on board the *Compton Gamma-Ray Observatory* suffered from the back splash effect and the effective area became worse above ~10 GeV. In order to suppress the back splash effect, the LAT ACD is segmented and composed of 89 tiles and 7 ribbons plastic scintillators. When events hit a ACD segment on the path of the incident gamma rays, the events are vetoed.

4.1.3 Event Reconstruction

In order to perform scientific analysis, the type of events (e.g. astrophysical photon) and physical parameters such as the energy and direction of incident photons must be identified from hit's signals in the detector. The framework of the event reconstruction can be improved by understanding of the LAT itself and environment on the orbit. The LAT event-level analysis framework is called "Pass". The software has been updated and released since launch: Pass 6, Pass 7, Pass 7 reprocessed and the latest version Pass 8. Before Pass 8, the main purpose of improvement is to deduce the systematic error in the instrumental response function (IRFs). The description about the IRFs is written in Section 4.1.4. The significant improvements in the event reconstruction and classification was performed for Pass 8. After *Fermi* launched, the unexpected issue was found, which is called "ghost"-event. The "ghost" event is a remnant of events which are triggered as well as good gamma-ray events and this signal causes the misclassify of the true gamma-ray event and deduces the effective area (Ackermann et al., 2012). The main purpose for Pass 8 is to minimize the "ghost" events. The new event reconstruction

method can not only the suppress the ghost events but also improve the LAT performance. For example, a clustering stage based on a Minimum Spanning Tree algorithm is introduces in the CAL. This algorithm allows to remove the charged deposition due to the "ghost" events. In addition, the new event reconstruction methods are also adopted in the TKR and ACD parts. The detailed description of Pass 8 can be found in Atwood et al. (2013).

The LAT instrument team divides reconstructed events into different classes called event class. The criteria of each class is based on their photon probability and the quality of their reconstruction. The event class is characterized by each IRF and the configuration of the event class is represented by the nested hierarchy. The higher photon probability events are characterized by smaller effective areas, narrower point spread function and lower background contamination. The level of the background contamination is defined by the isotropic diffuse gamma-ray background (Abdo et al., 2010b) (also see Section 4.1.6). The current standard event class is composed of seven types: P8R2_TRANSIENT020, P8R2_TRANSIENT010, P8R2_SOURCE, P8R2_CLEAN, P8R2_ULTRACLEAN, and P8R2_ULTRACLEANVETO. The loosest selection criteria is TRANSIENT class, which is recommended to detect a transient event such as a gamma-ray burst. For the standard source analysis, the lower background contamination event, SOURCE, CLEAN and ULTRACLEAN class are used. The SOURCE class having the moderate performance is used for a point source and extended sources such as while CLEAN and ULTRACLEAN event class are often needed in order to study a weak source or diffuse source to suppress instrumental effects for the spectral analysis. In addition, events attributed in a class subdivided into event types, which are based on the individual event topologies. The LAT team provides the 3 types of the event class: Front/Back, PSF and EDSIP. The PSF and EDSIP event type were newly added from the Pass 8. The Front/Back event is divided by the conversion points in the tracker. The Front events have a better PSF than the BACK ones because a thin converter can deduce multi scattering (also see Section 4.1.2). The PSF and EDSIP are based on the quality of the reconstructed direction and energy, respectively. One can choose the event class and the event type, which are suitable for scientific objects in own analysis.

4.1.4 LAT Performance

The LAT performance is mainly decided by three things, the hardware design, event reconstruction algorithms and background and event classification. The total performance is described by the instrumental response function (IRFs) (Ackermann et al., 2012). The IRFs make the connection between the actual gamma-ray photons and detected events. The IRFs can be factorized into three parts:

- **Effective Area** $A_{\rm eff}(\varepsilon, \hat{v}, s)$: Represents the detection efficiency. It is defined by the product of the geometric collection area, conversion probability, and the efficiency of a given event selection, s, as a function of true gamma-ray energy ε and direction $\hat{v}$ in the LAT frame. The effective

area as a function of for normal incident photon is shown in Figure 4.3 upper left panel.

- **Point Spread Function** $P(\hat{v}'; \varepsilon, \hat{v}, s)$: Represents the probability density function for the space angle between the reconstructed directions, $\hat{v}'$, for a gamma-ray energy ε and direction $\hat{v}$ in the event class s. The PSF as a function for the normal incident photon is shown in Figure 4.3 upper right panel.
- **Energy Dispersion** $D(\varepsilon'; \varepsilon, \hat{v}, s)$: Represents the probability density function to the reconstructed event energy, ε', for a gamma-ray energy ε and the direction $\hat{v}$ in the event class s. The energy dispersion as a function for the normal incident photon is shown in Figure 4.3 lower panel.

The observed gamma-ray distribution $M(\varepsilon', \hat{v}', s)$ is given by the convolution of the source model $S(\varepsilon, \hat{v})$ and the IRFs.

$$M(\varepsilon', \hat{v}', s) = \int S(\varepsilon, \hat{v}) A_{\text{eff}}(\varepsilon, \hat{v}, s) P(\hat{v}'; \varepsilon, \hat{v}, s) D(\varepsilon'; \varepsilon, \hat{v}, s) \mathrm{d}t \mathrm{d}\varepsilon \mathrm{d}\Omega \tag{4.1}$$

The integration is performed over the time and energy of interest for the analysis and solid angle in the LAT reference frame.

LAT sensitivity

The primary observation mode of the *Fermi* adopts the "scanning mode" in order to perform the efficient all-sky survey in a uniform exposure. In the scanning mode, the instrumental axis is rocked 50 degree toward north and then 50 degree toward south on the subsequent orbit. This strategy provides the uniform sky exposure after two orbits, $\sim$ 3 hours. The Figure 4.4 represents the LAT exposure on various time scales.

The sensitivity for a point source is defined as the minimum photon flux above 100 MeV to obtain the 5σ detection in ten years of observation in survey mode. The Figure 4.5 shows the point source sensitivity map in the all aky. A power-law spectrum with index 2 for the spectrum of the point source and only galactic diffuse and isotropic diffuse are considered. The sensitivity depends on the observation time, energy, spectrum of the source and intensity of the diffuse emissions. The higher flux is required to detect sources located in the galactic plane where the galactic diffuse emission becomes strong.

4.1.5 Basic Analysis Method

The imaging and spectral analysis in the mostly astrophysics is performed by the aperture photometry. The aperture photometry is done by the counts of the extracted source region subtracted by the background counts estimated by nearby source region. This simple method, however is inadequate to apply the LAT data. The galactic diffuse emission, which is the most dominant background component, is highly anisotropic (see section 4.1.6), while aperture photometry requires a more or less

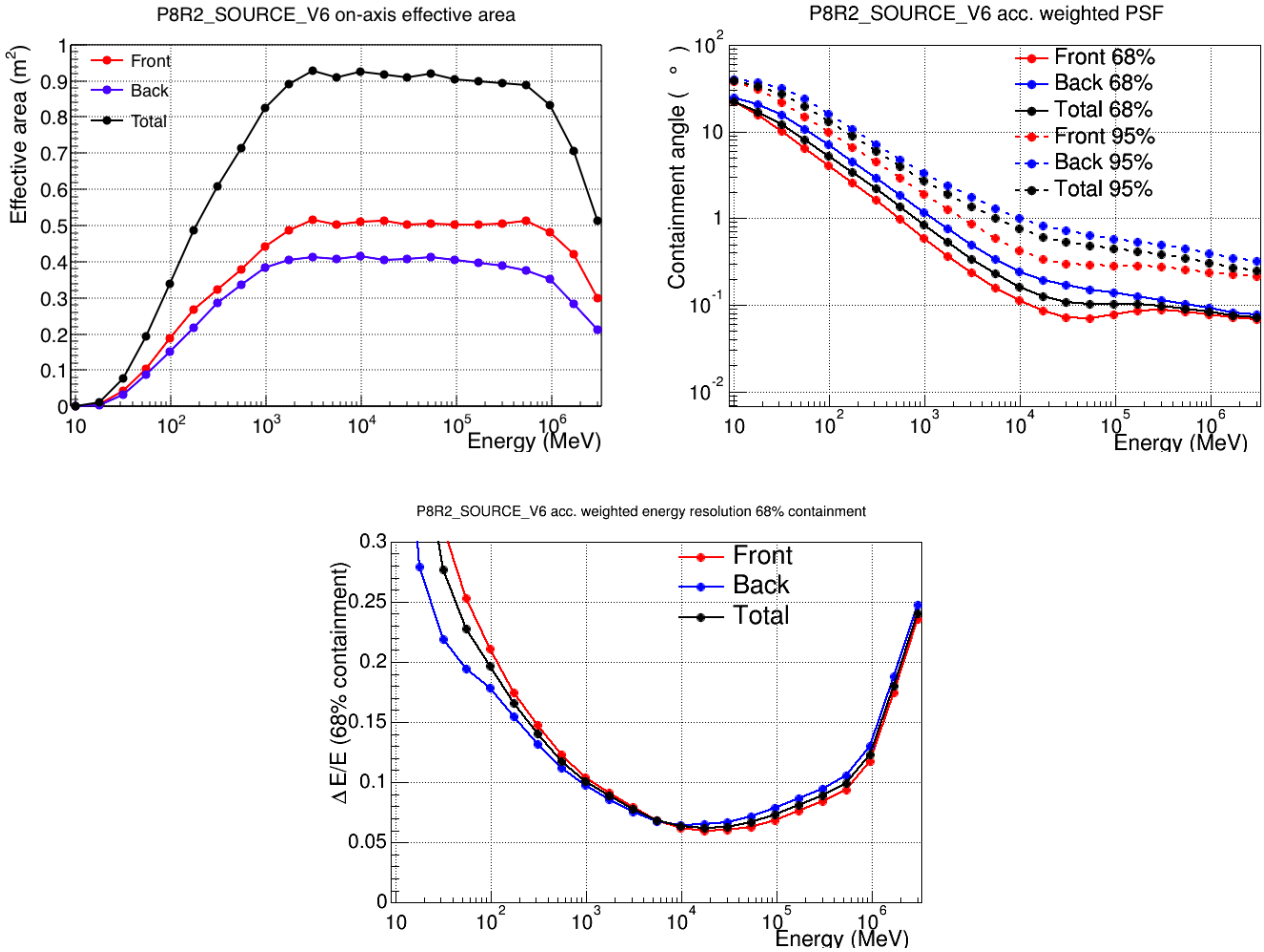

Figure 4.3 upper left: The effective as a function of energy for normal incidence photons. upper right: The point spread function as a function of energy for normal incidence photons. lower: The energy dispersion as a function of energy for normal incidence photons. The figures are taken from http://www.slac.stanford.edu/exp/glast/groups/canda/lat_Performance.html

uniform background level. In addition, PSF of the LAT becomes broader at low energy (see Figure 4.3 upper right panel). Therefore the leakage from nearby other sources can not be ignored and it is difficult to isolate the target source from background sources. Such reasons show the aperture photometry is not appropriate for the LAT data analysis.

The analysis of the LAT data has adopted maximum-likelihood method. Mattox et al. (1996) described the maximum-likelihood analysis framework developed to analyze EGRET data. The likelihood represents the probability of the data observed given a model of gamma-ray emission. The model parameters are determined by maximizing the likelihood. Since the LAT is a photon counting experiment, the probability distribution is described by the Poisson distribution. Thus the likelihood is

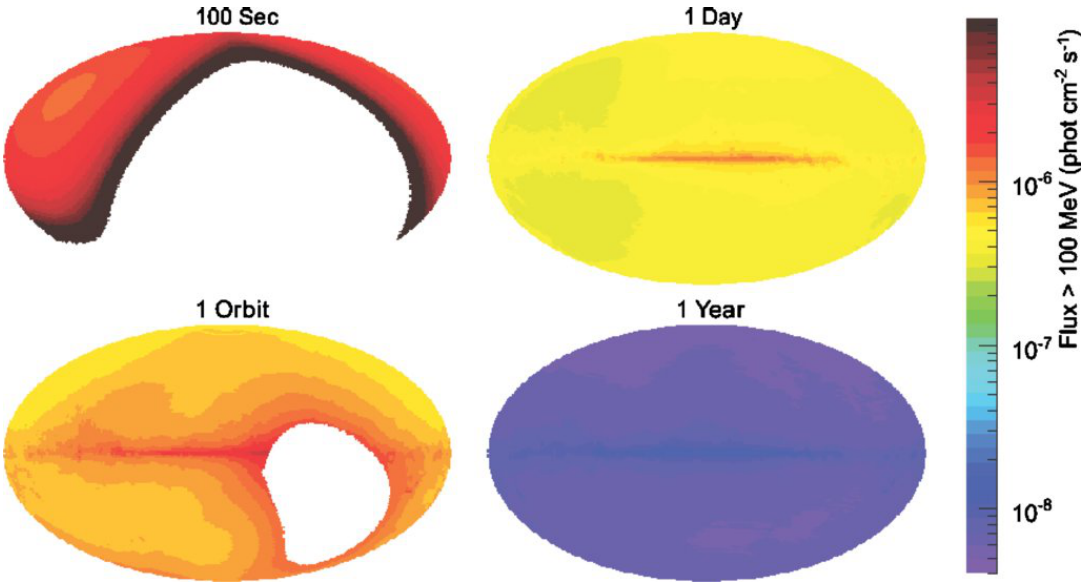

Figure 4.4 LAT all-sky exposure on various time scales. An Aitoff projection in galactic coordinates is applied in each map. In the scanning mode, the nearly uniform exposure is achieved after two orbits. The figure is taken from Atwood et al. (2009)

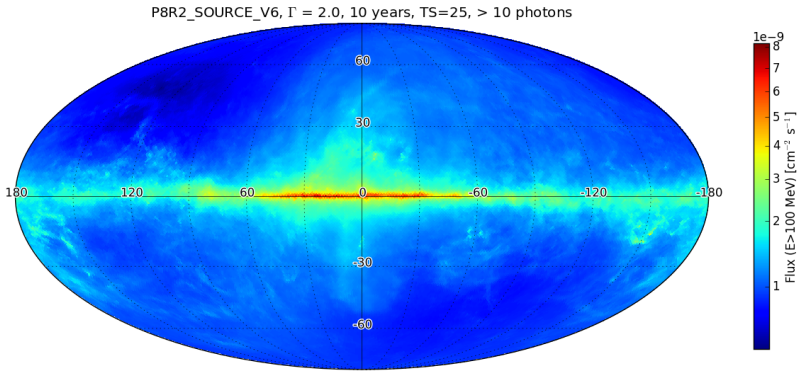

Figure 4.5 The all-sky flux sensitivty map for point sources with ten years LAT data. The power-law spectra with photon index 2 is assumed for point sources. The figure is take from https://www.slac.stanford.edu/exp/glast/groups/canda/archive/pass8v6/lat_Performance.htm

defined as follows:

$$L = \prod_{i,\,j} \frac{\theta_{ij} e^{-\theta_{ij}}}{n_{ij}!}\,, \tag{4.2}$$

where n_{ij} represents observed counts in pixel i, j and θ_{ij} shows the model-predicted number of counts in the pixel. It is computationally efficient to get the logarithm for the Eq. (4.2):

$$\ln L = \sum_{i,j} \ln\left(n_{ij}\theta_{ij}\right) - \sum_{i,j} \theta_{ij} - \sum_{i,j} n_{ij}!\,. \tag{4.3}$$

The last term represents the total observed counts, and it can be removed for the parameter estimation. The second term shows the predicted model counts, $N_{\rm pred} = \sum_{i,j} \theta_{ij}$. Eventually we can get to optimize function:

$$\ln L = \sum_{i,j} \ln\left(n_{ij}\theta_{ij}\right) - N_{\rm pred}\,. \tag{4.4}$$

`gtlike` implemented Science Tools enables us to analyze the LAT data by the maximum likelihood framework. `gtlike` provides the two methods, unbinned analysis and binned analysis. The binned analysis divides the data set into some energy and spatial bins which are chosen by the user. The likelihood analysis is performed in each bin. The finer bins enable the accurate likelihood analysis because binning means wasting photon information. The advantage of binned analysis is the faster calculation for a large data set. On the other hand, unbinned analysis is performed for one photon, and allows to calculate the accurate likelihood. This method is suitable for time series analysis, which the number of photons is not large.

Fermi employs the likelihood ratio test in order to assess the source significance and the comparison between two models. Let the model $M_1(\alpha_{k(k=1,2,\cdots,h)})$ and simpler model $M_1(\alpha_{k'(k'=1,2,\cdot,\cdot,m)})$ $(h > m)$. The test statistics is defined by

$$\mathrm{TS} \equiv 2(\ln L_1 - \ln L_0) \tag{4.5}$$

where L_1 and L_0 are the maximum likelihood value for the model M_1 (alternative hypothesis) and M_0 (null hypothesis), respectively. If these models are nested, Wilks theorem predicts the distribution of TS should be asymptotically distributed as asymptotically χ^2 with $h - m$ degree of freedoms. The detection significance of a point source at fixed position is given by the square root of TS.

4.1.6 Models for Diffuse Gamma-ray Emission

The Figure 4.6 represents the gamma-ray sky above 1 GeV observed by the LAT with 5 years of data. As we can see, the gamma-ray sky is anisotropic and concentrated on the galactic plane. In addition, there are individual sources which are blazars, pulsars and supernova remnants etc. Such emission components are not only targets of analysis but also backgrounds. The LAT data analysis based on the maximum likelihood is required to assume background models. *Fermi* collaboration distributes the background models, the gamma-ray source catalog, the galactic interstellar emission model and the

isotropic diffuse emission model, for the standard LAT data an analysis. In this section, we summarize the properties of the diffuse emission models.

Galactic Diffuse Emission model[*2]

One of the dominant component of the GeV gamma-ray sky is the emission from the galactic plane. This emission is called as the galactic diffuse emission. The galactic diffuse emission model (GDEM) gives a large effect on the source analysis especially on the galactic plane, so accurate models are required. The gamma-ray emission are produced through decay of secondary pions produced interactions of CR protons with interstellar nuclei, bremsstrahlung produced interactions of CR electrons with nucleons and inverse Compton (IC) scattering of CR electrons with low-energy photons of the interstellar radiation field (ISRF). The current GDEM is derived from a linear combination of gas column density map of H_I and CO (tracer of H_2) and the infrared dust map in order to trace the interstellar gas components (Acero et al., 2016). The H_I and CO template are divided into 9 galactocentric rings based on the galactic rotational curve (Clemens, 1985). This procedure is crucial because the method

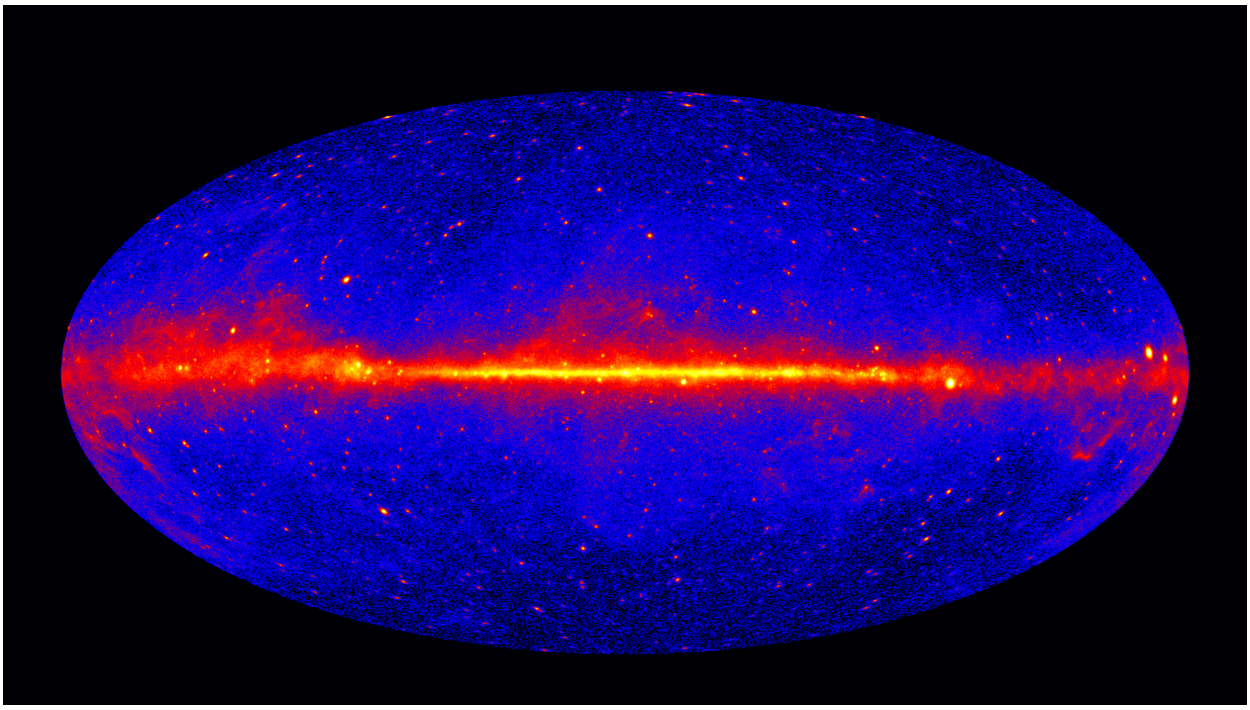

Figure 4.6 The 60-month gamma-ray sky above 1 GeV observed by the *Fermi* LAT. The only front events are used and the map is in Hammer-Aitoff projection. Image credit: NASA/DOE/Fermi LAT Collaboration

[*2]We explain the galactic diffuse emission model, "gll_iem_v06.fits". The detailed description can be found in (Acero et al., 2016)

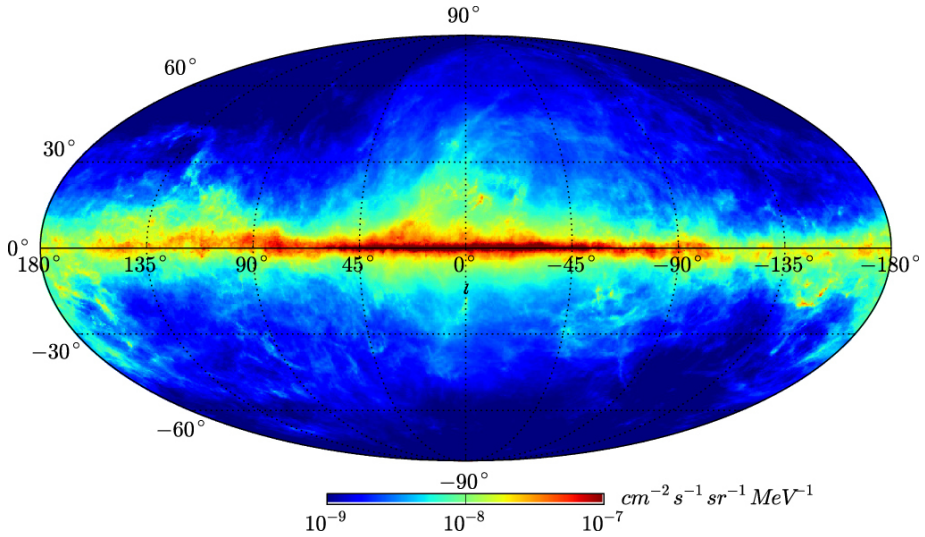

Figure 4.7 The photon specific intensity in the Galactic Interstellar Emission Model at 1 GeV. An Mollweide projection in galactic coordinate is adopted. The figure is taken from Acero et al. (2016)

of the using gas templates assumes a uniform CR density in each template. The dust map is used for corrections of over- or under-estimated gamma ray derived by the H_I and CO templates. Using these template, the gamma-ray emission which interacts with interstellar nuclei is derived.

Another important component is the IC gamma-ray. The GDEM used the CR propagation code, `GALPROP` (Strong et al., 2007) to derive the IC template, because there is no direct observational template for the IC emission. The `GALPROP` code can calculate the IC gamma-ray emission based on the propagation of electrons and the ISRF.

There are some large excesses due to the lack of suitable templates in the model while some of them exhibit relate known objects such as the Fermi bubbles and Loop I. The GDEM includes the positive residuals to explain such unknown extended components.

In summary, the GDEM is derived by summing the emission components originating from the gas annuli and dust map, from the IC emission based on the calculation of `GALPROP` code, and from excess components. The Figure 4.7 represents the GDEM at 1 GeV.

Isotropic Diffuse Emission model

The isotropic diffuse emission observed by the LAT is consists of the unresolved extragalactic sources such as blazars, star-forming and radio galaxies (Ackermann et al., 2015) and residual charged particles produced in the LAT which are misclassified as gamma rays. The spectral form of the isotropic diffuse emission model is obtained by fitting the all-sky emission excluding the galactic plane ($|b| < 10$ deg) and the Celestial poles (|Dec| > 60 deg). The misclassified probability of photons depends on the IRFs, so the isotropic diffuse emission model is prepared for each IRFs.

4.2 Observations and Results

Spaceborne gamma-ray telescopes (*Fermi* and *AGILE*) revealed that $\sim$ 100 MeV emission from the Crab Nebula is not steady source but highly active source. Most remarkable phenomena is a day-scale flux enhancement, known as flares (see, e.g., Bühler and Blandford, 2014, and references therein). Many theoretical ideas has been proposed, however we have not fully understood flares seen in the Crab Nebula. The current detection of flares is based on automated processing of the LAT data (Atwood et al., 2009). Such analysis includes both the radiation from the Crab pulsar and nebula. The phase-averaged photon flux above 100 MeV from the Crab pulsar is $\sim 2 \times 10^{-6}$ photon cm^{-2} s^{-1} (e.g., Abdo et al., 2010a; Buehler et al., 2012). So this fairly bright source may hinder detection of flares with relatively small photon flux. Detection of such hidden flares might give a clue to deeper our understanding of the physical phenomena responsible for the flaring emission. In addition, the synchrotron gamma rays show variability on all resolvable time scales (Buehler et al., 2012) and monthly variability were reported even except flares (Abdo et al., 2011). The MHD-flow models assume the synchrotron spectrum between optical to $\sim$ 1 GeV gamma ray originates the freshly accelerated electrons in the termination shock. Therefore monthly variabilities are expected to be related with the acceleration process and the magnetic field nearby the termination shock. In this section, we provided the results of the gamma-ray analysis of the Crab Nebula based on 7.4-year data obtained by the *Fermi*-LAT, which focuses on the day-scale variability and the month-scale variability.

4.2.1 Observation and Data Reduction

We analyzed the data during MJD 54686 (2008 August 8) and 57349 (2015 November 11) in the energy range between 100 MeV and 500 GeV. The data analysis was performed using the Science Tools package (v11r05p3) distributed by the Fermi Science Support Center (FSSC) following the standard procedure[*3] with the P8R2_SOURCE_V6 instrument response functions. Spectral parameters were estimated by the maximum likelihood using `gtlike` implemented in the Science Tools. We examined the detection significance of gamma-ray signals from sources by means of the test statistic (TS) based on the likelihood ratio test (Mattox et al., 1996).

Our analyses are composed of two parts: the longer-term (7.4 year) scale for the baseline state, and the shorter-term (30 day, 5 day and 1.5 day) scale for flare states. For the longer-term analysis, the events were extracted within a 21.2 $\times$ 21.2 degree region of interest (RoI) centered on the Crab Nebula position (RA: 83.6331, Dec: 22.0199). After the standard quality cut (DATA_QUAL>0&&(LAT_CONFIG==1), the events with zenith angles above 90 deg were excluded to reduce albedo gamma-ray events from the Earth limbs. The data when the Crab Nebula was within

[*3] http://fermi.gsfc.nasa.gov/ssc/data/analysis/

5 deg of the Sun were also excluded. The data were analyzed by the binned maximum likelihood method with `gtlike`. The background model includes sources within 18 degrees from the Crab Nebula as listed in the Preliminary LAT 8-year Point Source List (FL8Y)[*4]. The diameter of 18 degrees completely enclosed the RoI. Suspicious point sources, FL8Y J0535.9+2205 and FL8Y J0531.1+2200 which are located nearby the Crab Nebula (< 0.8 deg), are excluded[*5]. The supernova remnants IC 443 and S 147 are included as spatial extended templates. Both normalizations and spectral parameters of the sources which are located within 5 degrees from the Crab Nebula set free while the parameters of all other sources are fixed at the FL8Y values. The galactic diffuse emission model "gll_iem_v06.fits" and the isotropic diffuse emission model "iso_P8R2_SOURCE_V6_v06.txt" are included in the background model. A normalization factor and photon index for the galactic diffuse emission model and a normalization factor for the isotropic diffuse emission model set free. Sources with TS of less than 1 were removed after the first iteration of the maximum likelihood fit and then we fitted data again. We excluded the known flare periods as reported in Mayer (2015) and Rudy et al. (2015) to determine the base-line state in our long-term analysis. We defined the flare periods as two weeks before or after the peak flare times. The flare periods which were excluded in our long-term analysis are summarized in Table 4.1. In this paper, we refer those flares as "reported flares".

Table 4.1 List of the periods of"reported flares". Those periods were excluded in our long-term analysis to determine the base-line state of the source.

Flare name	MJD	reference
February 2009	54855 - 54883	Mayer (2015)
September 2010	55446 - 55474	Mayer (2015)
April 2011	55653 - 55681	Mayer (2015)
July 2012	56098 - 56126	Mayer (2015)
March 2013	56343 - 56371	Mayer (2015)
October 2013(1), (2)[a]	56568 - 56608	Rudy et al. (2015)
August 2014(1), (2)[a]	56869 - 56902	Rudy et al. (2015)

a The light curve shows a two-peak structure (Rudy et al., 2015).

For the shorter-term analysis, the events were extracted within a 15-degree acceptance cone centered on the location of the Crab Nebula, and the gamma-ray fluxes and spectra were determined by unbinned maximum likelihood method. The background model is the same one as used in the long-term analysis, but parameters are fixed by the results from our long-term analysis, except for the isotropic diffuse emission, whose normalization sets free. *Fermi*-LAT cannot positionally distinguish gamma-ray emission originated from between the Crab pulsar and nebula due to its large PSF. Thus, off-pulse

[*4] https://fermi.gsfc.nasa.gov/ssc/data/access/lat/fl8y/

[*5] The fourth Fermi Large Area Telescope source catalog (The Fermi-LAT collaboration, 2019) has just recently published and does not include those two sources.

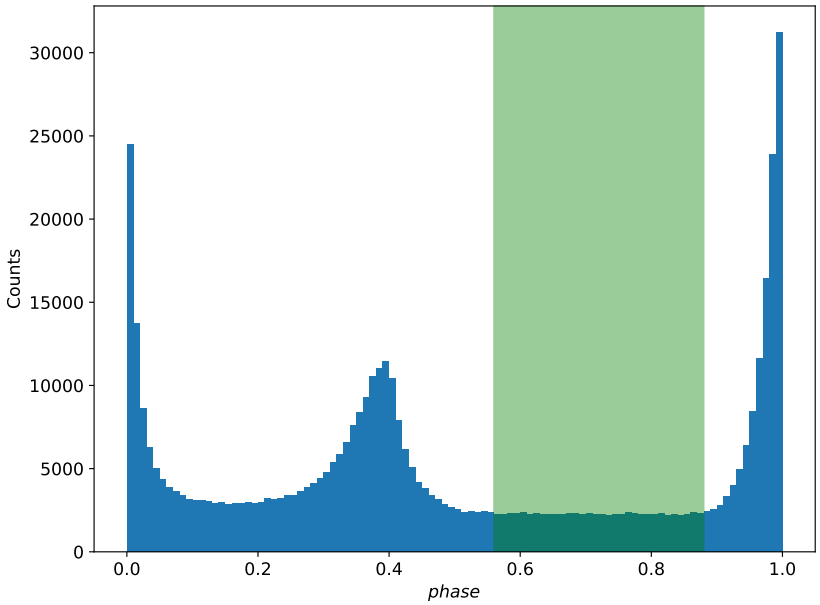

Figure 4.8 Phase profile of gamma rays above 100 MeV within 3 deg of the Crab pulsar for the 7.4-year data of *Fermi* observations. The green shadow region represents the adopted off-pulse interval [0.56-0.88] where the emission is dominated by the nebula.

window of the Crab pulsar are needed to get an accurate spectrum of the Crab Nebula. For this purpose, we used TEMPO2 package[*6] (Hobbs et al., 2006) for phase gating analysis. The ephemeris data was prepared following the methods outlined in Kerr et al. (2015). The result of the phase calculation is shown in Figure 4.8. The 3 degree of radius is chosen for the extract region. The duration of the ephemeris data of the Crab pulsar is between MJD 54686 and 57349 and the phase interval was chosen during 0.56-0.88 to sufficiently suppress effects from the pulsar (green shadow region in Figure 4.8) (e.g. Abdo et al., 2010a). In summary, we performed the long term analysis to determine the base-line spectral parameters and the short-time analysis to detect and characterize "small flares". All analysis procedures were performed using the off-pulse data of the Crab pulsar as the similar way in Abdo et al. (2011).

4.2.2 Spectral Model

A gamma-ray spectrum of the Crab Nebula has two components in the LAT energy band. One is a synchrotron component which has a soft spectrum and the other is an IC component which dominates above 1 GeV. We assume a power law spectrum (PL) for the synchrotron component and logparabola

[*6] http://www.atnf.csiro.au/research/pulsar/tempo2/index.php?n=Main.HomePage

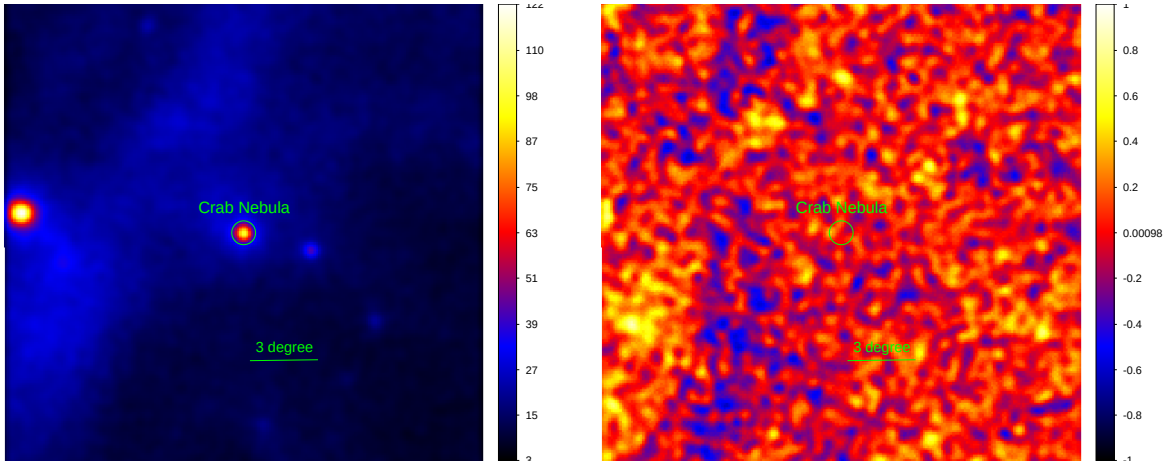

Figure 4.9 left: Count map in region of interest (21.2 × 21.2 degree) for the base-line analysis. right: Residual map in region of interest. The σ =0.2 degree gaussian smoothing was applied for both image.

(LP) spectrum for the IC component for the Crab Nebula spectrum:

$$\frac{dN}{d\varepsilon} = N_{0,\mathrm{SYN}} \left(\frac{\varepsilon}{100\ \mathrm{MeV}} \right)^{-\Gamma_{0,\mathrm{SYN}}} + N_{0,\mathrm{IC}} \left(\frac{\varepsilon}{1\ \mathrm{GeV}} \right)^{-(\alpha_0 + \beta_0 \ln(\varepsilon/1\ \mathrm{GeV}))}, \tag{4.6}$$

where ε represents the photon energy. We performed the maximum likelihood analysis of data between MJD 54686 and 57349 excluding the "reported flares" as defined in Sec 4.2.1, and obtained the spectrum values, $\Gamma_{0,\mathrm{SYN}} = 4.27 \pm 0.08$, $\alpha_0 = 1.50 \pm 0.04$, $\beta_0 = 0.05 \pm 0.01$. The photon flux above 100 MeV is $F_{\mathrm{ph,SYN}} = (6.31 \pm 0.23) \times 10^{-7}$ photon cm^{-2} s^{-1} for the synchrotron component and $F_{\mathrm{ph,IC}} = (1.09 \pm 0.08) \times 10^{-7}$ photon cm^{-2} s^{-1} for the IC component whereas the energy flux is $F_{\mathrm{e,SYN}} = (1.45 \pm 0.06) \times 10^{-10}$ erg cm^{-2} s^{-1} and $F_{\mathrm{e,IC}} = (5.46 \pm 0.28) \times 10^{-10}$ erg cm^{-2} s^{-1}. In the following sections, we refer these values as the base-line values. The Figure 4.9 left shows the total count map of the RoI and the Crab Nebula is located in the center of the image. The bright source which located the nearby the east end is the supernova remnant IC 443. The IC 443 is known to be a extended source and a "middle-age" supernova remnant (∼ 10000 years) (e.g. Abdo et al., 2010c) . One does not expect any time variability from a such source and the variability has not been seen in the IC 443 at the present. In order to the validity of the `gtlike` results, we made a residual map. A residual map is the differential map between the observed count map and modeled count map. We also divided the residual map by the square-root scaled model map to compare with the statistical error. The resulting map is shown in Figure 4.9 right.

Figure 4.10 represents the base-line spectral energy distribution of the Crab Nebula. The spectral points were obtained by dividing the 100 MeV and 500 GeV range into 15 logarithmically spaced energy bins.

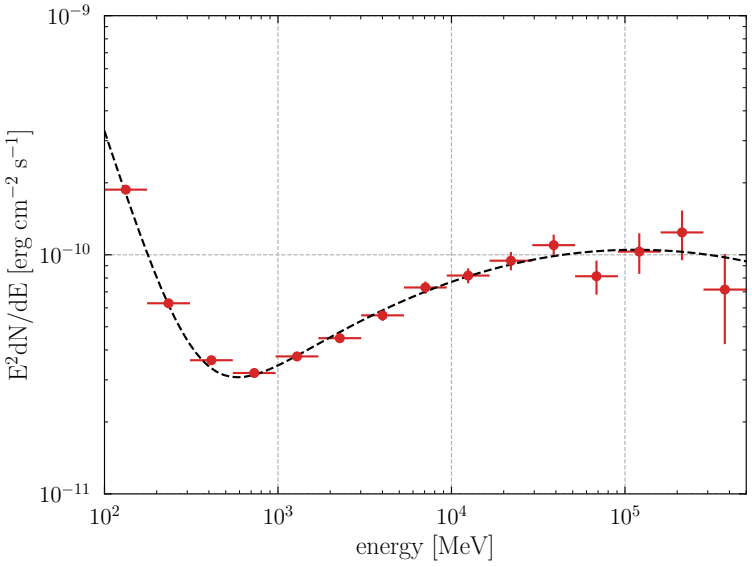

Figure 4.10 Spectral energy distribution for the Crab Nebula averaged over the 7.4 years of *Fermi* observations excluding the "reported flare" durations listed in Table 4.1. Only the data of the off-pulse phase (phase interval: [0.56-0.88]) were used. The dashed black line represents the best-fitted model of the Crab Nebula (synchrotron component + inverse Compton component) described by Eq. (4.6)

4.2.3 Search for Small Flares

Detection of "Small Flares"

We derived a 5-day binned light curve (LC) of the synchrotron and the IC component based on the Eq. (4.6) and tried the χ^2 test to examine a variability. The χ^2 test of the synchrotron component was performed using the integral flux between 100 MeV - 500 GeV and we treated the normalization and photon index of the synchrotron component, the IC component and the isotropic diffuse emission as free parameters while the others were fixed by the base-line values. On the other hand, we chose 5-500 GeV to perform the χ^2 test of the IC component to suppress the effect of the synchrotron component and the normalizations of the IC component and isotropic diffuse emission set free. The resulting LC is shown in Figure 4.11. The data points of TS < 0 were excluded for the χ^2 test because the statistical error of such low significant data points is not calculated correctly. Note that such low significant data points must have a large statistical error and the effect of the χ^2 value is small. The χ^2 is defined as follow:

$$\chi^2_{\mathrm{SYN/IC}} = \sum_i \frac{(F_{\mathrm{i,\,SYN/IC}} - F_{\mathrm{base,\,SYN/IC}})^2}{F^2_{\mathrm{i,\,err,SYN/IC}}} \tag{4.7}$$

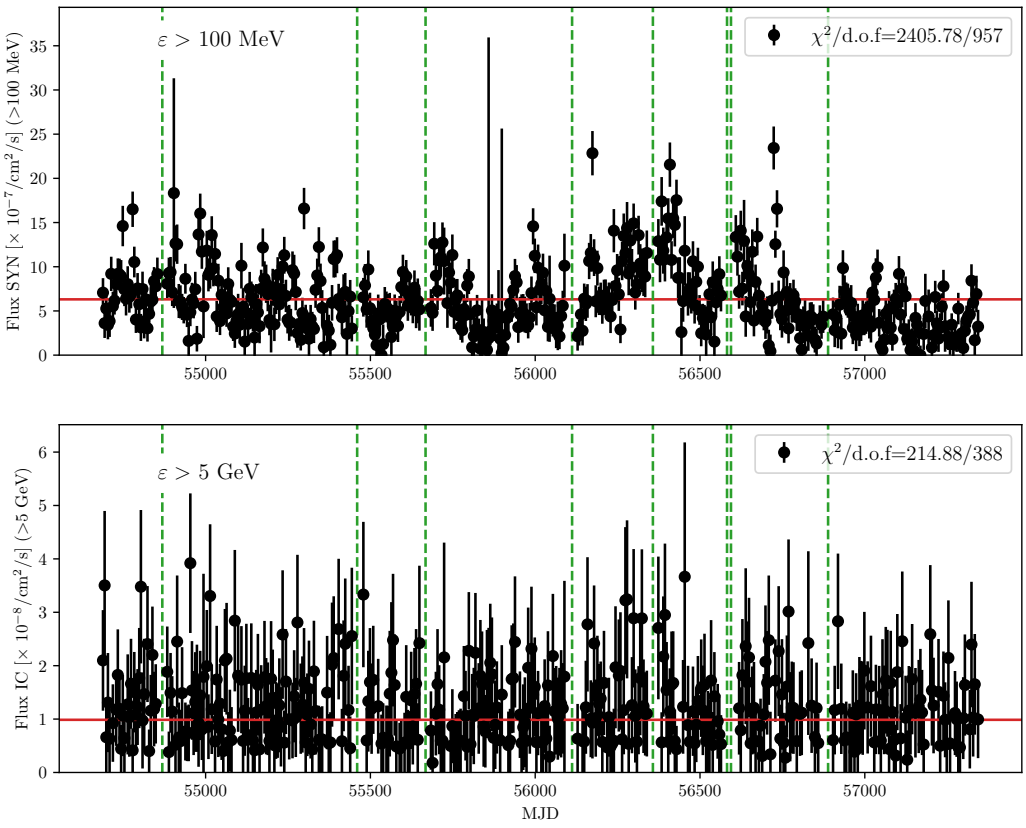

Figure 4.11 top: 5-day gamma-ray light curve (integral photon flux) of the Crab synchrotron component between 100 MeV and 500 GeV. bottom: 5-day gamma-ray light curve (integral photon flux) of the Crab inverse Compton component between 5 GeV and 500 GeV. The data duration is from August 2008 to November 2015. The green lines show the times of the reported flares listed in Table 4.1. The data points which overlapped with the reported flare duration are excluded.

where $F_{\mathrm{i,\,SYN/IC}}$ and $F_{\mathrm{i,err,\,SYN/IC}}$ is a value of the flux and error of the synchrotron and IC component in each LC-bin, respectively. The obtained $\chi^2_{\mathrm{SYN/IC}}$/ (d.o.f) are $\chi^2_{\mathrm{SYN}} = 2405.78/957$ and $\chi^2_{\mathrm{IC}} = 214.88/388$. The constant model is disfavored in the synchrotron component, while the IC component is consistent with the constant model. It has been reported that the IC component does not show any variability by previous LAT analysis (Abdo et al., 2011; Buehler et al., 2012; Mayer et al., 2013; Yeung and Horns, 2019) and by ground-based imaging air Cherenkov telescopes observation (H. E. S. S. Collaboration et al., 2014; Aliu et al., 2014; Aleksić et al., 2015). Thus in the following analysis, we assume the spectral parameters of the IC component ($N_{0,\mathrm{IC}}$, α_0 and β_0) are fixed at the base-line values. The 5-day LC of the synchrotron component is represented in the Figure 4.12. The upper panels showed the LC of

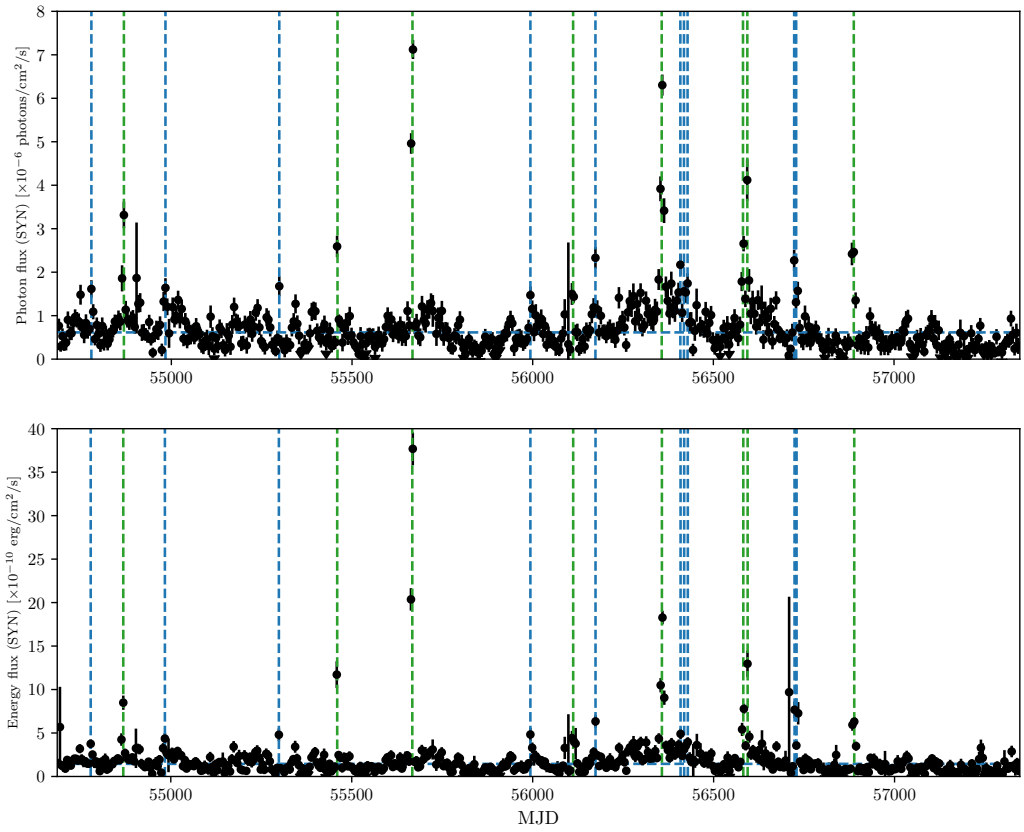

Figure 4.12 top: 5-day gamma-ray light curve (integral photon flux) of the Crab synchrotron component. bottom: 5-day gamma-ray light curve (integral energy flux) of the Crab synchrotron component. The time range is from August 2008 to November 2015 and the energy range is between 100 MeV and 500 GeV. The green lines show the times of the reported flares listed in Table 4.1. The center times of the small flares from this work are indicated in blue lines as listed in Table 4.2

the photon flux and the lower one is energy flux. There is some bins which shows the flux enhancement except for the reported flares. To identify flare activity of the synchrotron component of the Crab Nebula emission, we modeled the emission as a superposition of three components; synchrotron, IC and additional flare components, in a similar way as Abdo et al. (2011). The flare component is modeled by the PL with free normalization and photon index parameters while the synchrotron and IC component are fixed by the base-line values. We define "small flares" as TS value of the flare component is larger than 29. This corresponds to the significance of $\sim 5\sigma$ with 2 degrees of freedom (pre-trial) or $\sim 3.7\sigma$ considering trials for the 525 LC bins. The center time (MJD) of the LC bin and the TS of detected "small flares" are summarized in Table 4.2. The center times of small flares are

also shown in Figure 4.12 as blue lines. All "reported flares" listed in Table 4.1 satisfy the criteria of TS>29.

Table 4.2 List of detected "small flares"

name	Bin midpoint (MJD)	TS (significance[a])
small flare 1	54778.65	32.6 (4.1σ)
small flare 2[b]	54983.65	32.4 (4.1σ)
small flare 3	55298.65	34.4 (4.3σ)
small flare 4[c]	55993.65	37.3 (4.6σ)
small flare 5	56173.65	78.2 (7.8σ)
small flare 6	56408.65	59.4 (6.5σ)
small flare 7	56418.65	30.2 (3.8σ)
small flare 8	56428.65	30.9 (3.9σ)
small flare 9[d]	56723.65, 56728.65, 56733.65	93.4, 31.7, 66.0 (8.7σ, 4.0σ, 7.1σ)

a corresponding significance with 2 degrees of freedom with 525 trials

b This was indicated as the minor flare in Striani et al. (2013).

c This was indicated as the "wave" in Striani et al. (2013).

d ATel #5971 (Gasparrini and Buehler, 2014).

Effect on the Detection Significance from the Crab pulsar

So far, our analysis was performed based on the off-pulse analysis. The off-pulse analysis can deduce the systematic error from the Crab pulsar while the exposure time also becomes small because of the pulsar gating. Here, we performed the all-phase analysis and examined how the Crab pulsar affects the detection of the flare component.

We analyzed the data during MJD 54683 and MJD 58270 in the energy range between 100 MeV and 500 GeV in order to determine the base-line result of the all-phase analysis. The difference of time range between all phase analysis and off-pulse analysis is the limitation of the time range of the ephemeris data. The reported flare durations shown in Table 4.1 are excluded to suppress the bright flare effects from the Crab Nebula. The event reprocess is the same as the description in the Section 4.2.1 while the Crab pulsar was added in the source models. The Crab pulsar is modeled as a power law with a exponential cutoff:

$$\frac{dN}{d\varepsilon} = N_0 \left(\frac{\varepsilon}{100\ \mathrm{MeV}} \right)^{-\Gamma} \exp\left[\left(-\frac{\varepsilon}{\varepsilon_{\mathrm{cut}}} \right)^{\beta} \right], \tag{4.8}$$

where N_0, Γ and β represent the normalization, the photon index and the cut-off index. We assumed $\beta = 2/3$, which means sub-exponential cutoff shape. The likelihood analysis via provided the spectral values of the Crab pulsar, $F_{\mathrm{pulsar}} = (2.03 \pm 0.01) \times 10^{-6}$ cm^{-2} s^{-1}, $F_{\mathrm{e,pulsar}} = (8.27 \pm 0.03) \times 10^{-4}$ erg cm^{-2} s^{-1}, $\Gamma = 1.85 \pm 0.01$ and $\varepsilon_{\mathrm{cut}} = 3.3 \pm 0.1$ GeV. The residual map in units of the square root of the model

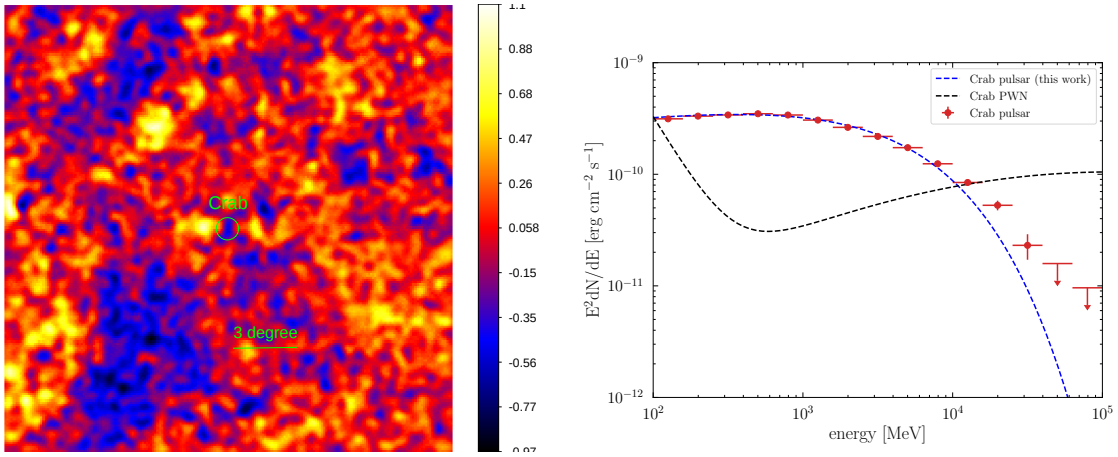

Figure 4.13 left: Residual map in region of interest (21.2 × 21.2 degree).The σ =0.2 degree gaussian smoothing was applied for both image. right: Spectral energy distribution of the Crab pulsar. The dashed blue lines and the dashed black line represent the best fitted spectrum of the Crab pulsar and the Crab Nebula spectrum, respectively. The spectrum of the Crab Nebula was obtained via the off-pulse analysis and the spectral parameters are fixed by the base-line results.

counts is shown in Figure 4.13 left. We called these best fit models as the base-line (all phase) in this thesis.

The SED of the Crab pulsar is also shown in Figure 4.13 right with the best fitted line (dashed blue line). The spectral points were obtained by dividing the 100 MeV and 500 GeV range into 15 logarithmically spaced energy bins. The SED shows a discrepancy between the best fitted line obtained by the likelihood analysis and the data points which do not have a model dependence. This suggests the β in Eq. 4.8 should be smaller value, which was also indicated by the TeV gamma-ray telescopes (Aleksić et al., 2011; VERITAS Collaboration et al., 2011). Here, we attempt to examine effects on the detection significance of the Crab flare component by the systematic error from the Crab pulsar. The lower energy part $\lesssim$ 10 GeV is important because of the large photon fluxes, so we ignore the discrepancy which appears at high energy range.

We derived the 5-days binned LC of the Crab Nebula synchrotron component to identify the Crab flare component. The flare component was added by the power-law model with the normalization and the photon index set free and the normalization of the isotropic diffuse emission set free. The all other spectral parameters including the Crab Nebula and the Crab pulsar are fixed by the base-line values (all phase). The threshold of the detection of the flare component is adopted as the same as the off-pulse analysis, i.e. TS>29. The list of the detected "small flare" is shown in the Figure 4.14.

In order to compare the flux level between the flare component and the Crab pulsar, the flux of the flare component with TS>29 were also shown in the Table 4.3[*7]. We additionally detected seven "small flares (here we describe new ones as flare candidates)" using all phase data. All "small flare" except

[*7] flux value was derived by the off-pulse analysis.

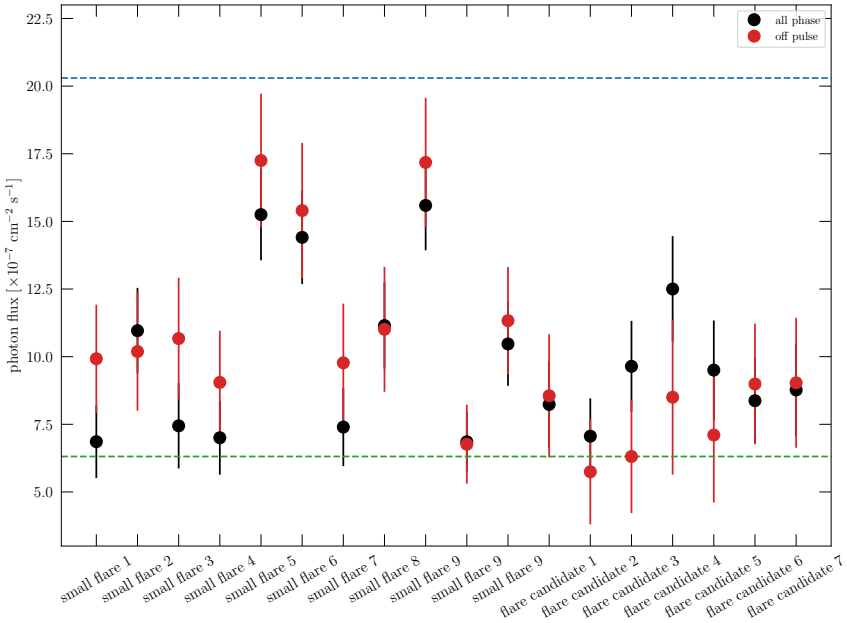

Figure 4.14 Comparison with the fluxes of the flare component between the off-pulse analysis (red points) and all-phase analysis (black points). The green dashed line and blue dashed line represent the flux of the Crab Nebula synchrotron component and the flux of the Crab pulsar, respectively.

for "small flare 3" were detected in both off-pulse analysis and all-phase analysis. On one hand, the fluxes of the small flares are typically 50 % of the flux of the Crab pulsar (also see following figure) and the systematic errors of the Crab pulsar might affect the detection significance of the flare component. In order to examine the effects from the Crab pulsar, we artificially changed the normalization of the Crab pulsar by 2% and 5%. The systematic error 2% is based on the systematic error based on the stability of the LAT pulsars (Nolan et al., 2012) and 5% is based on the uncertainties on the effective area without accounting for energy dispersion[*8]. The list of TS values and the photon fluxes of the flare components are following. (The red points and the black points represent the fluxes of the all-phase analysis and the off-pulse analysis, respectively. The blue line and the green line represent the averaged flux of the Crab pulsar and the Crab synchrotron, respectively.)

Generally, the results from the all-phase analysis show higher TS values, however Table 4.3 indicates the TS values are significantly affected by the systematic uncertainty of the Crab pulsar emission. It is naturally expected because the typical flux of the small flares is smaller than the flux of Crab pulsar (also see Figure 4.14).

Our primary purpose is not to maximize the number of the flare detections, but to establish the

[*8] https://fermi.gsfc.nasa.gov/ssc/data/analysis/scitools/Aeff_Systematics.html

Table 4.3 List of the flare component between all-phase analysis and off-pulse analysis.

flare id	MJD	off pulse TS	all phase TS	all phase pulsar flux 2% up	all phase pulsar flux 5% up
small flare 1	54778.65	32.6	31.7	28.9	23.9
small flare 2	54983.65	32.4	61.0	57.0	49.7
small flare 3	55298.65	34.4	25.2	22.3	17.2
small flare 4	55993.65	37.3	31.3	27.2	20.0
small flare 5	56173.65	78.2	103.7	97.8	86.8
small flare 6	56408.65	59.4	97.6	93.2	85.2
small flare 7	56418.65	30.2	35.6	34.3	30.7
small flare 8	56428.65	30.9	60.2	36.3	49.3
small flare 9	56723.65	93.4	117.3	110.0	96.4
small flare 10	56728.65	31.7	44.9	39.3	29.6
small flare 11	56733.65	66.0	58.3	53.0	43.3
flare candidate 1	54748.65	19.7	32.5	29.3	23.6
flare candidate 2	54988.65	11.2	31.1	28.7	24.4
flare candidate 3	55343.65	13.0	39.5	36.5	30.6
flare candidate 4	56373.65	11.9	58.1	53.5	45.0
flare candidate 5	56278.65	10.5	31.0	28.5	24.2
flare candidate 6	56403.65	21.7	36.4	34.1	29.8
flare candidate 7	56423.65	19.7	33.2	30.9	26.8

presence of small-flux flares more reliably. Therefore, we conservatively adopted the results of off-pulse analysis to avoid the possible systematic uncertainties caused by the component of the Crab pulsar emission in the following analysis.

Time Profile of Each Flare

In order to analyze detailed structures of "small flares" and "reported flares" we made 1.5-day binned LCs for one month centered at the small-flare times listed in Table 4.2 and the durations of "reported flares" listed in Table 4.1. In the same manner as the 5-day binned LC in Figure 4.12, the Crab Nebula is modeled by Eq. (4.6) and $N_{0,\mathrm{SYN}}$, $\Gamma_{0,\mathrm{SYN}}$ and the normalization of isotropic diffuse emission set free. Figure 4.15 represents the 1.5-day binned LCs in the energy range of 100 MeV to 500 GeV during "small-flare" and "reported-flare" periods. The LCs are fitted by the following function to characterize the time profiles of both "small flares" and "reported flares" :

$$F(t) = F_{\mathrm{b}} + \frac{F_0}{e^{-(t-t_0)/\tau_{\mathrm{rise}}} + e^{(t-t_0)/\tau_{\mathrm{decay}}}} \tag{4.9}$$

where F_{b} is an assumed constant level underlying a flare, F_0 is an amplitude of a flare, t_0 describes approximately a peak time (it corresponds to the actual maximum only for symmetric flares), τ_{rise} and τ_{decay} describe the characteristic rise and decay times. The time of the maximum of a flare (τ_{peak}) can be described using parameters in Eq. (4.9) as:

$$t_{\mathrm{peak}} = t_0 + \frac{\tau_{\mathrm{rise}}\tau_{\mathrm{decay}}}{\tau_{\mathrm{rise}} + \tau_{\mathrm{decay}}} \ln\left(\frac{\tau_{\mathrm{decay}}}{\tau_{\mathrm{rise}}}\right) \tag{4.10}$$

This formula is often used to characterize flare activities of blazars (e.g., Hayashida et al., 2015). We note that the small flare 7 and 2014 August flare are not fitted well by Eq. (4.9). These flares may be of combined effects of the statistical fluctuation or superpositions of short and weak flares which can not be resolved by the *Fermi*-LAT. So, we do not estimate the characteristic time scale of the small flare 7 and 2014 August flare in this paper. We divide the small flare 9 and the 2013 October flare into two flares (a) and (b) for each because each shows a two-peak structure. The fitting results are summarized in Table 4.4, and the best fitted profiles are overlaid in Figure 4.15 as a dashed line. We compare energy fluxes and photon indices at the flare peaks in Figure 4.16-(a), and fluences and photon indices in Figure 4.16-(b) for individual flares. The flare peak is defined as the highest flux bin in each panel of Figure 4.15 and the energy fluxes and photon indices were taken from the results of corresponding bins. The flare fluences were defined with integrations over periods between between $t_{\mathrm{peak}} - \tau_{\mathrm{rise}} \leq t \leq t_{\mathrm{peak}} + \tau_{\mathrm{decay}}$, based on the best fitted time profile model as listed in Table 4.4. The fluence and photon index were calculated with `gtlike` from data resampled by those integration periods. Figure 4.16-(a) indicates "harder when brighter" trend, which could imply electron spectra with higher cut-off energies or stronger magnetic fields for the bright flaring states. Although the current data set alone does not allow one to constrain the nature of the base-line and flaring components, the "harder when brighter" feature implies some statistical effects, such as the Doppler boosting which depends on the motion direction of relativistic fluid elements and the fluctuation of the magnetic field, play an important role.

In the fluence vs. photon index plot shown in Figure 4.16-(b), two flares clearly shows high fluences. One corresponds to the 2011 April flare with the largest energy flux $\sim 85 \times 10^{-10}$ erg cm^{-2} s^{-1},

Table 4.4 Fitting results of the 1.5-days light curve

flare id	F_b [$\times 10^{-10}$ erg cm^{-2} s^{-1}]	F_0 [$\times 10^{-10}$ erg cm^{-2} s^{-1}]	τ_{rise} [day]	τ_{decay} [day]	t_0 [MJD]
small flare 1	1.4 ±0.2	5.6 ±2.0	0.3 ±0.4	3.3 ±1.7	54777.4 ±1.0
small flare 2	1.5 ±0.4	9.0 ±2.6	0.7 ±0.5	3.2 ±1.3	54980.2 ±0.7
small flare 3	1.1 ±0.4	10.6 ±2.8	1.1 ±1.0	1.3 ±0.9	55299.1 ±1.6
small flare 4	1.3 ±0.4	10.6 ±3.1	0.6 ±0.4	2.7 ±1.1	55991.4 ±0.6
small flare 5	2.0 ±0.3	12.5 ±4.2	0.4 ±0.2	1.8 ±0.8	56172.7 ±0.5
small flare 6	1.9 ±0.6	4.3 ±1.7	7.0 ±3.7	0.2 ±2.3	56409.5 ±1.2
small flare 8	2.4 ±0.3	6.0 ±2.5	0.9 ±0.9	2.1 ±1.7	56425.2 ±1.5
small flare 9 (a)	0.6 ±1.0	23.5 ±4.8	2.1 ±0.9	0.5 ±0.2	56726.6 ±0.5
small flare 9 (b)	1.9 ±0.5	20.6 ±9.3	1.3 ±0.7	0.4 ±0.3	56735.2 ±0.5
2009 Feb	2.5 ±0.3	16.3 ±3.8	2.3 ±0.9	0.7 ±0.3	54869.5 ±0.6
2010 Sep	1.6 ±0.3	30.0 ±6.6	1.7 ±0.6	1.0 ±0.3	55460.0 ±0.6
2011 Apr	1.8 ±0.3	142.7 ±10.8	1.6 ±0.1	0.6 ±0.1	55668.0 ±0.1
2012 July	1.8 ±0.6	11.2 ±3.5	3.3 ±1.4	0.3 ±1.2	56113.6 ±0.8
2013 Mar	2.3 ±0.5	34.2 ±2.0	2.4 ±0.4	3.6 ±0.6	56356.8 ±0.6
2013 Oct (a)	1.8 ±0.4	23.6 ±3.4	2.2 ±0.6	0.8 ±0.2	56583.4 ±0.3
2013 Oct (b)	3.3 ±0.4	30.0 ±55.5	0.5 ±7.7	1.1 ±1.1	56594.6 ±4.9

and the other is the 2013 March flare with the second largest flux and long flare duration (see Table 4.4)[*9]. Apart from those two flares, the "reported flares" and the "small flares" show similar results: the same range of photon index, "harder when brighter" trend. Thanks to the detection of "small flares", the number of flares becomes large and we can obtain a fluence distribution of flares. The fluecne distribution indicates that the extremely large intensity flares (2011 April and 2013 March), which were studied in detailed (Buehler et al., 2012; Mayer et al., 2013), are rather exception and the other flares provides the main contribution among flares. In addition, the current detection of flares is limited by the sensitivity of the gamma-ray detectors. This implies that weaker-intensity flares must exist. Detection of "small flares" suggests flares are not so rare events and may provide a not small contribution to the persistent emission observed in the Crab Nebula.

[*9] in the 2013 March flare, rapid variability of ~5-hour scale has been reported using orbit-binned (~ 90 minutes) LC (Mayer et al., 2013). Our analysis is based on 1.5-day binned LC and focuses on more global feature of the flare.

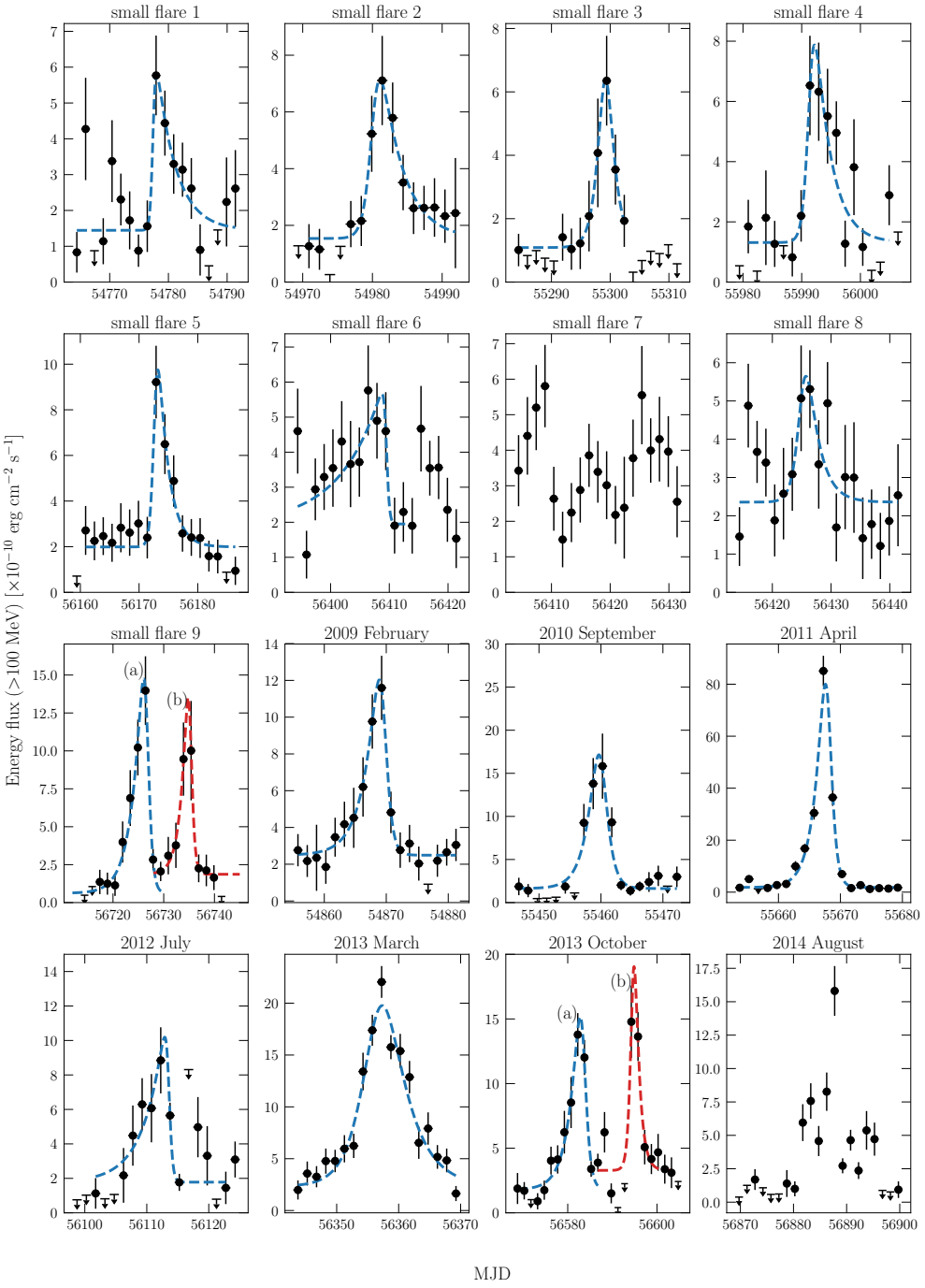

Figure 4.15 1.5-day binned gamma-ray light curve between 100 MeV and 500 GeV of the Crab synchrotron component during each "small flare" and "reported flare". The vertical error bars in data points represent 1σ statistical errors and the down arrows indicate 95% confidence level upper limits. The blue and red lines represent the best fitted time profiles defined as Eq. (4.9).

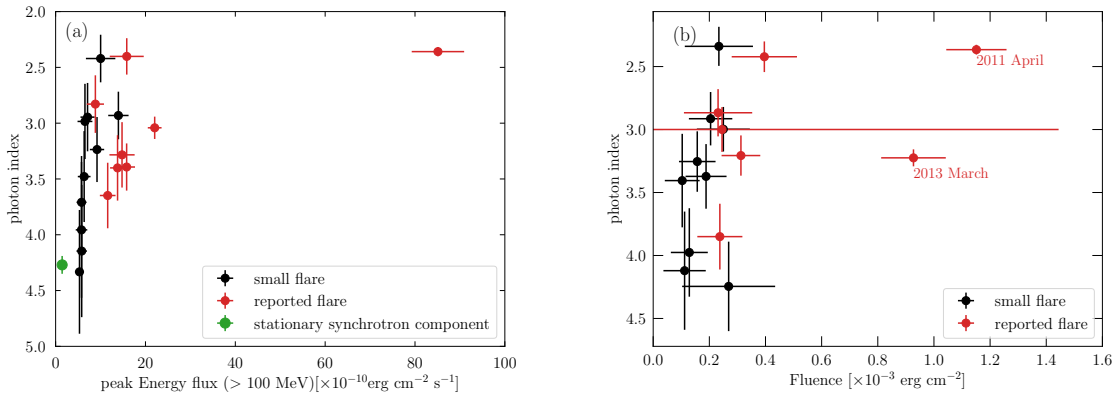

Figure 4.16 (a): Scatter plot of the photon index and the peak energy flux (100 MeV - 500 GeV). Black data points indicate "small flares" and red points show "reported flare". The green data point represents the base-line value. (b): scatter plot of the photon index and fluence. The fluence is defined by integrated emission over a period between $t_{peak} - \tau_{rise}$ to $t_{peak} + \tau_{decay}$ Black data points indicate "small flares" and red points show "reported flare". The small flare 7 and 2014 August flare are not shown in this plot because they have a complex time profile.

To examine a possible spectral curvature, we applied not only a power-law model, but also a power law with an exponential cut-off model for the Crab synchrotron component. The power law with an exponential cut-off model is defined as

$$\frac{dN}{d\varepsilon} = N\left(\frac{\varepsilon}{100\ \mathrm{MeV}}\right)^{-\Gamma} \exp\left(-\frac{\varepsilon}{\varepsilon_{\mathrm{cut}}}\right) \tag{4.11}$$

where N, Γ, and $\varepsilon_{\mathrm{cut}}$ represent the normalization, the photon index and the cut-off energy, respectively. Five flares (small flare 9(b), 2011 April flare, 2013 March flare, 2013 October flare (a) and October flare (b)) show significant curvature ($-2\Delta L > 9$)[*10] and those results are listed in Table 4.5. Figures 4.17 and 4.18 represent the SED of the synchrotron component during the "small flares" state and

Table 4.5 Spectral fitting results of each flare

flare id	flare duration [day]	averaged energy flux [$\times 10^{-10}$ erg cm^{-2} s^{-1}]	photon index	cut-off energy [MeV]	$-2\Delta L$
small flare 1	3.5 ± 1.7	4.3 ± 0.6	4.0 ± 0.3	–	–
small flare 2	3.9 ± 1.4	5.6 ± 0.8	3.4 ± 0.3	–	–
small flare 3	2.4 ± 1.3	5.0 ± 1.0	3.4 ± 0.4	–	–
small flare 4	3.3 ± 1.1	7.1 ± 1.2	2.9 ± 0.2	–	–
small flare 5	2.2 ± 0.8	8.3 ± 1.2	3.3 ± 0.2	–	–
small flare 6	7.3 ± 4.4	4.3 ± 0.5	4.3 ± 0.4	–	–
small flare 8	2.9 ± 1.9	4.4 ± 0.8	4.1 ± 0.5	–	–
small flare 9 (a)	2.7 ± 0.9	10.9 ± 1.4	3.0 ± 0.2	–	–
small flare 9 (b)	1.7 ± 0.8	15.9 ± 4.1	2.3 ± 0.2	–	–
2009 Feb	3.0 ± 0.9	9.4 ± 1.1	3.8 ± 0.3	–	–
2010 Sep	2.6 ± 0.6	17.4 ± 3.0	2.4 ± 0.1	–	–
2011 Apr	2.2 ± 0.2	60.4 ± 3.8	2.37 ± 0.04	–	–
2012 July	3.6 ± 1.8	7.3 ± 1.1	2.9 ± 0.2	–	–
2013 Mar	6.0 ± 0.7	17.9 ± 0.7	3.2 ± 0.1	–	–
2013 Oct (a)	3.0 ± 0.6	12.0 ± 1.2	3.2 ± 0.2	–	–
2013 Oct (b)	1.6 ± 7.8	17.8 ± 2.3	3.0 ± 0.2	–	–
small flare 9 (b)	–	11.3 ± 1.8	0.3 ± 0.7	237 ± 94	14.9
2011 Apr	–	45.5 ± 1.8	1.6 ± 0.1	688 ± 115	71.2
2013 Mar	–	17.0 ± 0.6	2.2 ± 0.2	257 ± 67	20.5
2013 Oct (a)	–	11.4 ± 1.1	1.5 ± 0.7	160 ± 76	9.5
2013 Oct (b)	–	16.2 ± 1.9	0.6 ± 1.0	119 ± 57	10.1

The upper section represents the fitting results using a power-law model. The lower section shows the results using a power law with an exponential cut-off model for the flares in which significant cut-off ($-2\Delta L > 9$) was observed. ΔL represents the difference of the logarithm of the likelihood of the fit with respect to a single power-law fit.

[*10] $-2\Delta L = -2\log(L0/L1)$, where $L0$ and $L1$ are the maximum likelihood estimated for the null (a simple power-law model) and alternative (a power law with an exponential cut-off model) hypothesis, respectively.

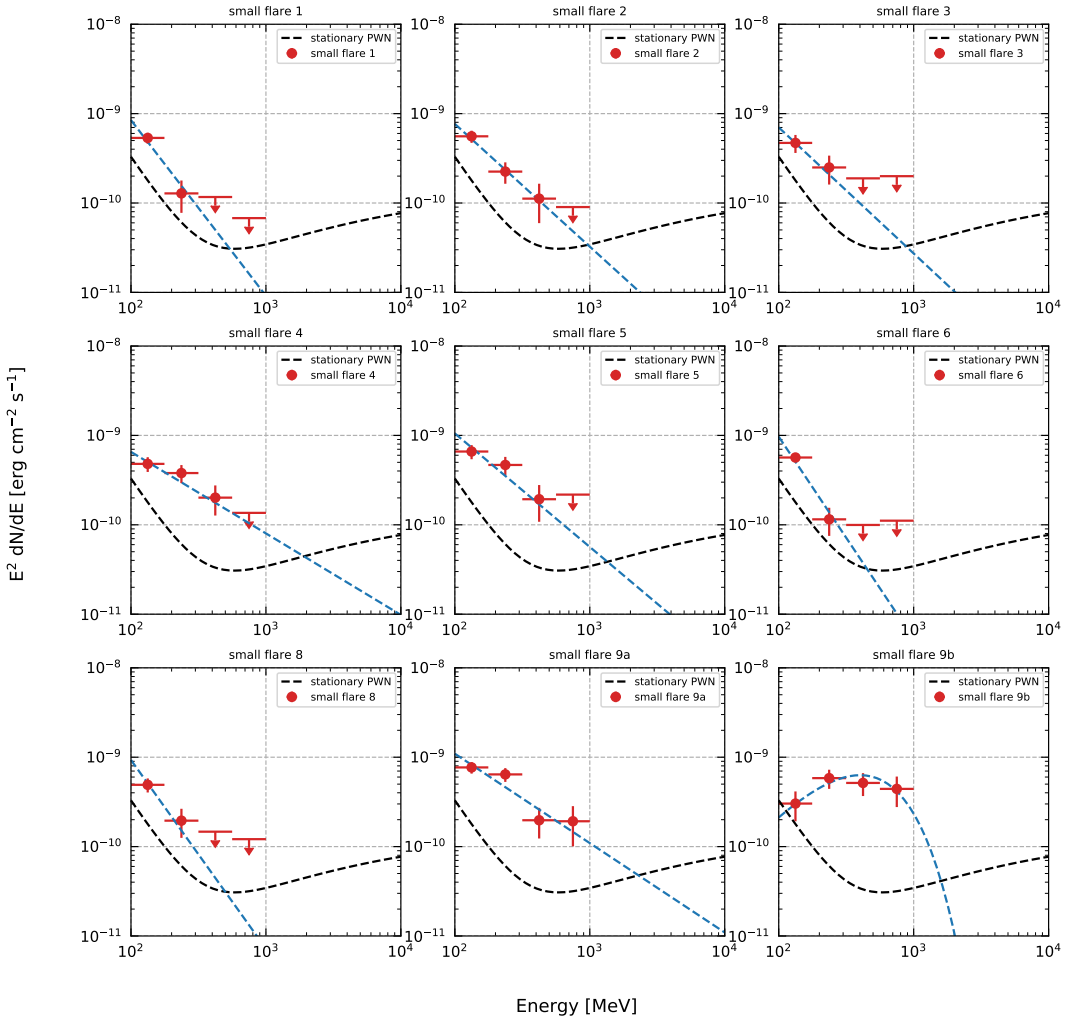

Figure 4.17 Spectral energy distribution for the Crab Nebula during each "small flare" state. The dashed black line represents the base-line result of the Crab Nebula described by Eq. (4.6) The dashed blue line shows the best-fitted model of the Crab synchrotron component during the "small flare" duration. The upper limits are set at a 95% confidence level.

"reported flares" state (see Table 4.4). The spectral points were obtained by dividing the 100 MeV and 1 GeV range into 4 logarithmically spaced energy bins. The blue dashed lines and black dashed line show the best fitted results and the base-line component of the Crab Nebula (the same as the black dashed line in Figure 4.10), respectively.

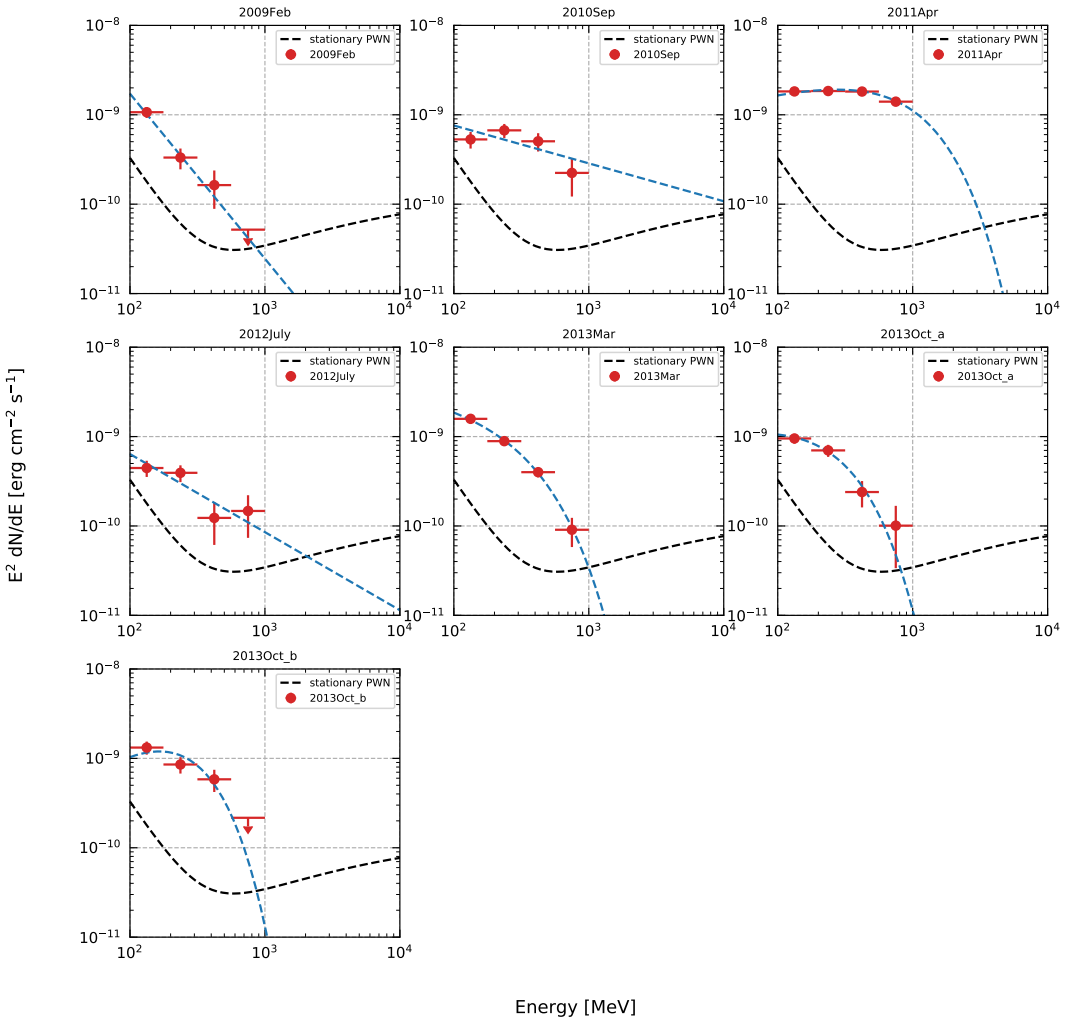

Figure 4.18 Spectral energy distribution for the Crab Nebula during each "reported flare" state. The dashed black line represents the base-line result of the Crab Nebula described by Eq. (4.6) The dashed blue line shows the best-fitted model of the Crab synchrotron component during the "reported flare" duration. The upper limits are set at a 95% confidence level.

4.2.4 Month Scale Variability

The Crab synchrotron emission in the gamma-ray band shows variability not only in a day scale but also in a month scale (Abdo et al., 2011). Off-pulse analysis of the Crab pulsar is necessary to investigate the month-scale variability because the variability amplitude is rather small and the variation can be hidden by the Crab pulsar emission. For studies of the month-scale variation of the Crab synchrotron emission, we made a 30-day binned gamma-ray flux LC of the Crab synchrotron component thorough off-pulse analysis. The 30-day binned LC between 54686 and 57349 represents in Figure 4.19. The upper panel is LC in unit of energy flux and the lower one represents photon indices. The analysis procedure is the same manner as the 5-day binned LC shown in Figure 4.12; the Crab Nebula is modeled by the Eq. (4.6) and the normalization, photon index ($N_{0,\mathrm{SYN}}$ and $\Gamma_{0,\mathrm{SYN}}$) of the Crab synchrotron component and the normalization of the isotropic diffuse emission set free and the other sources are fixed by the base-line values. In order to examine the variability of the synchrotron component, we performed the χ^2 test based on the Eq. (4.7). Data points of the gamma-ray fluxes and the photon indices which overlapped with any peaks of both the reported flares and "small flares" were excluded, because the fluxes of those points could be dominated by emission related to the day-scale flaring activities (red points in Figure 4.19). The obtained χ^2_{SYN}/ (d.o.f) are $\chi^2_{\mathrm{SYN,\,flux}} = 723.73/142$ for the fluxes and $\chi^2_{\mathrm{SYN,\,index}} = 137.22/142$ for the photon indices. This suggests the synchrotron flux except for the flare states is never stationary while the photon index is constant.

We divide the data set into five states base on the value of the fluxes: state 1 (the lowest flux group) to state 5 (the largest flux group) to investigate a possible relation between the gamma-ray fluxes and the photon indices in a more statistically stable state. The flux range is shown in Table 4.6 in each states. The scatter plot of the photon indices and the fluxes of the averaged values in each state is shown in Figure 4.21. We also added the fluxes and the photon indices from the 30-day binned light curve as the black points. There are hard $\Gamma = 4.03 \pm 0.07$ and bright flux state and soft $\Gamma = 4.95 \pm 0.26$ and weak flux state while there is no clear relation between the flux and the photon index in the intermediate state (state 2, 3, 4).

Table 4.6 List of flux range in each state

name	flux range [$\times 10^{-10}$ erg cm^{-2} s^{-1}]
state 1	0.36 – 0.86
state 2	0.90 –1.2
state 3	1.2 – 1.5
state 4	1.6 – 1.9
state 5	2.0 – 3.4

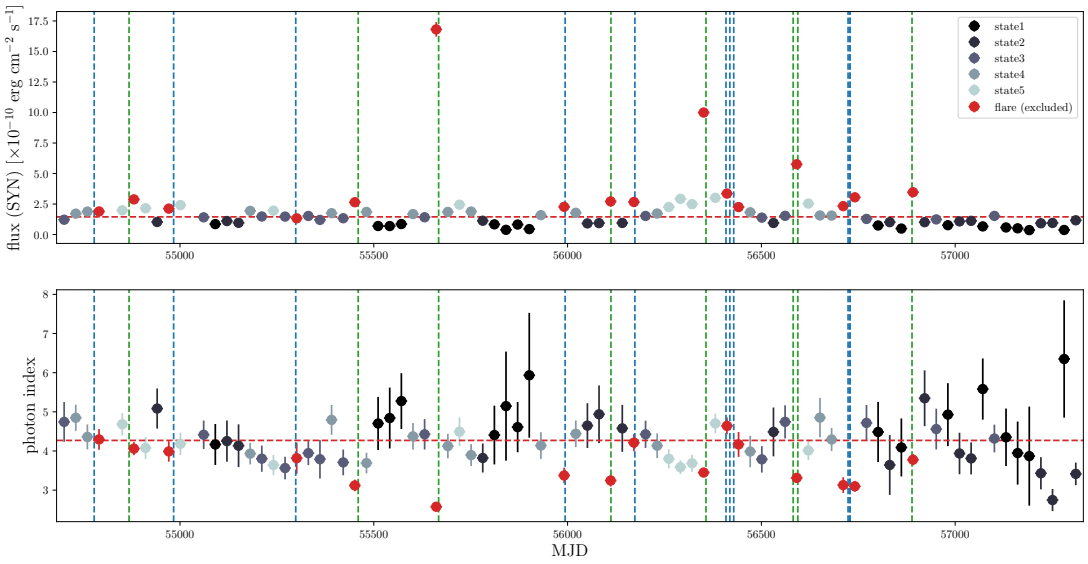

Figure 4.19 top: 30-day binned gamma-ray flux light curve (100 MeV - 500 GeV) of the Crab synchrotron component. bottom: The history of the photon index of the Crab synchrotron component between 100 MeV - 500 GeV. The “small flares" are presented in the blue lines, and the green lines show the “reported flares".

Month-Scale Variability vs. Hard X-ray

We found the Crab Nebula is not a “stationary” source in the month scale. There are no correlate activities with flares in other wave length observations at the present (see e.g. Bühler and Blandford, 2014). However, it is unclear whether there is a any correlation between the monthly gamma-ray variability and other wavelength phenomena. The recent X-ray observations revealed the Crab Nebula is not steady in X-ray and soft gamma-ray band (Wilson-Hodge et al., 2011; Kouzu et al., 2013). Here we attempt to compare the gamma-ray flux and other wave length observation.

At first, we compared the gamma-ray LC with the hard X-ray LC with measured by *Swift*/BAT. The LC is shown in Figure 4.21. The energy range of *Swift*/BAT data is 15–50 keV. In order to examine the correlation, we calculated the discrete correlation function (DCF) (Edelson and Krolik, 1988)[*13]. The DCF is defined for two individual data sets, $\{a_i,\ b_j\}$ and allows to quantify the correlation of the flux between the gamma-ray and other bands without any interpolation of the data sets. At first, unbinned

[*12] https://swift.gsfc.nasa.gov/results/transients

[*13] The pyDCF was used for the calculation https://github.com/astronomerdamo/pydcf (see also Robertson et al., 2015).

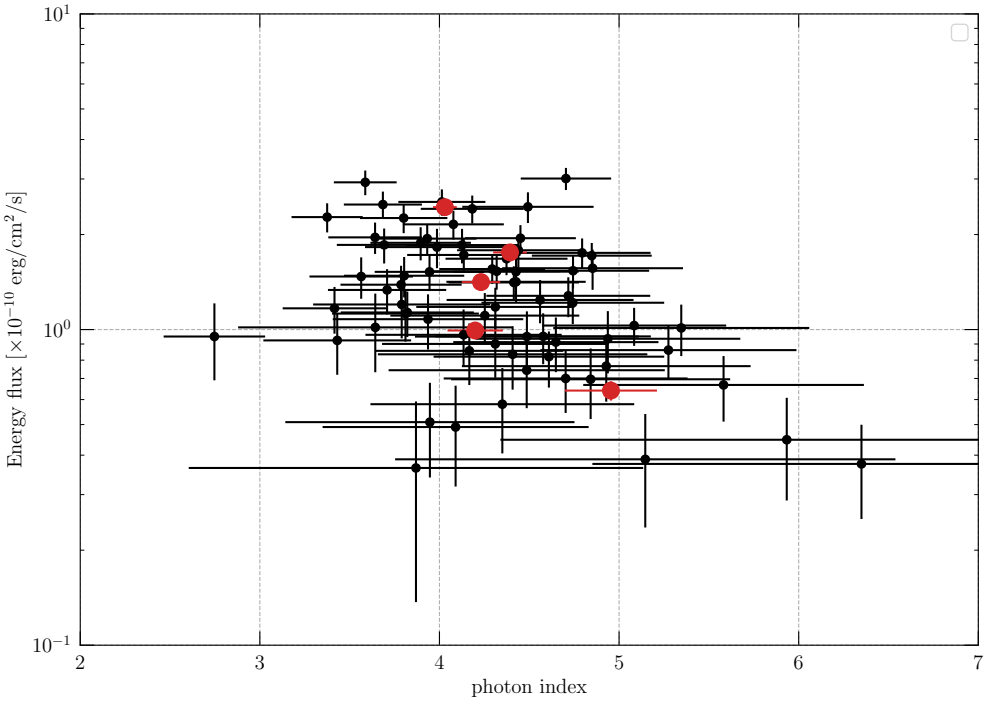

Figure 4.20 Scatter plot of the fluxes (100 MeV – 500GeV) and the photon indices of the Crab Nebula. The red points shows the data points sorted in flux resulting from 30-day binned analysis. The black points represents the results from 30-day binned analysis. Both "reported flares" and "small flares" are excluded.

discrete correlation coefficients (UDCF_{ij}) is defined by:

$$\mathrm{UDCF}_{ij} = \frac{(a_i - \bar{a})(b_j - \bar{b})}{\sqrt{(\sigma_a^2 - e_a^2)^2(\sigma_b^2 - e_b^2)^2}} \tag{4.12}$$

for all data sets. Here, $\{\bar{a}, \bar{b}\}$, $e_{a/b}$ and $\sigma_{a/b}$ represent the average value of the data sets, measurement errors with the data sets and the standard deviation with the data sets, respectively. Each of these correlation is related with the pairwise time lag, $t_{ij} = t_j - t_i$. The UDCF_{ij} is summed inside the time lag bin, $\tau - \frac{\Delta\tau}{2} \leq t_{ij} \leq \tau + \frac{\Delta\tau}{2}$ where τ is the transform in time and $\Delta\tau$ is the bin width. The $\mathrm{DCF}(\tau)$ can be obtained by the averaging the summed UDCF_{ij} with M data sets for $\tau - \frac{\Delta\tau}{2} \leq t_{ij} \leq \tau + \frac{\Delta\tau}{2}$:

$$\mathrm{DCF}(\tau) = \frac{1}{M} \sum \mathrm{UDCF}_{ij} \,. \tag{4.13}$$

The error is calculated by

$$\sigma_{\mathrm{DCF}}(\tau) = \frac{1}{M-1} \sqrt{\sum (\mathrm{UDCF}_{ij} - \mathrm{DCF}(\tau))^2} \,. \tag{4.14}$$

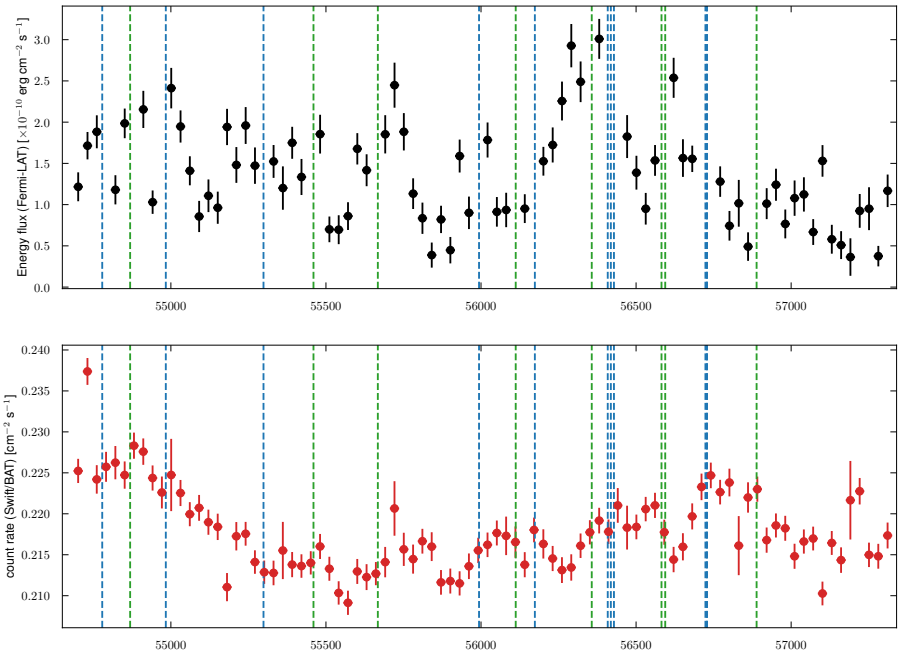

Figure 4.21 30-day binned light curve of the gamma-ray and X-ray. top: Gamma-ray energy flux in energy range 100 MeV – 500 GeV from *Fermi*-LAT. Both reported flares and "small flares" are excluded. bottom: X-ray count rate in energy range 15 – 50 keV from *Swift*/BAT. The dashed blue lines and the dashed green lines represent the time of "small flare" and reported flare, respectively. The *Swift* data is taken its archival data [*12].

The choice of the $\Delta\tau$ is not decided by apriori. Generally, the larger $\Delta\tau$ improve the accuracy in the statistical measurement while the small $\Delta\tau$ gives a good resolution of the DCF curve. Note that Edelson and Krolik (1988) argued that the choice of the bin width does not strongly affect the result. We calculated the DCF between the 30 day-binned gamma-ray flux and the 30-day binned *Swift* data and the result is shown in Figure 4.22. The DCF does not show a strong correlation in any time lags.

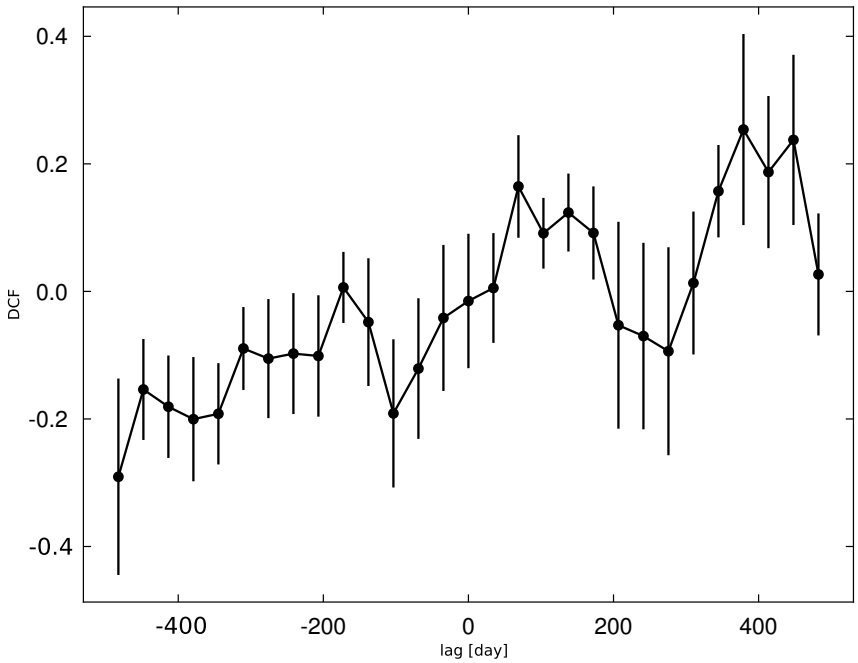

Figure 4.22 Discrete correlation function obtained for the gamma-ray and X-ray. Positive values of the lag correspond to flux in the gamma-ray band lagging flux in the X-ray band.

Month-Scale Variability vs. the Inner Knot

We compare the 30-day binned LC with the separation distance between the Crab pulsar and inner knot (knot-pulsar separation) observed by *Hubble Space Telescope* (HST) (Rudy et al., 2015)[*14] because one of the most prominent variable features in Crab Nebula is the inner knot which discovered by Hester et al. (1995). The 30-day binned LC between MJD 55796 and 57206 represents in Figure 4.23 (black points and left axis). We excluded data points of the gamma-ray fluxes which overlapped with any peaks of the flares because the fluxes of those points could be dominated by emission related to the day-scale flaring activities. Data points are interpolated by a cubic spline interpolation (black solid line). Note that this procedure brings some arbitrariness originated from the definition of flares.

The knot-pulsar separation is shown in Figure 4.23 as red points and the right axis. The "inner knot" locates about 0.55–0.75 arcsec to the south east from the Crab pulsar. This structure is interpreted as a Doppler-boosted emission from the downstream of the oblique termination shock and the bulk of the synchrotron gamma rays originates from the inner knot based on the MHD simulation (Komis-

[*14] We choose the Hubble Space Telescope data because the Keck data may have unaccounted systematic errors (Rudy et al., 2015).

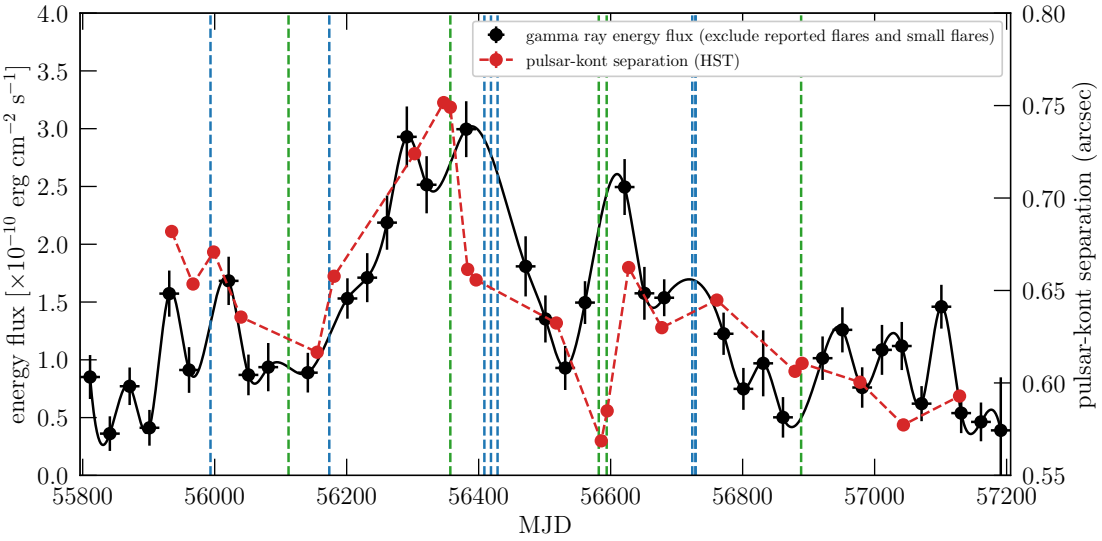

Figure 4.23 30-day binned gamma-ray flux light curve (100 MeV - 500 GeV) of the Crab synchrotron component and the separation distance between the Crab pulsar and the inner knot. Black data points represent the gamma-ray energy fluxes. The data points overlapping with any peaks of the flares are excluded. The points are interpolated using a cubic spline interpolation as plotted in the solid black line. Red data points show the separation distances between the Crab pulsar and the inner knot measured by the Hubble Space Telescope (Rudy et al., 2015). The small flares are presented in the blue lines, and the green lines show the reported flares.

sarov and Lyutikov, 2011). Rudy et al. (2015) compared between gamma-ray flux and the knot-pulsar separation, and no significant correlation was found between them. However, their gamma-ray data analysis was based on all-phase interval data and it was difficult to measure weaker fluxes of the Crab Nebula compared to fluxes of the Crab pulsar. Figure 4.24 shows a scatter plot between the knot separations from the HST observations and the corresponding gamma-ray energy fluxes based on the 30-day binned LC of Figure 4.23. Since Figure 4.23 does not include the data points of the gamma-ray fluxes which overlapped with any peaks of the day-scale flares, such data are not plotted in Figure 4.24, either. It seems that the gamma-ray fluxes become higher when the knot separation is larger. We calculated the Pearson correlation coefficient, r between the gamma-ray fluxes and the separation distance. As a result, we obtained $r = 0.70$ with p-value 5.4×10^{-3} and this implies the presence of a correlation. Our discovery provides the first possible correlation of the gamma-ray and any features revealed by high resolution telescope. One difficultly of the origin of the gamma-ray emission in the Crab Nebula is the worse angular resolution of the gamma-ray telescopes. This correlation is of great help to understand the particle acceleration site emitting the gamma-ray synchrotron in the Crab Nebula. However, there are some biases for the selection of the gamma-ray data points. In addition, the observation of

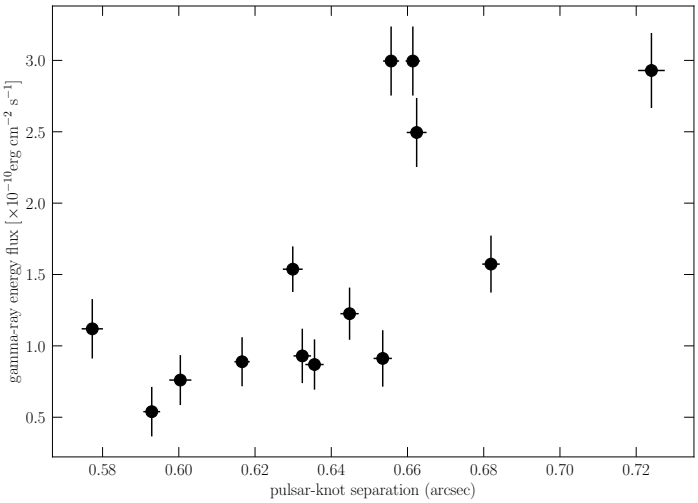

Figure 4.24 Scatter plot of the gamma-ray energy flux (100 MeV – 500 GeV) and the knot-pulsar separation. The gamma-ray fluxes were averaged with a 30-day bin and the knot-pulsar separation was observed by HST within each 30-day bin. With the same definition of the 30-day LC in Figure 4.23, the data points overlapping with any peaks of the flares are excluded, and the data of the knot-pulsar separation is taken from Rudy et al. (2015).

the inner knot is relatively sparse to trace various time scale of the gamma-ray flux, therefore more evenly sampled observations by optical telescopes are necessary to establish the correlation between the gamma-ray flux and the knot-pulsar separation.

Chapter 5

Discussion on the Time Variability and the Origin of the Multi MeV Synchrotron Gamma-ray Emission in the Crab Nebula

There are two electron populations which are produce $\sim$ 100 MeV synchrotron gamma-ray radiation. One is called "wind electrons", which are responsible for the bulk non-thermal radiation in X-ray and TeV gamma-ray band. The "wind electrons" are canonically assumed to extend upto $\sim$ 1 PeV (e.g. Atoyan and Aharonian, 1996), and emit $\sim$ 100 MeV synchrotron gamma-ray photons. The other is characterized by a hard spectrum with the cut-off emission of those particles is observed as large-intensity flares (Buehler et al., 2012; Mayer et al., 2013). The magnetic reconnection framework is the most feasible scenario to explain these flares.

At first, we attempt to discuss the flare statistics. We apply the magnetic reconnection framework to the flares with the cut-off spectra. For the other flares, we examine whether "wind electrons" describe the relation between the energy fluxes and the photon indices. Then, we try to characterize the physical environment of the "small flares" based on the observed time variabilities to investigate the difference between the "small flares" and the "reported flares". For the month-scale variability, we discuss whether the "wind electron" can explain the observed fluxes and photon indices and provide a possibility of the relation between the gamma-ray fluxes and the pulsar-inner knot separation. Finally, we propose a new picture for the origin of the multi MeV synchrotron gamma-ray based on the studies in this thesis.

5.1 The Origin of the Small Flares

5.1.1 Flare Statistics

In Section 4.2.3, we obtained the fluences, characteristic time scales, and photon indices for all flares, including both the "reported flares" and the "small flares". The total number of flares amounts to fourteen thanks to the detections of the "small flares". The relatively large number of detections allows one to attempt discussing the features of the flares on a statistical bases.

As seen in Figure 4.17-(b), many of "small flares" have fluences smaller than 2×10^{-4} erg cm^{-2}. It suggests that even smaller intensity flares may exist although it is difficult to detect such flares with the current instrument. Superposition of unresolved weak flares may contribute to the variable LC which is seen in Figure 4.12. Because of the fast variability the flares should be produced through the synchrotron channel and only electrons with the highest attainable energy may provide a significant contribution in the GeV energy band. If the spectral analysis of the flare allows one to define the cut-off energy, one can use the single particle spectrum to define the energy of the emitting particles, E. The single-particle synchrotron spectrum is described by the following approximate expression:

$$F_{\rm sp}(\varepsilon) \propto \left(\frac{\varepsilon}{\varepsilon_c}\right)^{1/3} \exp\left(-\frac{\varepsilon}{\varepsilon_c}\right). \tag{5.1}$$

The critical energy is defined as $\varepsilon_c \equiv \frac{3\hbar E^2 eB}{2m_e^3 c^5}$, where E, ε, e, m_e, c, and B are electron energy, photon energy, the elementary charge, the electron mass, the speed of light, and the magnetic field strength (Rybicki and Lightman, 1979).

Detection of a cut-off in the LAT band implies that emitting particles are accelerated by some very efficient radiation mechanism or produced in relativistically moving plasma. Presently, it is broadly accepted that the magnetic field reconnection scenario provides the most comprehensive approach for the interpretation of the flaring emission (see, e.g., Cerutti et al., 2012; Bühler and Blandford, 2014). These models allow one to reproduce some important properties of individual flares successfully, however do not attempt to study the flare statistics. We, therefore, present here some basic estimates aiming to describe the flare statistics in the frameworks of the reconnection scenario (see Lyubarsky, 2005, for a more detailed consideration). We assume that the reconnection proceeds in the relativistic regime, and we note that we ignore some processes, e.g., for the impact of the guiding magnetic field[*1], which potentially might be very important. However, a detailed consideration of the magnetic reconnection is beyond the scope of this paper.

If one assumes the flares originate from magnetic reconnection events, then some key aspects of the flare emission are determined by the geometry of the reconnection region. The schematic view of the

[*1] the magnetic filed along with the electric field (z-direction in Figure 5.2)

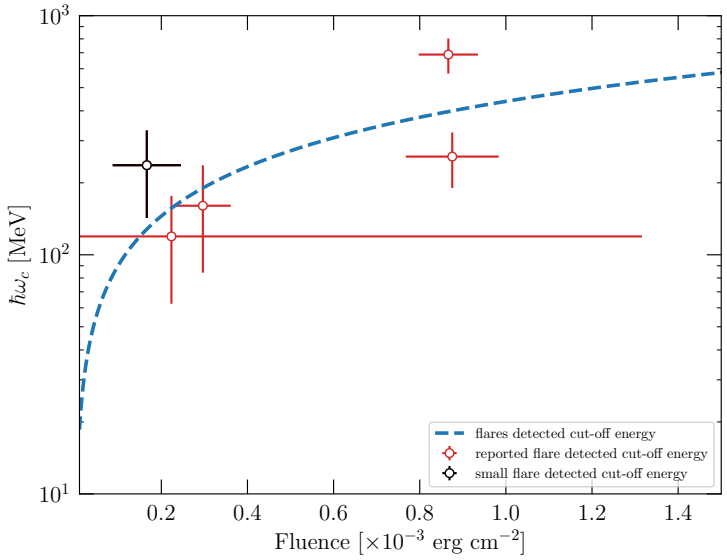

Figure 5.1 Scatter plot of the fluence and the cut-off energy for each flare in which significant spectral cut off was observed. Black data point indicates small flares 9 (b) and red points show 2011 April flare, 2013 March flare, 2013 October flare (a) and October flare (b). The critical synchrotron energy (ε_c) is defined by the observed cut-off energy. The dashed blue line shows the best fitted power-law function for those data points.

magnetic reconnection in this section is shown in Figure 5.2. The maximum energy that an electron can gain in the reconnection region can be estimated as

$$E_{\rm max} = eB_0L\,. \tag{5.2}$$

Here B_0 and L are the strength of the reconnecting magnetic field and the length of the layer, respectively. It was assumed here that the reconnection proceeds in the relativistic regime, i.e., the electric field at the reconnection region is equal to the initial magnetic field (see, e.g., Lyubarsky, 2005, for a general consideration of relativistic reconnection). The length of the reconnection region, L, determines the flare rise time, $\tau_{\rm rise} \simeq L/c$. The total magnetic energy, which is dissipated in the region, is given by

$$W_B = \frac{cB_0^2}{4\pi} aL\frac{L}{c} = \frac{a_L L^3 B_0^2}{4\pi}\,, \tag{5.3}$$

where $a = a_L L$ represent the width of the reconnection region (i.e., its length in the direction perpendicular to the electric field). The emission produced by particles accelerated beyond the ideal MHD limit might be highly anisotropic (Derishev et al., 2007; Cerutti et al., 2012), as electrons may lose energy over just a fraction of the gyro radius and photons are emitted within a narrow beaming cone. The beaming solid angle is determined by the $\Delta\Omega = \min[\pi(ct_{\rm SYN}/r_{\rm g})^2, 4\pi]$, where $t_{\rm SYN} \propto E^{-1}B^{-2}$ is

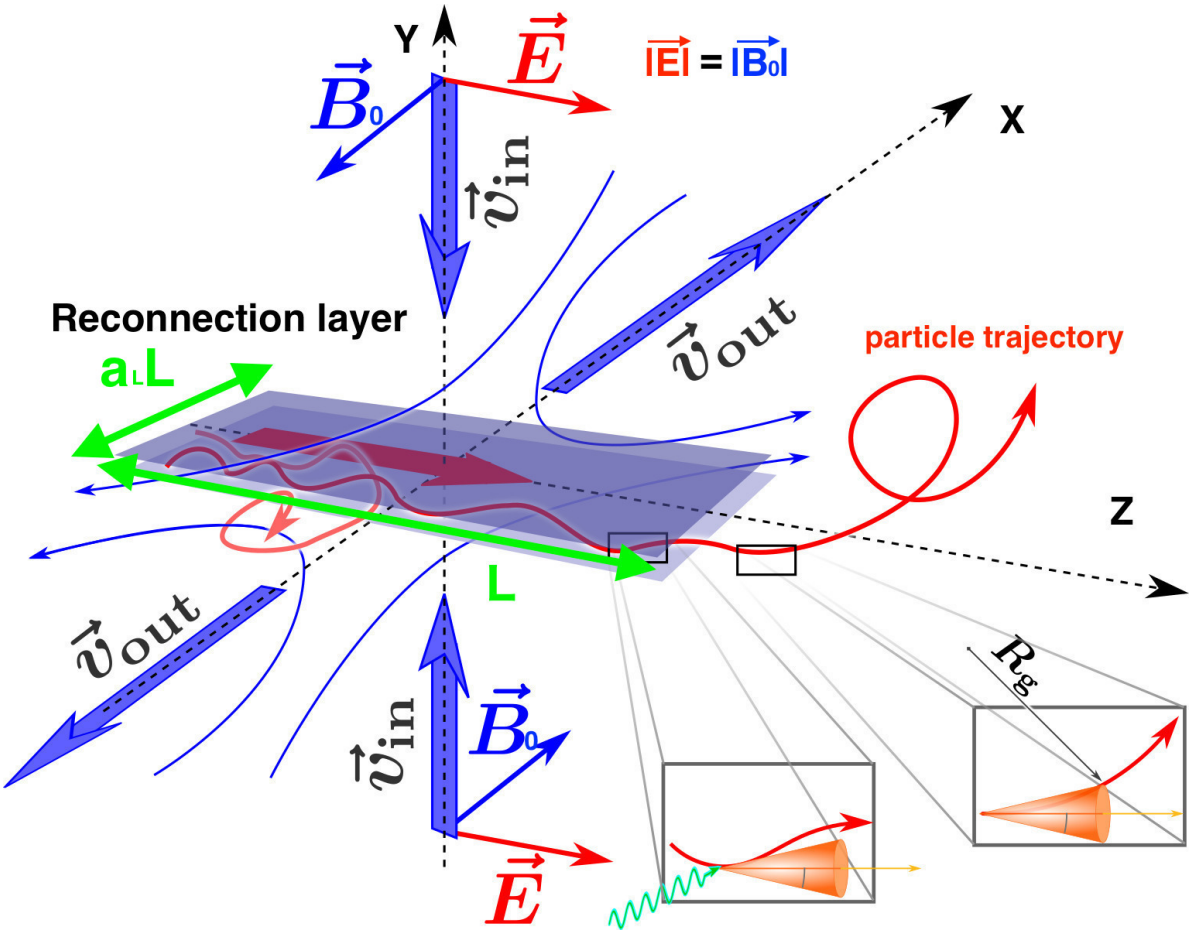

Figure 5.2 The schematic view of the magnetic reconnection. The incoming Poynting flux is dissipated in the reconnection layer, whose area is defined by $L \times a_L L$. Electrons injected into the reconnection layer are accelerated by the electric field induced in the layer. Since the electric field at the reconnection region is equal to the initial magnetic field, B_0 in the relativistic regime (see, e.g., Lyubarsky, 2005), the maximum electron energy is determined by the length of the reconnection layer, L, and the initial magnetic field. If the synchrotron loss time scale of the accelerated electron is shorter than the gyro period, the beaming effect is significant. (Credit: Dmitry Khangulyan, with modifications by the author.)

the synchrotron cooling time and $r_g \propto EB^{-1}$ is the gyro radius of the electron. The two values of the solid angle describe to two distinct regimes: $\Delta\Omega = \pi(ct_{\rm SYN}/r_g)^2$ corresponds to the strong beaming case whereas $\Delta\Omega = 4\pi$ represents the isotropic radiation case.

The observed fluences can be written as $F = \xi W_B / \left(D^2 \Delta\Omega\right)$, which yields

$$F_{\rm beaming} \propto B_0^{-5/2} \varepsilon_c^{7/2} \tag{5.4}$$

for the strong beaming case and

$$F_{\rm iso} \propto B_0^{-5/2} \varepsilon_c^{3/2} \tag{5.5}$$

for the isotropic case. Here ξ and D represent the radiation efficiency and the distance to the Crab Nebula, respectively. ξ represents a fraction of available energy that is transferred to the particles that produce the flare and must be less than unity. Generally, the magnetic field carries a significant part of energy because of the presence of the guide magnetic field, so one can expect $\xi \sim 1$–10%. The scatter plot of the fluence $F_{\rm SYN}$ and the critical photon frequency is shown in Figure 5.1. The dependence between these quantities was fitted with a power-law function:

$$\varepsilon_c \propto F_{\rm SYN}^{p} \,. \tag{5.6}$$

We include here only the flares that allow the detections of the cut-off energies (i.e., small flare 9 (b), 2011 April flare, 2013 March flare, 2013 October flare (a) and October flare (b)). For these data points we obtained $p = 0.69 \pm 0.35$ as the best-fit values. The line corresponding to the best-fit approximation is shown in Figure 5.1 as blue dashed line.

The dependence of the fluence on the critical synchrotron energy for the anisotropic regime, $p = 0.286$, does not seem to agree with the revealed best-fit approximation. However, the isotropic regime, $p = 0.66$, might be consistent with the dependence, although we note that the error bars are significant. This might be taken as a hint for the reconnection origin of the variable emission, but more detailed consideration makes this possibility to be less feasible. Namely, Eq. (5.5) allows one to obtain estimates for the strength of the magnetic field as

$$B_{\rm iso} \simeq 400\, a_L^{\frac{2}{5}} \xi^{\frac{2}{5}} \left(\frac{D}{2\ {\rm kpc}}\right)^{-\frac{4}{5}} \left(\frac{\varepsilon_{\rm c}}{300\ {\rm MeV}}\right)^{\frac{3}{5}} \left(\frac{F_{\rm SYN}}{6\times 10^{-4}\ {\rm erg\ cm^{-2}}}\right)^{-\frac{2}{5}} \mu{\rm G}\,, \tag{5.7}$$

As it is shown below, the detected rise and decay time scales require a significantly stronger magnetic field. This discrepancy implies that the magnetic field reconnection cannot be readily taken as the ultimate explanation for the origin of the variable GeV emission detected from the Crab Nebula, suggesting that other phenomena, e.g., Doppler boosting plays important role (see, e.g., Buehler et al., 2012).

Reconstruction of the spectrum of emitting particles for the flares that do not allow defining the cut-off energy is less straight forward. Let us assume that the electron spectrum is described by a power-law with an exponential cut-off: $\frac{dN}{dE} \propto E^{-\alpha}\exp\left(-E/E_{\rm max}\right)$. The modeling of the emission from the Crab Nebula implies that the high energy part of the electron spectrum is characterized by $\alpha \simeq 3.23$ and the cut-off energy is in the PeV band $E_{\rm max} \simeq 3\,{\rm PeV}$ (as obtained by Meyer et al., 2010, in the framework of the constant B-field model). The total synchrotron spectrum is then

$$F(\varepsilon) \propto \int dE' E'^{-\alpha} \exp\left(-E'/E_{\rm max}\right) \left(\frac{\varepsilon}{\varepsilon_c}\right)^{1/3} \exp\left(-\frac{\varepsilon}{\varepsilon_c}\right). \tag{5.8}$$

For the spectra, which do not allow determination of the cut-off frequency, one should expect $\varepsilon_c(E_{\rm max}) \lesssim 100\,{\rm MeV}$ or $\varepsilon_c(E_{\rm max}) \gg 100\,{\rm MeV}$, the later possibility is however robustly excluded by

the synchrotron radiation theory and the broadband spectrum measured with *Fermi*–LAT [*2]. In the regime $\varepsilon \geq \varepsilon_c(E_{\rm max})$, the above integral can be computed with the *steepest descent* method yielding in

$$F(\varepsilon) \propto E_{\rm max}^{-\alpha+1} \left(\frac{\varepsilon}{\varepsilon_c(E_{\rm max})}\right)^{-\frac{6\alpha-5}{18}} \exp\left(-\frac{3}{2^{2/3}}\left(\frac{\varepsilon}{\varepsilon_c(E_{\rm max})}\right)^{1/3}\right), \tag{5.9}$$

where the dependence on $E_{\rm max}$ and B is kept. The photon index at ε can be obtained as

$$\Gamma_{\rm SYN} \simeq 1 - \frac{\frac{dF(\varepsilon/\varepsilon_c(E_{\rm max}))}{d\varepsilon}}{F(\varepsilon/\varepsilon_c(E_{\rm max}))}\varepsilon, \tag{5.10}$$

which can be derived analytically:

$$\Gamma_{\rm SYN} = \frac{6\alpha+13}{18} + \frac{1}{2^{2/3}}\left(\frac{\varepsilon}{\varepsilon_c(E_{\rm max})}\right)^{1/3}. \tag{5.11}$$

The variable gamma-ray emission might originate from the distribution of non-thermal electrons that are responsible for the broad-band emission from the Crab Nebula. For example if the strength of the magnetic field fluctuates or the electron cut-off energy changes. To probe these possibility we set $\alpha = 3.23$, and study the relation between the flare flux and photon index. If the variation is caused by a change of the magnetic field (i.e., $E_{\rm max} = {\rm const}$), then

$$F(\varepsilon) \propto (\Gamma_{\rm SYN} - 1.8)^{-2.4} \exp\left(-3\,(\Gamma_{\rm SYN} - 1.8)\right). \tag{5.12}$$

If the variability of the gamma-ray emission is caused by a change of the electron cut-off energy, then there is an addition factor in the expression that determines the flux level:

$$F(\varepsilon) \propto (\Gamma_{\rm SYN} - 1.8)^{0.95} \exp\left(-3\,(\Gamma_{\rm SYN} - 1.8)\right). \tag{5.13}$$

The scatter plot of the both "small flares" flux and reported flares flux without detection of the curvature structure and photon index is shown in Figure 5.3. From the figure it can be seen that the data points seem to be inconsistent with Eq. (5.12), which corresponds to the case when the flare is generated by a changing magnetic field. Although Eq. (5.13) agrees better with the data, the discrepancy is still large. This suggests that one-zone model does not allow one to study the seen variability, and a more detailed model is required. In particular, the properties at the flare production site might be different from the typical conditions inferred for the nebula, implying a realization of a multi-zone configuration. In what follows we try to infer the conditions at the flare production site using simple synchrotron models for individual "small flares".

5.1.2 Magnetic Field Strength at the Emission Site

All "small flares" except for one episode allow defining the rise and decay time-scales based on 1.5-day binned light curves. Here, we discuss constrains on the magnetic field strength assuming

[*2] The observed cut-off energy between *COMPTEL* and *Fermi*–LAT band was 97 ± 12 MeV (Abdo et al., 2010a)

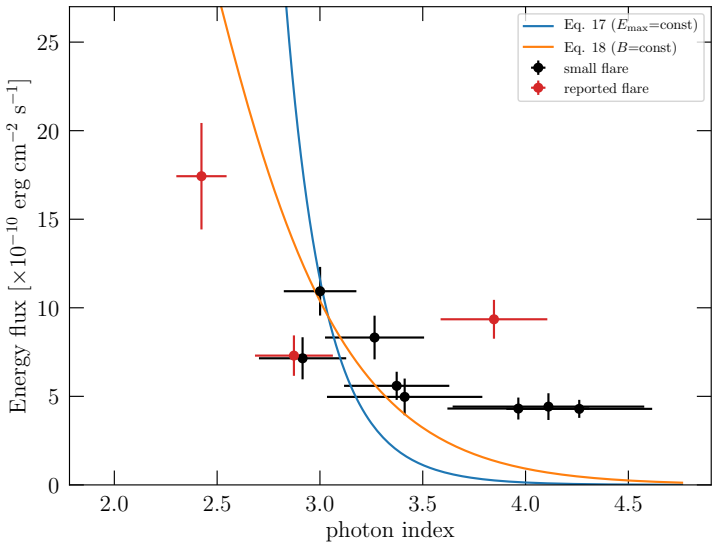

Figure 5.3 Scatter plot of the energy flux and the photon index for the flares that resulted in non-detection of the cut-off energy. Red points: reported flares. Black points: small flares. Two lines show the best fit approximation of the data points by Eq. (5.12) ($E_{\rm max}$ =const.: blue line) and Eq. (5.13) (B =const: orange line).

the synchrotron origin of the emission. For the sake of simplicity we adopt a model that assumes a homogeneous magnetic field in the flare production site, which does not move relativistically with respect to the observer. Thus the rise time is associated with particle acceleration time-scale:

$$t_{\rm acc} \simeq 10\eta \left(\frac{E}{1\,{\rm PeV}}\right)\left(\frac{B}{100\,\mu{\rm G}}\right)^{-1} {\rm d}\,, \tag{5.14}$$

where η, E and B are acceleration efficiency ($\eta \to 1$ for particle acceleration by reconnection), electron energy and magnetic field strength, respectively. Since variability is registered for $\sim$ 100 MeV emission, then one obtains

$$E \simeq 4\left(\frac{B}{100\,\mu{\rm G}}\right)^{-1/2}\left(\frac{\varepsilon}{100\,{\rm MeV}}\right)^{1/2} {\rm PeV}\,, \tag{5.15}$$

where ε is synchrotron photon energy. This yields an acceleration time of

$$t_{\rm acc} \simeq 40\eta \left(\frac{B}{100\,\mu{\rm G}}\right)^{-3/2}\left(\frac{\varepsilon}{100\,{\rm MeV}}\right)^{1/2} {\rm d}\,, \tag{5.16}$$

which translates to the following limitation on the magnetic field strength:

$$B \simeq 1\eta^{2/3}\left(\frac{t_{\rm acc}}{1\,{\rm d}}\right)^{-2/3}\left(\frac{\varepsilon}{100\,{\rm MeV}}\right)^{1/3} {\rm mG}\,. \tag{5.17}$$

Observational requirement of $\tau_{\rm acc} \approx 1$ d implies an extremely strong magnetic field or an acceleration with efficiency exceeding the ideal MHD limit: $\eta < 1$. We note however, that the cooling time, which is associated with the decay time (≈ 2 d), does not depend on the acceleration efficiency. The cooling time for the synchrotron emission is determined by

$$t_{\rm SYN} = 100 \left(\frac{\varepsilon}{100\ {\rm MeV}}\right)^{-1/2} \left(\frac{B}{1\ {\rm mG}}\right)^{-3/2} {\rm d}\,. \tag{5.18}$$

Eqs. (5.16) and (5.18) allow us to obtain the following constraint for the magnetic field

$$B \simeq 1 \left(\frac{t_{\rm SYN}}{2\,{\rm d}}\right)^{-2/3} \left(\frac{\varepsilon}{100\,{\rm MeV}}\right)^{-1/3} {\rm mG}\,. \tag{5.19}$$

This estimate is valid for the isotropic radiation regime, which, in particular, implies negligible Doppler boosting and homogeneity of the magnetic field. These assumptions are most likely violated for the big flares (see, e.g., Buehler et al., 2012). We nevertheless adopt these assumptions here as we aim testing the consistency of the "small flares" with these assumption *ex adverso*.

Given that (i) both the rise and decay time-scales are short, (ii) the dependence on the photon energy in Eqs. (5.17) and (5.19) is inverse, the magnetic field in the production region needs to be very strong, approaching the mG value. This estimate seems to be inconsistent with Eq. (5.7), posing certain difficulties for the reconnection scenario.

In PWN magnetic field can provide an important contribution to the local pressure:

$$P_{\rm B} = \frac{B^2}{8\pi} = 4 \times 10^{-10} \left(\frac{B}{100\ \mu{\rm G}}\right)^2 {\rm erg\,cm^{-3}}\,. \tag{5.20}$$

On the other hand, PWNe are expected to be nearly isobaric systems, thus the characteristic pressure in the Crab Nebula can be determined by the location of the pulsar wind termination shock:

$$P_{\rm PWN} \simeq \frac{2}{3} \times \frac{L_{\rm SD}}{4\pi R_{\rm TS}^2 c} \simeq 5 \times 10^{-9} \left(\frac{L_{\rm SD}}{5 \times 10^{38}\ {\rm erg\ s^{-1}}}\right) \left(\frac{R_{\rm TS}}{0.14\ {\rm pc}}\right)^{-2} {\rm erg\,cm^{-3}}\,, \tag{5.21}$$

where $L_{\rm SD}$ and $R_{\rm TS}$ are spindown luminosity of the central pulsar and the location of the termination shock, respectively. Such total pressure implies the magnetic field of $B \lesssim 400\ \mu$G, which appears to be significantly weaker than the strength required for acceleration and cooling of the particles responsible for the "small flares."

This implies that the production of small flares under conditions typical for the nebula is difficult. One of the common approaches to relax the constraints imposed by the fast variability is to involve a relativistically moving production site (Komissarov and Lyutikov, 2011; Lyutikov et al., 2016). Namely, the apparent variability time-scales are shorted:

$$t = \frac{t'}{\delta}\,, \tag{5.22}$$

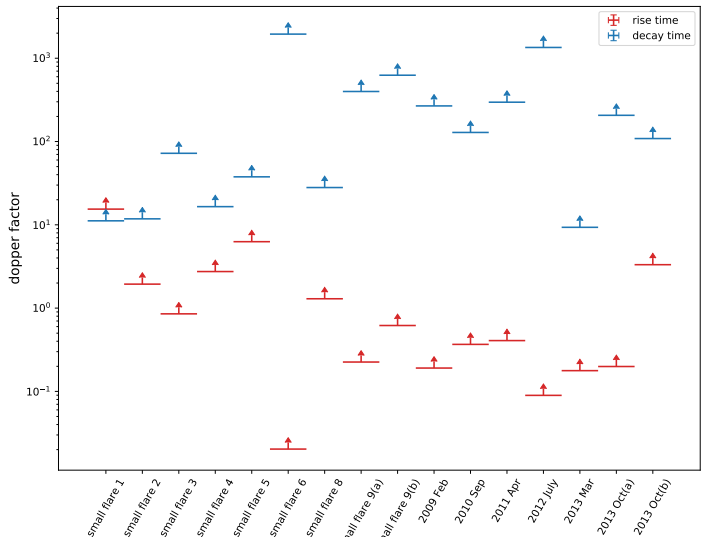

Figure 5.4 Doppler factor of each flare. The values are derived from Eq. (5.23) (red lower limits) and (5.24 (blue lower limits))

where t' is plasma co-moving frame time scales. In addition the emission frequency changes as well, so the co-moving frame photon energy is $\varepsilon' = \varepsilon/\delta$. Thus, one obtains that the requirements for magnetic field strength, Eqs. (5.17) and (5.19) are relaxed by a factor δ and $\delta^{\frac{1}{3}}$, respectively.

The maximum magnetic field strength consistent with the nebular pressure, $B = 400\,\mu\mathrm{G}$, gives the following lower limit of the bulk Lorentz factors from Eqs. (5.17) and (5.19):

$$\delta > 3\eta^{2/3}\left(\frac{t_{\rm acc}}{1\,\mathrm{d}}\right)^{-2/3}\left(\frac{\varepsilon}{100\,\mathrm{MeV}}\right)^{1/3}\left(\frac{B}{400\,\mu\mathrm{G}}\right)^{-1} \tag{5.23}$$

$$\delta > 30\left(\frac{t_{\rm SYN}}{2\,\mathrm{d}}\right)^{-2}\left(\frac{\varepsilon}{100\,\mathrm{MeV}}\right)^{-1}\left(\frac{B}{400\,\mu\mathrm{G}}\right)^{-3}. \tag{5.24}$$

The resulting doppler factor of each flare is shown in Figure 5.4

The existence of such high bulk Lorentz factors in the termination shock downstream region seems to be challenging, but, probably, cannot be excluded from the first principles. For example, the bulk Lorentz factor of a weakly magnetized flow passing through an inclined relativistic shock depends only on the inclination angle α: $\gamma = 3/(\sqrt{8}\sin\alpha)$ (see, e.g., Bogovalov and Khangoulyan, 2002). Thus, the required bulk Lorentz factors, $\gamma \simeq 15$, can be achieved if the pulsar wind velocity makes an angle of $\alpha \sim 5^\circ$ with the termination shock (see Figure 5.5). We note, however, that detailed MHD simulations are required to verify feasibility of the production of the variable GeV emission in relativistically moving plasma. Such MHD simulations should allow one to obtain a realistic magnetic field and plasma internal energy in the flow that is formed at the inclined termination shock. These parameters

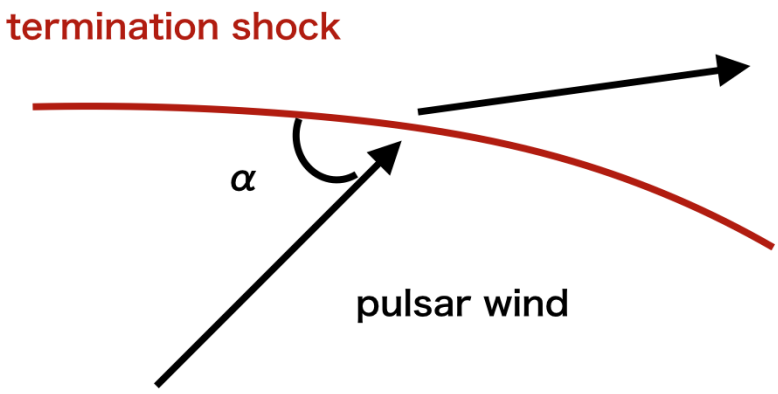

Figure 5.5 Schematic image of the termination shock and the inclination angle α.

are required to define the spectrum of non-thermal particles in the flow and in turn to compute the synchrotron radiation (Porth et al., 2014; Lyutikov et al., 2016).

5.2 The Origin of the Month Scale Variability

5.2.1 Testing the Possibility by the “Wind Electrons"

We could obtain the distribution of the gamma-ray flux and the photon index based on the 30-day binned analysis. This results indicates there is no clear correlation but the highest-flux state and the lowest-flux state has the different photon index: $\Gamma = 4.03 \pm 0.07$ for highest-flux state and $\Gamma = 4.95 \pm 0.26$ (see Figure 4.21). The question is that the flux-sorted distribution can be explained by the distribution of non-thermal electrons that are responsible for the broad-band emission. Here, we refer this non-thermal electron component as “wind electrons”. In order to verify this possibility, we apply the same method described in Section 5.1. The electron distribution is assumed to be a power-law with cut-off function (e.g. Atoyan and Aharonian, 1996; Mayer et al., 2013):

$$\frac{\mathrm{d}N}{\mathrm{d}E} \propto E^{-3.23} \exp\left(-\frac{E}{E_{\mathrm{cut}}}\right) \tag{5.25}$$

where E_{cut} represents the electron cut-off energy, $E_{\mathrm{cut}} \sim 1$ PeV. The radiation from the “wind electrons” corresponds to the bulk non-thermal emission above X-ray in the Crab Nebula. In this case, the asymptotic synchrotron spectrum can be written:

$$F(\varepsilon) \propto E_{\mathrm{max}}^{-\alpha+1} \left(\frac{\varepsilon}{\varepsilon_c(E_{\mathrm{max}})}\right)^{-\frac{6\alpha-5}{18}} \exp\left(-\frac{3}{2^{2/3}}\left(\frac{\varepsilon}{\varepsilon_c(E_{\mathrm{max}})}\right)^{1/3}\right), \tag{5.26}$$

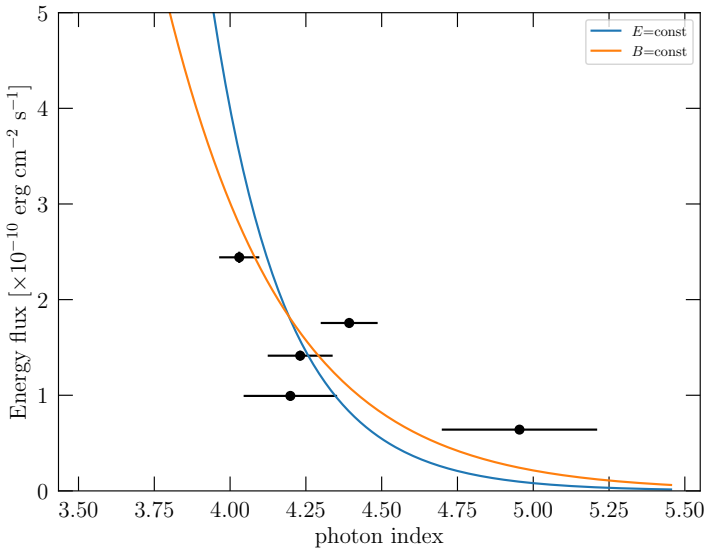

Figure 5.6 Scatter plot of the energy flux and the photon index for the flux-sorted results. Two lines show the best fit approximation of the data points by Eq. (5.29) ($E_{\rm max}$ =const.: blue line) and Eq. (5.30) (B =const: orange line).

where ε_c is the critical synchrotron frequency defined by $\varepsilon_c \equiv \frac{3\hbar E^2 eB}{2m_e^3 c^5}$, where E, e, m_e, c, and B are electron energy, the elementary charge, the electron mass, the speed of light, and the magnetic field strength (Rybicki and Lightman, 1979). The photon index at ε can be obtained as

$$\Gamma_{\rm SYN} \simeq 1 - \frac{\frac{dF(\varepsilon/\varepsilon_c(E_{\rm max}))}{d\varepsilon}}{F(\varepsilon/\varepsilon_c(E_{\rm max}))}\varepsilon\,. \tag{5.27}$$

This yields the following approximate relation between the photon index and the critical frequency:

$$\Gamma_{\rm SYN} = \frac{6\alpha + 13}{18} + \frac{1}{2^{2/3}}\left(\frac{\varepsilon}{\varepsilon_c(E_{\rm max})}\right)^{1/3}\,. \tag{5.28}$$

If the energy flux and photon index variation is caused by a fluctuation of the strength of the magnetic field, the relation between the flux and photon index is written by

$$F(\varepsilon) \propto (\Gamma_{\rm SYN} - 1.8)^{-2.4} \exp\left(-3\,(\Gamma_{\rm SYN} - 1.8)\right)\,. \tag{5.29}$$

If the variability of the gamma-ray emission is caused by a change of the electron cut-off energy, then there is an addition factor in the expression that determines the flux level:

$$F(\varepsilon) \propto (\Gamma_{\rm SYN} - 1.8)^{0.95} \exp\left(-3\,(\Gamma_{\rm SYN} - 1.8)\right)\,. \tag{5.30}$$

The fitting results are shown in Figure 5.6. The best-fitted lines provide a certain explanation of the distribution, however the discrepancy still remains for especially the softest component. This

discrepancy implies that the origin of $\sim$ 100 MeV gamma-rays is different from the "wind electrons" while more sophisticated models can not be excluded.

5.2.2 Correlation between the Gamma-ray Flux and the Separation Distance of the Inner Knot and the Crab Pulsar

In Section 4.2.4, we obtained a possible relation of the gamma-ray energy flux to the knot-pulsar separation. This tendency is, however, inconsistent with the prediction of the MHD model by Komissarov and Lyutikov (2011). On the other hand, we argued that the gamma-ray synchrotron originated from a region with a strong magnetic field, like the base of the jet, in Section 3.2.2 and 5.2.1. A possible scenario is that a perturbation of the termination shock affects the magnetic pressure at the base of the jet if the correlation is real. The knot-pulsar separation has a strong dependence on the shock geometry, because the inner knot is considered to be a result of the strong Doppler boosting at the downstream of the termination shock (e.g Lyutikov et al., 2016). In this case, one can expect a time lag between particle acceleration at the base of the jet and emitting gamma rays and the fluctuation of the shock geometry. However, we compared the month scale gamma-ray with relatively sparse optical observations therefore it is difficult to infer any time delay between the gamma-ray emission and the knot-pulsar separation in the current data set. The further observations are necessary not only to establish the correlation but also to test this possibility. In addition, higher-resolution MHD simulations are required to study how the magnetic pressure at the jet affects the termination shock geometry.

5.3 Origin of Multi MeV gamma ray

In this thesis, we study the origin of the PeV electrons in the Crab Nebula. There are two possible sites of the acceleration upto PeV: the termination shock and the base of the jet. The scenario that the electrons accelerated at the termination shock ("wind electrons") and advected with the MHD flow can reproduce both the spectrum and the extension of the UV, X-ray and TeV (H. E. S. S. Collaboration et al., 2019a), while the acceleration upto PeV at the termination shock is only an assumption. The base of the jet is the most feasible site of the flare production (e.g. Lyutikov et al., 2018a), because a strong magnetic field and a large magnetization parameter might be realized in there.

MeV and multi hundred TeV gamma rays allow one to estimate the strength of the magnetic field at the acceleration site. The resulting magnetic field is weak, 118 μG and this indicates a difficulty of the confinement of PeV electrons. A possible solution is multi MeV gamma-ray emission originates from a new electron component. We showed that the two-zone model ("wind electron" + Maxwellian-type distribution) can reproduce the MeV to TeV gamma-ray spectrum.

We could detect nine low-intensity flares ("small flares") which have not been reported in literature ("reported flares"). Production sites of all flares (both "reported flares" and "small flare") require strong

magnetic fields, $B \sim 1$ mG, because of their short time scales. This indicates that not only "reported flares" but also "small flares" originate from the non-ordinary environment which is not expected by the modeling of the non-thermal emission. Since the detection of flares is limited by the sensitivity of the current detectors, one can expect the existence of weaker flares. This implies that the contribution of flares might not be small to multi MeV gamma-ray spectrum. In addition, the month-scale gamma-ray variability does not correlate with the hard X-ray (15–50 keV), and also indicates another electron distribution which is different from "wind electrons". Interestingly, we found a possible correlation between the monthly gamma-ray flux and the pulsar-knot separation. If this feature is real, this is the first case of establishing a link between the gamma-ray flux level and some spatially resolved morphological feature seen in the Crab Nebula with some high resolution telescope. The current theoretical models and optical/near infrared observation suggest an anti-correlation. Therefore the inner knot itself seems to be less feasible for the gamma-ray emission site but the dynamics of the termination shock might affect the gamma-ray fluxes.

Our works presented in this thesis suggest that the bulk of multi MeV emission and flare emission have a common production site. The most feasible site is the base of jet where the MHD simulation suggests strong magnetic fields, $B \sim 1$ mG (Porth et al., 2014). Figure 5.7 represents the current understanding of the Crab Nebula with the results obtained in this thesis highlighted in red fonts. According to our scenario, the persistent electron acceleration at the jet is responsible for the bulk multi MeV gamma-ray emission and flares originate from a strong flux enhancement such as the beaming and/or Doppler boost effect. The possibility of the gamma-ray origin at the base of the jet was discussed by Lyubarsky (2012) from the theoretical point of view and the recent MHD simulations imply the requirement of an additional acceleration to explain the brightness of the jet (Porth et al., 2014). The existence of the new electron component can test by the feature TeV gamma-ray observatories and MeV missions.

Finally, the hard electron spectrum is required to explain the multi MeV gamma-ray emission (see Section 3). Such a hard electron spectrum was also found by the blazar 3C 279 flare (Hayashida et al., 2015). The understanding of the acceleration in the Crab Nebula may help to shed light on the acceleration in blazar jets which is another important issue in the high energy astrophysics.

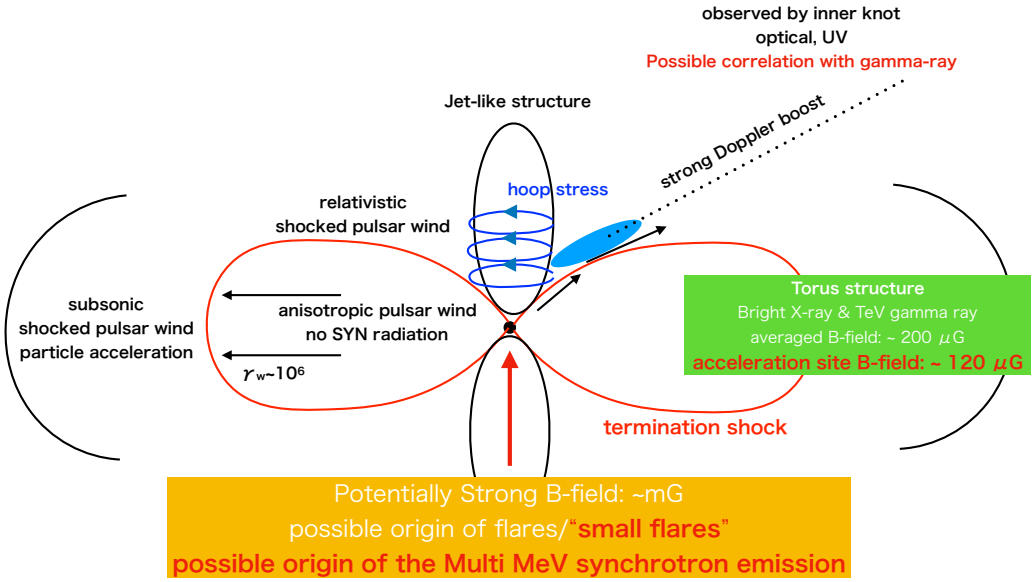

Figure 5.7 Crab Nebula with key hydrodynamic structures shown schematically. Locations and expected physical conditions are shown for the relevant production sites. Conditions revealed in this works are shown in red font. The oblique termination shock originated from the anisotropic pulsar wind naturally makes the torus structure observed in X-ray (e.g. Weisskopf et al., 2000; Bogovalov and Khangoulyan, 2002). Such anisotropic wind also makes a collimated jet flow due to the magnetic hoop stress in the polar region (e.g. Lyubarsky, 2002a; Bogovalov and Khangoulian, 2002a).

Chapter 6

Conclusions

We studied the origin of PeV electrons in the Crab Nebula based on the recent detection of 100 TeV gamma-ray emission from the Crab Nebula and observational studies with *Fermi*-LAT focusing on the day-scale and month-scale time variability. We summarized the results of this thesis as follows.

- We have obtained a constraint on the strength of the magnetic field nearby the acceleration site in a parameter-free way and put constraints on the MHD models for the Crab Nebula, in particular on the feasible magnetization and anisotropy of the pulsar wind. The obtained magnetic field is weak, 118 μG, to be consistent with observed fluxes measured in the MeV and > 100 TeV gamma-ray bands, which requires a small magnetization parameter $\sigma \simeq 0.01$ and a highly anisotropic pulsar wind. In addition, the gyro radius of PeV electrons in $B \sim 100$ μG is about 40% of the scale of the termination shock, which indicates that it is difficult to confine PeV electrons in a compact region nearby the termination shock. These implies the presence of the second component that is responsible for multi MeV gamma-ray synchrotron emission.
- We have discovered nine small-flux flares, "small flares" by analyzing 7.4 years gamma-ray data obtained with *Fermi*-LAT. The "small flares" and the flares which were reported in literature are characterized by "harder when brighter" feature. Observed energy fluxes and the photon indices during the flare state face difficulties by non-thermal electron distribution that is responsible for the broadband synchrotron emission. In addition, "small flares" show the day-scale time variability. The short time variabilities require the strong magnetic field of $B \sim 1$ mG which is larger than the typical strength of the magnetic field in the nebula. The presence of the "small flares" implies that the contribution of flaring components are not small for the 100 MeV gamma-ray emission.
- We have confirmed the month-scale time variability which was indicated by Abdo et al. (2011) and this variability is significant even if all flares are excluded. The observed energy fluxes and photon indices based on the 30-day binned analysis can not be explained by emission of electrons from the broad-band distribution which is responsible for the bulk of X-ray emission. This

implies that the month-scale variability requires another electron population, likely residing in a strong magnetic field of $B \sim 1$ mG. In addition, we found a possible correlation between the gamma-ray flux and the separation distance of the inner knot and the Crab pulsar. Further observations of the inner knot is required to verify the correlation.

Our observational and theoretical works suggest that "small flares" and the bulk of synchrotron gamma-ray emission originate from a region with a strong magnetic field $B \sim 1$ mG. This appears to be similar to the requirements for large-flux flares, which may imply that the origin of all multi MeV synchrotron emission is the same. As revealed with MHD simulations, regions with such a strong magnetic field should be located at the base of the jet. Our findings indicate that a second electron population is required to explain the gamma-ray synchrotron emission. Currently, there is no observational results that allow one to distinguish the day-scale variability and the month-scale variability, therefore it is possible that all synchrotron gamma-ray present a superposition of the short (∼day) and weak variable components, which can not be resolved by the current detectors. If the correlation between the gamma-ray and knot-pulsar separation is established, the origin of the month-scale or bulk gamma-ray emission is expected to be related with dynamics of the termination shock. If our scenario is correct, a new electron distribution, which is different from the electron distribution responsible for the bulk X-ray emission, is required. The presence of the second population can be tested by future MeV and TeV gamma-ray missions and detailed MHD simulations are also required to verify the feasibility of the production of synchrotron emission at the jet.

Appendix

A Probability density distributions of radiative model parameters

Figure A.1 show the probability density distributions of radiative model parameters fit to the *INTEGRAL*/SPI data points and the > 10 TeV gamma-ray data points.

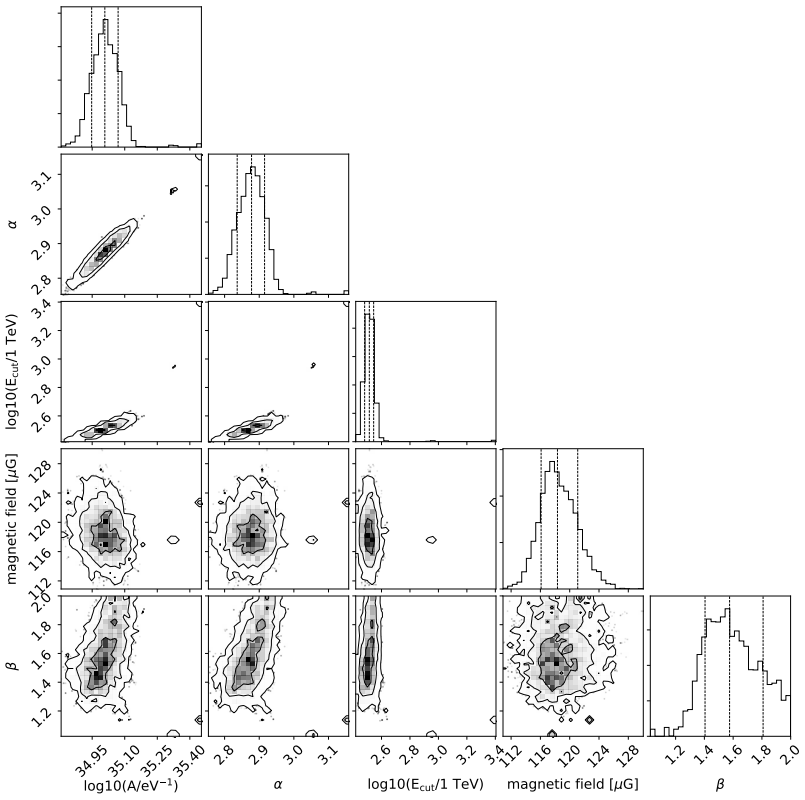

Figure A.1 One- and two-dimensional projections of the posterior probability density distributions of the parameters for the radiative model for the hard X-ray and gamma-ray (above 10 TeV) spectra of the Crab Nebula. The parameters of the electron spectrum are defined by Eq. 3.7. The lines overlaid to the one-dimensional projections are the 16th, 50th and 84th percentiles of the distributions. The contours overlaid to the two-dimensional projections correspond to 1σ, 1.5σ, and 2σ probability decrease with respect to the maximum.

Bibliography

[1] Abdo, A. A. et al. (2011) "Gamma-Ray Flares from the Crab Nebula," *Science*, Vol. 331, p. 739, DOI: 10.1126/science.1199705.

[2] Abdo, A. A. et al. (2010a) "Fermi Large Area Telescope Observations of the Crab Pulsar And Nebula," , Vol. 708, pp. 1254–1267, DOI: 10.1088/0004-637X/708/2/1254.

[3] Abdo, A. A. et al. (2010b) "Spectrum of the Isotropic Diffuse Gamma-Ray Emission Derived from First-Year Fermi Large Area Telescope Data," *Physical Review Letters*, Vol. 104, No. 10, p. 101101, DOI: 10.1103/PhysRevLett.104.101101.

[4] Abdo, A. A. et al. (2010c) "Observation of Supernova Remnant IC 443 with the Fermi Large Area Telescope," , Vol. 712, No. 1, pp. 459–468, DOI: 10.1088/0004-637X/712/1/459.

[5] Abeysekara, A. U. et al. (2019) "Measurement of the Crab Nebula Spectrum Past 100 TeV with HAWC," , Vol. 881, No. 2, p. 134, DOI: 10.3847/1538-4357/ab2f7d.

[6] Acero, F. et al. (2016) "Development of the Model of Galactic Interstellar Emission for Standard Point-source Analysis of Fermi Large Area Telescope Data," , Vol. 223, No. 2, p. 26, DOI: 10.3847/0067-0049/223/2/26.

[7] Ackermann, M. et al. (2012) "The Fermi Large Area Telescope on Orbit: Event Classification, Instrument Response Functions, and Calibration," , Vol. 203, No. 1, p. 4, DOI: 10.1088/0067-0049/203/1/4.

[8] Ackermann, M. et al. (2015) "The Spectrum of Isotropic Diffuse Gamma-Ray Emission between 100 MeV and 820 GeV," , Vol. 799, No. 1, p. 86, DOI: 10.1088/0004-637X/799/1/86.

[9] Aharonian, F. A. and A. M. Atoyan (1981) "Compton scattering of relativistic electrons in compact X-ray sources," , Vol. 79, pp. 321–336, DOI: 10.1007/BF00649428.

[10] Aharonian, F. A. and A. M. Atoyan (1998) "Nonthermal Radiation of the Crab Nebula," in Shibazaki, N. ed. *Neutron Stars and Pulsars: Thirty Years after the Discovery*, p. 439.

[11] Aharonian, F. A. et al. (2002) "Constraints on the extremely high-energy cosmic ray accelerators from classical electrodynamics," , Vol. 66, No. 2, p. 023005, DOI: 10.1103/PhysRevD.66.023005.

[12] Aharonian, F. A., S. R. Kelner, and A. Y. Prosekin (2010) "Angular, spectral, and time distributions of highest energy protons and associated secondary gamma rays and neutrinos propa-

gating through extragalactic magnetic and radiation fields," , Vol. 82, No. 4, p. 043002, DOI: 10.1103/PhysRevD.82.043002.

[13] Aharonian, F. et al. (2004) "The Crab Nebula and Pulsar between 500 GeV and 80 TeV: Observations with the HEGRA Stereoscopic Air Cerenkov Telescopes," , Vol. 614, No. 2, pp. 897–913, DOI: 10.1086/423931.

[14] Aharonian, F. et al. (2006) "Observations of the Crab nebula with HESS," , Vol. 457, No. 3, pp. 899–915, DOI: 10.1051/0004-6361:20065351.

[15] Albert, J. et al. (2008) "VHE γ-Ray Observation of the Crab Nebula and its Pulsar with the MAGIC Telescope," , Vol. 674, No. 2, pp. 1037–1055, DOI: 10.1086/525270.

[16] Aleksić, J. et al. (2011) "Observations of the Crab Pulsar between 25 and 100 GeV with the MAGIC I Telescope," , Vol. 742, p. 43, DOI: 10.1088/0004-637X/742/1/43.

[17] Aleksić, J. et al. (2015) "Measurement of the Crab Nebula spectrum over three decades in energy with the MAGIC telescopes," *Journal of High Energy Astrophysics*, Vol. 5, pp. 30–38, DOI: 10.1016/j.jheap.2015.01.002.

[18] Aliu, E. et al. (2014) "A Search for Enhanced Very High Energy Gamma-Ray Emission from the 2013 March Crab Nebula Flare," , Vol. 781, p. L11, DOI: 10.1088/2041-8205/781/1/L11.

[19] Amenomori, M. et al. (2019) "First Detection of Photons with Energy beyond 100 TeV from an Astrophysical Source," , Vol. 123, No. 5, p. 051101, DOI: 10.1103/PhysRevLett.123.051101.

[20] Aramaki, Tsuguo et al. (2020) "Dual MeV gamma-ray and dark matter observatory - GRAMS Project," *Astroparticle Physics*, Vol. 114, pp. 107–114, DOI: 10.1016/j.astropartphys.2019.07.002.

[21] Arons, J. (2012) "Pulsar Wind Nebulae as Cosmic Pevatrons: A Current Sheet's Tale," , Vol. 173, pp. 341–367, DOI: 10.1007/s11214-012-9885-1.

[22] Atoyan, A. M. and F. A. Aharonian (1996) "On the mechanisms of gamma radiation in the Crab Nebula," , Vol. 278, pp. 525–541, DOI: 10.1093/mnras/278.2.525.

[23] Atwood, W. et al. (2013) "Pass 8: Toward the Full Realization of the Fermi-LAT Scientific Potential," *arXiv e-prints*, p. arXiv:1303.3514.

[24] Atwood, W. B. et al. (2009) "The Large Area Telescope on the Fermi Gamma-Ray Space Telescope Mission," , Vol. 697, No. 2, pp. 1071–1102, DOI: 10.1088/0004-637X/697/2/1071.

[25] Bai, X. et al. (2019) "The Large High Altitude Air Shower Observatory (LHAASO) Science White Paper," *arXiv e-prints*, p. arXiv:1905.02773.

[26] Barkov, Maxim V., Maxim Lyutikov, and Dmitry Khangulyan (2019) "3D dynamics and morphology of bow-shock pulsar wind nebulae," , Vol. 484, No. 4, pp. 4760–4784, DOI: 10.1093/mnras/stz213.

[27] Blumenthal, George R. and Robert J. Gould (1970) "Bremsstrahlung, Synchrotron Radiation, and Compton Scattering of High-Energy Electrons Traversing Dilute Gases," *Reviews of Modern Physics*, Vol. 42, No. 2, pp. 237–271, DOI: 10.1103/RevModPhys.42.237.

[28] Bogovalov, S. V. et al. (2005) "Interaction of pulsar winds with interstellar medium: numerical simulation," , Vol. 358, No. 3, pp. 705–715, DOI: 10.1111/j.1365-2966.2004.08592.x.

[29] Bogovalov, S. V. and D. V. Khangoulian (2002a) "On the origin of the torus and jet-like structures in the centre of the Crab Nebula," , Vol. 336, No. 3, pp. L53–L55, DOI: 10.1046/j.1365-8711.2002.06027.x.

[30] Bogovalov, S. V. and D. V. Khangoulian (2002b) "On the origin of the torus and jet-like structures in the centre of the Crab Nebula," , Vol. 336, No. 3, pp. L53–L55, DOI: 10.1046/j.1365-8711.2002.06027.x.

[31] Bogovalov, S. V. and D. V. Khangoulyan (2002) "The Crab Nebula: interpretation of Chandra observations.," *Astronomy Letters*, Vol. 28, pp. 373–385, DOI: 10.1134/1.1484137.

[32] Bucciantini, N. (2014) "Review of the theory of pulsar-wind nebulae," *Astronomische Nachrichten*, Vol. 335, No. 3, pp. 234–239, DOI: 10.1002/asna.201312024.

[33] Buehler, R. et al. (2012) "Gamma-Ray Activity in the Crab Nebula: The Exceptional Flare of 2011 April," *The Astrophysical Journal*, Vol. 749, No. 1, p. 26.

[34] Bühler, R. and R. Blandford (2014) "The surprising Crab pulsar and its nebula: a review," *Reports on Progress in Physics*, Vol. 77, No. 6, p. 066901, DOI: 10.1088/0034-4885/77/6/066901.

[35] Bykov, A. M. et al. (2012) "Twinkling pulsar wind nebulae in the synchrotron cut-off regime and the γ-ray flares in the Crab Nebula," , Vol. 421, No. 1, pp. L67–L71, DOI: 10.1111/j.1745-3933.2011.01208.x.

[36] Camus, N. F. et al. (2009) "Observations of 'wisps' in magnetohydrodynamic simulations of the Crab Nebula," *Monthly Notices of the Royal Astronomical Society*, Vol. 400, No. 3, pp. 1241–1246, DOI: 10.1111/j.1365-2966.2009.15550.x.

[37] Cerutti, B. et al. (2012) "Beaming and Rapid Variability of High-energy Radiation from Relativistic Pair Plasma Reconnection," , Vol. 754, No. 2, p. L33, DOI: 10.1088/2041-8205/754/2/L33.

[38] Cerutti, B. et al. (2013) "Simulations of Particle Acceleration beyond the Classical Synchrotron Burnoff Limit in Magnetic Reconnection: An Explanation of the Crab Flares," , Vol. 770, No. 2, p. 147, DOI: 10.1088/0004-637X/770/2/147.

[39] Clemens, D. P. (1985) "Massachusetts-Stony Brook Galactic plane CO survey: the galactic disk rotation curve.," *The Astrophysical Journal*, Vol. 295, pp. 422–436, DOI: 10.1086/163386.

[40] de Angelis, A. et al. (2018) "Science with e-ASTROGAM. A space mission for MeV-GeV gamma-ray astrophysics," *Journal of High Energy Astrophysics*, Vol. 19, pp. 1–106, DOI: 10.1016/j.jheap.2018.07.001.

[41] Del Zanna, Luca and Barbara Olmi (2017) "Multidimensional Relativistic MHD Simulations of Pulsar Wind Nebulae: Dynamics and Emission," in Torres, Diego F. ed. *Modelling Pulsar Wind Nebulae*, Vol. 446 of Astrophysics and Space Science Library, p. 215, Jan, DOI: 10.1007/978-3-319-63031-1$_1$0.

[42] Derishev, E. V., F. A. Aharonian, and Vl. V. Kocharovsky (2007) "Off-Axis Emission from Relativistic Plasma Flows," , Vol. 655, No. 2, pp. 980–988, DOI: 10.1086/509818.

[43] Derishev, Evgeny and Felix Aharonian (2019) "Exact analytical expression for the synchrotron radiation spectrum in the Gaussian turbulent magnetic field," *arXiv e-prints*, p. arXiv:1907.11663.

[44] Edelson, R. A. and J. H. Krolik (1988) "The Discrete Correlation Function: A New Method for Analyzing Unevenly Sampled Variability Data," , Vol. 333, p. 646, DOI: 10.1086/166773.

[45] Foreman-Mackey, D. et al. (2013) "emcee: The MCMC Hammer," , Vol. 125, p. 306, DOI: 10.1086/670067.

[46] Gasparrini, D. and R. Buehler (2014) "Fermi LAT detection of enhanced gamma-ray emission from the Crab Nebula region," *The Astronomer's Telegram*, Vol. 5971.

[47] H. E. S. S. Collaboration et al. (2018) "The H.E.S.S. Galactic plane survey," , Vol. 612, p. A1, DOI: 10.1051/0004-6361/201732098.

[48] H. E. S. S. Collaboration et al. (2019a) "Resolving the Crab pulsar wind nebula at teraelectronvolt energies," *arXiv e-prints*, p. arXiv:1909.09494.

[49] H. E. S. S. Collaboration et al. (2019b) "H.E.S.S. and Suzaku observations of the Vela X pulsar wind nebula," , Vol. 627, p. A100, DOI: 10.1051/0004-6361/201935458.

[50] H. E. S. S. Collaboration et al. (2014) "H.E.S.S. observations of the Crab during its March 2013 GeV gamma-ray flare," , Vol. 562, p. L4, DOI: 10.1051/0004-6361/201323013.

[51] Hayashida, M. et al. (2015) "Rapid Variability of Blazar 3C 279 during Flaring States in 2013-2014 with Joint Fermi-LAT, NuSTAR, Swift, and Ground-Based Multiwavelength Observations," , Vol. 807, p. 79, DOI: 10.1088/0004-637X/807/1/79.

[52] He, H. (2019) "Status and First Results of the LHAASO Experiment," in *36th International Cosmic Ray Conference (ICRC2019)*, Vol. 36 of International Cosmic Ray Conference, p. 693, Jul.

[53] Hester, J. J. (2008) "The Crab Nebula: An Astrophysical Chimera," , Vol. 46, pp. 127–155, DOI: 10.1146/annurev.astro.45.051806.110608.

[54] Hester, J. J. et al. (1995) "WFPC2 Studies of the Crab Nebula. I. HST and ROSAT Imaging of the Synchrotron Nebula," , Vol. 448, p. 240, DOI: 10.1086/175956.

[55] Hobbs, G. B., R. T. Edwards, and R. N. Manchester (2006) "TEMPO2, a new pulsar-timing package - I. An overview," , Vol. 369, pp. 655–672, DOI: 10.1111/j.1365-2966.2006.10302.x.

[56] Jourdain, E. and J. P. Roques (2009) "The High-Energy Emission of the Crab Nebula from 20 keV TO 6 MeV with Integral SPI," , Vol. 704, No. 1, pp. 17–24, DOI: 10.1088/0004-637X/704/1/17.

[57] Kelner, S. R., F. A. Aharonian, and D. Khangulyan (2013) "On the Jitter Radiation," , Vol. 774, No. 1, p. 61, DOI: 10.1088/0004-637X/774/1/61.

[58] Kennel, C. F. and F. V. Coroniti (1984a) "Magnetohydrodynamic model of Crab nebula radia-

tion.," , Vol. 283, pp. 710–730, DOI: 10.1086/162357.

[59] Kennel, C. F. and F. V. Coroniti (1984b) "Confinement of the Crab pulsar's wind by its supernova remnant," , Vol. 283, pp. 694–709, DOI: 10.1086/162356.

[60] Kerr, M. et al. (2015) "Timing Gamma-ray Pulsars with the Fermi Large Area Telescope: Timing Noise and Astrometry," , Vol. 814, No. 2, p. 128, DOI: 10.1088/0004-637X/814/2/128.

[61] Khangulyan, D., F. A. Aharonian, and S. R. Kelner (2014) "Simple Analytical Approximations for Treatment of Inverse Compton Scattering of Relativistic Electrons in the Blackbody Radiation Field," , Vol. 783, p. 100, DOI: 10.1088/0004-637X/783/2/100.

[62] Khangulyan, Dmitry, Masanori Arakawa, and Felix Aharonian (2020) "Detection of ultra-high-energy gamma rays from the Crab Nebula: physical implications," , Vol. 491, No. 3, pp. 3217–3224, DOI: 10.1093/mnras/stz3261.

[63] Kirsch, M. G. et al. (2005) "Crab: the standard x-ray candle with all (modern) x-ray satellites," in Siegmund, Oswald H. W. ed. , Vol. 5898 of Society of Photo-Optical Instrumentation Engineers (SPIE) Conference Series, pp. 22–33, Aug, DOI: 10.1117/12.616893.

[64] Komissarov, S. S. and Y. E. Lyubarsky (2004) "Synchrotron nebulae created by anisotropic magnetized pulsar winds," , Vol. 349, No. 3, pp. 779–792, DOI: 10.1111/j.1365-2966.2004.07597.x.

[65] Komissarov, S. S. and M. Lyutikov (2011) "On the origin of variable gamma-ray emission from the Crab nebula," , Vol. 414, No. 3, pp. 2017–2028, DOI: 10.1111/j.1365-2966.2011.18516.x.

[66] Komissarov, Serguei S. (2013) "Magnetic dissipation in the Crab nebula," , Vol. 428, No. 3, pp. 2459–2466, DOI: 10.1093/mnras/sts214.

[67] Kouzu, Tomomi et al. (2013) "Spectral Variation of Hard X-Ray Emission from the Crab Nebula with the Suzaku Hard X-Ray Detector," , Vol. 65, p. 74, DOI: 10.1093/pasj/65.4.74.

[68] Kuiper, L. et al. (2001) "The Crab pulsar in the 0.75-30 MeV range as seen by CGRO COMPTEL. A coherent high-energy picture from soft X-rays up to high-energy gamma-rays," , Vol. 378, pp. 918–935, DOI: 10.1051/0004-6361:20011256.

[69] Lyubarsky, Y. E. (2002a) "On the structure of the inner Crab Nebula," , Vol. 329, No. 2, pp. L34–L36, DOI: 10.1046/j.1365-8711.2002.05151.x.

[70] Lyubarsky, Y. E. (2002b) "On the structure of the inner Crab Nebula," , Vol. 329, No. 2, pp. L34–L36, DOI: 10.1046/j.1365-8711.2002.05151.x.

[71] Lyubarsky, Y. E. (2003) "The termination shock in a striped pulsar wind," , Vol. 345, No. 1, pp. 153–160, DOI: 10.1046/j.1365-8711.2003.06927.x.

[72] Lyubarsky, Y. E. (2005) "On the relativistic magnetic reconnection," , Vol. 358, No. 1, pp. 113–119, DOI: 10.1111/j.1365-2966.2005.08767.x.

[73] Lyubarsky, Y. E. (2012) "Highly magnetized region in pulsar wind nebulae and origin of the Crab gamma-ray flares," , Vol. 427, No. 2, pp. 1497–1502, DOI: 10.1111/j.1365-2966.2012.22097.x.

[74] Lyutikov, M., S. S. Komissarov, and O. Porth (2016) "The inner knot of the Crab nebula," , Vol.

456, pp. 286–299, DOI: 10.1093/mnras/stv2570.

[75] Lyutikov, M. et al. (2018b) "Interpreting Crab Nebula synchrotron spectrum: two acceleration mechanisms," *arXiv e-prints*.

[76] Lyutikov, Maxim et al. (2018a) "Particle acceleration in explosive relativistic reconnection events and Crab Nebula gamma-ray flares," *Journal of Plasma Physics*, Vol. 84, No. 2, p. 635840201, DOI: 10.1017/S0022377818000168.

[77] Madsen, Kristin K. et al. (2015) "Broadband X-ray Imaging and Spectroscopy of the Crab Nebula and Pulsar with NuSTAR," , Vol. 801, No. 1, p. 66, DOI: 10.1088/0004-637X/801/1/66.

[78] Mattox, J. R. et al. (1996) "The Likelihood Analysis of EGRET Data," , Vol. 461, p. 396, DOI: 10.1086/177068.

[79] Mayer, M. et al. (2013) "Rapid Gamma-Ray Flux Variability during the 2013 March Crab Nebula Flare," , Vol. 775, p. L37, DOI: 10.1088/2041-8205/775/2/L37.

[80] Mayer, Michael (2015) *Pulsar wind nebulae at high energies* doctoralthesis, Universität Potsdam.

[81] Meyer, M., D. Horns, and H.-S. Zechlin (2010) "The Crab Nebula as a standard candle in very high-energy astrophysics," , Vol. 523, p. A2, DOI: 10.1051/0004-6361/201014108.

[82] Nolan, P. L. et al. (2012) "VizieR Online Data Catalog: Fermi LAT second source catalog (2FGL) (Nolan+, 2012)," *VizieR Online Data Catalog*, p. J/ApJS/199/31.

[83] Olmi, B. et al. (2014) "On the magnetohydrodynamic modelling of the Crab nebula radio emission," , Vol. 438, No. 2, pp. 1518–1525, DOI: 10.1093/mnras/stt2308.

[84] Olmi, B. et al. (2015) "Constraints on particle acceleration sites in the Crab nebula from relativistic magnetohydrodynamic simulations," , Vol. 449, No. 3, pp. 3149–3159, DOI: 10.1093/mnras/stv498.

[85] Olmi, B. et al. (2016) "Multi-D magnetohydrodynamic modelling of pulsar wind nebulae: recent progress and open questions," *Journal of Plasma Physics*, Vol. 82, No. 6, p. 635820601, DOI: 10.1017/S0022377816000957.

[86] Porth, Oliver et al. (2017) "Modelling Jets, Tori and Flares in Pulsar Wind Nebulae," , Vol. 207, No. 1-4, pp. 137–174, DOI: 10.1007/s11214-017-0344-x.

[87] Porth, Oliver, Serguei S. Komissarov, and Rony Keppens (2014) "Three-dimensional magnetohydrodynamic simulations of the Crab nebula," , Vol. 438, No. 1, pp. 278–306, DOI: 10.1093/mnras/stt2176.

[88] Rees, M. J. and J. E. Gunn (1974) "The origin of the magnetic field and relativistic particles in the Crab Nebula," , Vol. 167, pp. 1–12, DOI: 10.1093/mnras/167.1.1.

[89] Robertson, D. R. S. et al. (2015) "Searching for correlations in simultaneous X-ray and UV emission in the narrow-line Seyfert 1 galaxy 1H 0707-495," , Vol. 453, No. 4, pp. 3455–3460, DOI: 10.1093/mnras/stv1575.

[90] Rudy, A. et al. (2015) "Characterization of the Inner Knot of the Crab: The Site of the Gamma-

Ray Flares?," , Vol. 811, p. 24, DOI: 10.1088/0004-637X/811/1/24.

[91] Rybicki, George B. and Alan P. Lightman (1979) *Radiative processes in astrophysics*.

[92] Sironi, Lorenzo and Anatoly Spitkovsky (2011) "Acceleration of Particles at the Termination Shock of a Relativistic Striped Wind," , Vol. 741, No. 1, p. 39, DOI: 10.1088/0004-637X/741/1/39.

[93] Sironi, Lorenzo and Anatoly Spitkovsky (2014) "Relativistic Reconnection: An Efficient Source of Non-thermal Particles," , Vol. 783, No. 1, p. L21, DOI: 10.1088/2041-8205/783/1/L21.

[94] Striani, E. et al. (2011) "The Crab Nebula Super-flare in 2011 April: Extremely Fast Particle Acceleration and Gamma-Ray Emission," , Vol. 741, No. 1, p. L5, DOI: 10.1088/2041-8205/741/1/L5.

[95] Striani, E. et al. (2013) "Variable Gamma-Ray Emission from the Crab Nebula: Short Flares and Long "Waves"," *The Astrophysical Journal*, Vol. 765, No. 1, p. 52.

[96] Strong, Andrew W., Igor V. Moskalenko, and Vladimir S. Ptuskin (2007) "Cosmic-Ray Propagation and Interactions in the Galaxy," *Annual Review of Nuclear and Particle Science*, Vol. 57, No. 1, pp. 285–327, DOI: 10.1146/annurev.nucl.57.090506.123011.

[97] Tavani, M. et al. (2011) "Discovery of Powerful Gamma-Ray Flares from the Crab Nebula," *Science*, Vol. 331, No. 6018, p. 736, DOI: 10.1126/science.1200083.

[98] The Fermi-LAT collaboration (2019) "Fermi Large Area Telescope Fourth Source Catalog," *arXiv e-prints*.

[99] Uzdensky, Dmitri A., Benoît Cerutti, and Mitchell C. Begelman (2011) "Reconnection-powered Linear Accelerator and Gamma-Ray Flares in the Crab Nebula," , Vol. 737, No. 2, p. L40, DOI: 10.1088/2041-8205/737/2/L40.

[100] VERITAS Collaboration et al. (2011) "Detection of Pulsed Gamma Rays Above 100 GeV from the Crab Pulsar," *Science*, Vol. 334, p. 69, DOI: 10.1126/science.1208192.

[101] Vernetto, Silvia and Paolo Lipari (2016) "Absorption of very high energy gamma rays in the Milky Way," , Vol. 94, No. 6, p. 063009, DOI: 10.1103/PhysRevD.94.063009.

[102] Volpi, D. et al. (2008) "Non-thermal emission from relativistic MHD simulations of pulsar wind nebulae: from synchrotron to inverse Compton," , Vol. 485, No. 2, pp. 337–349, DOI: 10.1051/0004-6361:200809424.

[103] Weekes, T. C. et al. (1989) "Observation of TeV Gamma Rays from the Crab Nebula Using the Atmospheric Cerenkov Imaging Technique," , Vol. 342, p. 379, DOI: 10.1086/167599.

[104] Weisskopf, M. C. et al. (2000) "Discovery of Spatial and Spectral Structure in the X-Ray Emission from the Crab Nebula," , Vol. 536, pp. L81–L84, DOI: 10.1086/312733.

[105] Weisskopf, Martin C. et al. (2013) "Chandra, Keck, and VLA Observations of the Crab Nebula during the 2011-April Gamma-Ray Flare," , Vol. 765, No. 1, p. 56, DOI: 10.1088/0004-637X/765/1/56.

[106] Wilson-Hodge, Colleen A. et al. (2011) "When a Standard Candle Flickers," , Vol. 727, No. 2,

p. L40, DOI: 10.1088/2041-8205/727/2/L40.

[107] Yeung, Paul K. H. and Dieter Horns (2019) "The Energy-dependent γ-Ray Morphology of the Crab Nebula Observed with the Fermi Large Area Telescope," , Vol. 875, No. 2, p. 123, DOI: 10.3847/1538-4357/ab107a.

[108] Yuan, Y. and R. D. Blandford (2015) "On the implications of recent observations of the inner knot in the Crab nebula," , Vol. 454, pp. 2754–2769, DOI: 10.1093/mnras/stv2093.

[109] Zabalza, V. (2015) "naima: a Python package for inference of relativistic particle energy distributions from observed nonthermal spectra," *Proc. of International Cosmic Ray Conference 2015*, p. 922.

[110] Zirakashvili, V. N. and F. Aharonian (2007) "Analytical solutions for energy spectra of electrons accelerated by nonrelativistic shock-waves in shell type supernova remnants," , Vol. 465, No. 3, pp. 695–702, DOI: 10.1051/0004-6361:20066494.

[111] Zirakashvili, V. N. and F. A. Aharonian (2010) "Nonthermal Radiation of Young Supernova Remnants: The Case of RX J1713.7-3946," , Vol. 708, No. 2, pp. 965–980, DOI: 10.1088/0004-637X/708/2/965.

[112] Zirakashvili, V. N. and V. S. Ptuskin (2008) "Diffusive Shock Acceleration with Magnetic Amplification by Nonresonant Streaming Instability in Supernova Remnants," , Vol. 678, No. 2, pp. 939–949, DOI: 10.1086/529580.

Acknowledgements

First of all, I am deeply grateful to my supervisor Prof. Yasunobu Uchiyama for guiding and encouraging me throughout seven years at Rikkyo University. I learned a lot of things from his deep insights into physics. I am really proud of having been a member of his group. I thank Dr. Masaaki Hayashida for his comments on data analysis, the draft, and the presentations. Without his advice, I would not reach this stage. I also thank Dr. Dmitry Khangulyan for the discussions about the interpretations of data analysis results. His meaningful comments and ideas enriched this thesis. I am grateful to Dr. Yuto Ichinohe for encouraging me and giving advice for the data analysis. I would like to thank Prof. Kitamoto and Prof. Kurita for useful suggestions and comments.

I really appreciate Dr. Shigehiro Nagataki for giving me the opportunity to study at RIKEN. I also thank the members of Astrophysical Big Bang Laboratory. I learned the attitude as a researcher and enjoyed the discussions and events in his group.

I would like to thank all the colleagues in Department of Physics in Rikkyo University, especially the members of Uchiyama group. Finally, I really thank my family for their support and encouragement.